UNIVERSITY OF CALIFORNIA

Santa Barbara

Optically Pumped Ultra-Low Loss Waveguide Lasers and Amplifiers

A dissertation submitted in partial satisfaction of the

requirements for the degree

Doctor of Philosophy

In

Electrical and Computer Engineering

by

Michael Belt

Committee in charge:

Professor Daniel J. Blumenthal, Chair

Professor John E. Bowers

Professor Larry A. Coldren

Professor Rod C. Alferness

June 2017

The dissertation of Michael Belt is approved:

Professor John E. Bowers

Professor Larry A. Coldren

Professor Rod C. Alferness

Professor Daniel J. Blumenthal, Committee Chair

June 2017

Optically Pumped Ultra-Low Loss Waveguide Lasers and Amplifiers

Acknowledgements

Throughout my rollercoaster of a time here at UCSB, one concept has remained steadily constant: you win with people. To all the professors, staff, colleagues, friends, and haters I’ve met during my stay in Santa Barbara, thank you.

Curriculum Vitae for Michael Belt

June 2017

PERSONAL

Full Name: Michael Lawrence Belt
Place of Birth: Peoria, Illinois, U.S.A.

EDUCATION

Doctor of Philosophy in Electrical and Computer Engineering, Electrical and Computer Engineering Department, University of California Santa Barbara, Santa Barbara, California, U.S.A., June 2017

Master of Science in Electrical and Computer Engineering, Electrical and Computer Engineering Department, University of California Santa Barbara, Santa Barbara, California, U.S.A., March 2012

Bachelor of Science in Electrical and Computer Engineering (Cum Laude), Department of Electrical and Computer Engineering, The Ohio State University, Columbus, Ohios, U.S.A., June 2010

EXPERIENCE

2010-2017: Graduate Student Researcher, University of California, Santa Barbara, California, U.S.A.

2009: Undergraduate Researcher, The ElectroScience Laboratory, The Ohio State University, Columbus, Ohio, U.S.A.

2008: Aluminum Machining Intern, Honda of America Manufacturing, Marysville, Ohio, U.S.A.

PUBLICATIONS

Portions of this thesis have been drawn from the following publications:

PRIMARY AUTHOR

M. Belt, M. Davenport, J. E. Bowers, and D. J. Blumenthal, "Ultra-Low-Loss Ta_2O_5-Core/SiO_2-Clad Planar Waveguides on Si Substrates," Optica 4, 532-536 (2017).

M. Belt and D. J. Blumenthal, "High Temperature Operation of an Integrated Erbium-Doped DBR Laser on an Ultra-Low-Loss Si_3N_4 Platform," in Optical Fiber Communication Conference/National Fiber Optic Engineers Conference 2015, OSA Technical Digest (online) (Optical Society of America, 2015), paper Tu2C.7.

M. Belt and D. J. Blumenthal, “Erbium-doped waveguide DBR and DFB laser arrays integrated within an ultra-low-loss S3N4 platform,” Opt. Express 22 (9), 10655-10660 (2014).

M. Belt, M. Heck, J. Barton, J. Bauters, J. Bowers, and D. Blumenthal, “Apodized and Un-Apodized Sidewall Grating Filters with Low Coupling Constants in Ultra-Low-Loss Si3N4 Planar Waveguides,” in Optical Fiber Communication Conference/National Fiber Optic Engineers Conference 2013, OSA Technical Digest (online) (Optical Society of America, 2013), paper OTu3C.3.

M. Belt, T. Huffman, M. L. Davenport, W. Li, J. S. Barton, and D. J. Blumenthal, “Arrayed narrow linewidth erbium-doped waveguide-distributed feedback lasers on an ultra-low-loss silicon-nitride platform,” Opt. Letters 38 (22), 4825-4828 (2013).

M. Belt, J. Bovington, R. Moreira, J. Bauters, M. Heck, J. Barton, J. Bowers, and D. J. Blumenthal, “Sidewall gratings in ultra-low-loss Si3N4 planar waveguides,” Opt. Express 21, 1181-1188 (2013).

SUPPORTING AUTHOR

S. Gundavarapu, **M. Belt**, T. Huffman, M. A. Tran, T. Komljenovic, J. E. Bowers and D. J. Blumenthal, “Integrated Sagnac optical gyroscope sensor using ultra-low loss high aspect ratio silicon nitride waveguide coil,” Proc. SPIE 10323, 25th International Conference on Optical Fiber Sensors, 103231A (2017).

T. Huffman, M. Davenport, **M. Belt**, J. Bowers, and D. J. Blumenthal, “Ultra-low loss large area waveguide coils for integrated optical gyroscopes,” Photonics Technology Letters, IEEE, vol. 29, no. 2, January 15, 2017.

T. Huffman, M. Davenport, **M. Belt**, J. E. Bowers, and D. J. Blumenthal, "Ultra-low loss stitching for large-area waveguide based delay-line gyroscopes," 2016 IEEE Photonics Conference (IPC), Waikoloa, HI, USA, 2016, pp. 478-479.

T. Komljenovic, M. A. Tran, **M. Belt**, S. Gundavarapu, D. J. Blumenthal, and J. E. Bowers, “Frequency modulated lasers for interferometric optical gyroscopes,” Opt. Lett. 41, 1773-1776 (2016).

M. Tran, S. Gundaravapu, **M. Belt**, T. Komljenovic, D. J. Blumenthal, and J. E. Bowers, “Frequency Modulated Laser Based Interferometric Optical Gyroscope,” in CLEO: 2016, OSA Technical Digest (online) (Optical Society of America, 2016), poster JTu5A.140.

S. Gundavarapu, T. Huffman, **M. Belt**, R. Moreira, J. Bowers, and D. Blumenthal, “Integrated Ultra-Low-Loss Silicon Nitride Waveguide Coil for Optical Gyroscopes,” in Optical Fiber Communication Conference, OSA Technical Digest (online) (Optical Society of America, 2016), paper W4E.5.

Y. Shen, M. Tran, S. Srinivasan, J. Hulme, J. Peters, **M. Belt**, S. Gundavarapu, Y. Li, D. J.

Blumenthal and J. E. Bowers, “Frequency Modulated Laser Optical Gyroscope,” IPC 2015.

J. Garcia, K. Nguyen, **M. Belt**, H. Poulsen, and D. Blumenthal, “Demonstration of Edge Interoperability, Re-Shaping and Re-Timing using Hybrid Mode-Locking within a 40Gb/s Optical Packet Router,” in Optical Fiber Communication Conference/National Fiber Optic Engineers Conference 2013, OSA Technical Digest (online) (Optical Society of America, 2013), paper OTh4D.7.

Abstract

Optically Pumped Ultra-Low Loss Waveguide Lasers and Amplifiers

by

Michael Belt

An increasing number of systems and applications depend on photonics for transmission and signal processing. This includes data centers, communications systems, environmental sensing, radar, lidar, and microwave signal generation. Moving forward, monolithic integration of traditionally bulk optical components onto the chip scale will be necessary to significantly reduce power and cost while simultaneously maintaining the requisite performance specifications at high production volumes. A critical aspect is the loss of the integrated waveguide, along with the capability to design a wide range of passive and active optical elements using a low cost, highly manufacturable wafer-scale integration process such as that found in the electronics industry (CMOS). There has been a strong body of work to date on the reduction of waveguide loss and implementation of devices based on passive waveguides. This dissertation advances the state of the art in ultra-low loss waveguide integration by developing and realizing on-chip optical gain elements, and ultimately lasers, based on rare-earth-ion dopants. The analysis, design, fabrication procedure, and resulting experimental demonstration of a series of rare-earth-ion-doped optically pumped lasers that leverage the unique properties of a Si_3N_4-core/SiO_2-clad ultra-low loss waveguide platform is detailed. The low passive loss and highly temperature stable optical gain properties of this platform enable integration of a wide variety of linear and nonlinear optical components on-chip. This opens new integration possibilities within the data communications, microwave

photonics, high bandwidth electrical RF systems, sensing, and optical signal processing applications and research communities.

Table of Contents

Chapter 1

Introduction

Despite the tremendous advances in the information carrying capacity of lightwave communication systems over the past thirty years, the unabated growth in demand driven by multinational corporations, governments, institutions, and consumers continues to propel technological innovation. Global IP traffic is projected to increase nearly threefold over the next five years and will have increased nearly a hundredfold from 2005 to 2020. Recent developments in wireless and mobile devices have driven additional explosive demand over the past five years, with smartphone IP traffic projected to exceed PC traffic by 2020 [1]. Beyond data communications, server manufacturers have begun to investigate optical systems for on-board communications in parallel computing applications where transmission capacity and power dissipation exceed the limits of electrical wiring. While first generation optical systems relied solely on optical fibers to transmit and carry information, emerging systems such as those found in datacenters have begun to leverage optical waveguides in place of traditional electrical interconnects due to the low cost of communicating at ever increasing bandwidths [2][3]. Even fields classically unrelated to optics, such as gyroscopic and biological sensing, have begun harnessing waveguide technologies [4][5]. By leveraging modern high volume wafer-scale semiconductor manufacturing techniques and throughputs technologies that incorporate chip-scale photonic integrated circuits (PICs) are uniquely positioned to continue meeting demand within this broadening application space.

1.1 Integrated Optics

The benefits of using an integrated waveguide platform over a coil of optical fiber are similar to the use of electrical microchips over wire connectors and discrete components; that is a reduction package size, an improved environmental and mechanical robustness, and fine degree of control over device dimensions. It is important to note that optical waveguide propagation loss is of critical importance. Over nearly the past decade, research and development efforts carried out here at UCSB and our partner foundries have focused on implementing and refining record low loss stoichiometric Si_3N_4-core/SiO_2-clad ultra-low loss waveguides (ULLWs) [6][7].

1.2 Motivation

Thus far, research and development results on the ULLW platform have been limited to devices and components of strictly a passive nature (no generation or amplification of photons). From a system design standpoint, a complete integrated optical platform should also include active functionality for on-chip generation and amplification of light. Furthermore, due to the extremely low loss nature of the waveguide platform on-chip applications which demand low phase noise, such as microwave signal generation, heavily benefit from such an approach. Moreover, due to the nature of a rare-earth-ion doped gain material compared to a semiconductor alternative significant potential exists for optical linewidth narrowing, which in turn serves additional applications such as Brillouin signal generation. Finally, a small form factor design is essential, as compact waveguide amplifiers are necessary to serve alongside two photon absorption limited silicon photonics solutions.

1.3 This Dissertation: Scope and Objectives

The objective of this thesis is to develop a new class of optically pumped rare-earth-ion-doped dielectric waveguide lasers and amplifiers on an ultra-low loss Si_3N_4-core/SiO_2-clad platform, along with advancement of the passive waveguiding structure of the platform to include a CMOS compatible Ta_2O_5 core material. Each of the constituent parts that make up such devices, from optically pumped waveguide amplifier sections to waveguide sidewall Bragg grating mirror reflectors, are covered. The specification, analysis and design, fabrication procedure and process flow, and characterization protocols of each component is detailed. While the work on active rare-earth-ion-doped lasers and amplifiers has advanced the state of the art in integration by leveraging the low loss passive functionalities afforded by the Si_3N_4-core waveguide structure, the development of record low loss Ta_2O_5-core waveguides, which provide lower propagation loss when compared to Si_3N_4-core waveguides with equivalent geometry, introduces new avenues for device and component research. Finally, an extremely high quality deep SiO_2 etching protocol for high optical confinement waveguides (and thus reduction in device footprint), as well as transition regions between these strongly guiding waveguides and the previously demonstrated weakly guiding waveguides, is demonstrated. This newly developed waveguide design and fabrication procedure extends the minimum bend radius of the ULLW platform to below 65 μm.

1.4 Results Highlight

While this thesis examines a wide array of design, fabrication, and characterization processes and results on components and devices on an ultra-low loss waveguide platform, there are several technology demonstrations that serve as key elements for the basis of work that follows.

1.4.1 Ultra-Low Loss Ta_2O_5 Waveguides

Chapter 4 reports the demonstration of a record low propagation loss of 3±1 dB/m across the entire telecommunications C-band for a CMOS compatible Ta_2O_5-core/SiO_2-clad planar waveguide. The waveguide design, fabrication process, and optical frequency domain reflectometry characterization of the waveguide propagation loss and group index is presented and described in detail.

1.4.2 Waveguide Sidewall Bragg Gratings

Chapter 4 explores the design, fabrication, and complete characterization of a collection of sidewall gratings in ultra-low-loss Si_3N_4-core/SiO_2-clad planar waveguides. Through proper geometrical design coupling constant values between 0.2 and 310 cm^{-1} are achieved. The TE waveguide propagation loss of the structures over the wavelength range of 1540 to 1570 nm is below 5.5 dB/m.

1.4.3 Rare-Earth-Ion-Doped Dielectric Lasers

Chapter 6 presents the cavity design, fabrication process, and lasing characterization of an array of rare-earth-ion-doped waveguide distributed Bragg reflector (DBR) and distributed feedback (DFB) lasers on an ultra-low-loss Si_3N_4 platform. Waveguide sidewall gratings providing the lasing feedback are defined in the silicon nitride layer using 248 nm stepper lithography, while the gain is provided by a reactive co-sputtered erbium-doped aluminum oxide layer. Record low optical threshold powers and high slope efficiencies are demonstrated, as are side mode suppression ratios (SMSRs) above 50 dB and emission bandwidths of 40 nm. Finally, a record high temperature operation of 400 ^{o}C with an uncompensated temperature dependent wavelength shift of 1.92 GHz/^{o}C is reported.

1.5 Preview of This Thesis

The work presented within this dissertation demonstrates enabling technology for a new class of optically pumped rare-earth-ion-doped waveguide lasers and amplifiers on an ultra-low loss waveguide platform. Such optical sources demonstrate robust, high temperature operation with stable low noise output over the entirety of the telecommunications C-band while at the same time being fully compatible with modern high volume manufacturing process.

Chapter 2 begins with a discussion on various material systems that comprise modern state of the art integration platforms, with a motivating case presented for the basis set of passive waveguides to be implemented in a dielectric, rather than semiconductor, material. This is then followed up with a discussion on how such dielectric materials can be a benefit for active on-chip devices. Chapter 3 presents the individual integration building blocks developed within this thesis that when combined can eventually comprise a wide variety of functional photonic integrated circuits. Chapter 4 covers the complete analysis and design considerations, fabrication processing, and measurement and characterization of fully passive waveguide devices and components. This includes: weekly guiding buried ridge waveguides, strongly guiding deeply etched waveguides, deep to shallow adiabatic transition sections, waveguide sidewall Bragg gratings, and bus-coupled racetrack ring resonators. Chapters 5 and 6 present the same set of considerations and in-depth engineering analysis as Chapter 4 did for passive components, but instead focus on rare-earth-ion-doped waveguide amplifiers (Chapter 5) and lasers (Chapter 6) instead. Included in Chapter 6 are demonstrations of both distributed Bragg reflector type and distributed feedback type laser cavities. Chapter 7 concludes the dissertation by summarizing all the resulting experimental work contained within the previous chapters. Additionally, future work that address the performance limitations is also discussed to ensure that the technology presented here continues to advance.

1.6 References

[1] Cisco Visual Networking. “Forecast and Methodology, 2015-2020.” White Paper (2016).

[2] D. Vantrease, R. Schreiber, M. Monchiero, M. McLaren, N. Jouppi, M. Fiorentino, A. Davis, N. Binkert, R. Beausoleil, and J. Ahn, “Corona: System Implications of Emerging Nanophotonic Technology,” in 35th International Symposium on Computer Architecture, Beijing, China, 153164 (2008).

[3] C. L. Schow, F. E. Doany, C. Chen, A. V. Rylyakov, C. W. Baks, D. M. Kuchta, R. A. John, and J. A. Kash, “Low-Power 16 x 10 Gb/s BiDirectional Single Chip CMOS Optical Transceivers Operating at << 5 mW/Gb/s/link,” IEEE Journ. of Solid-State Circuits 44(1), 01313 (2009).

[4] C. Ciminelli, F. DellOlio, C. E. Campanella, and M. N. Armenise, “Photonic technologies for angular velocity sensing,” Advances in Optics and Photonics, vol. 2, pp. 370404, Jun. 2010.

[5] R. Osellame, V. Maselli, R. M. Vazquez, R. Ramponi, and G. Cerullo, “Integration of optical waveguides and microfluidic channels both fabricated by femtosecond laser irradiation,” Applied Physics Letters, vol. 90, no. 23, pp. 231118231118, 2007.

[6] D. John, “Etchless Core-Definition Process for the Realization of Low Loss Glass Waveguides,” Ph.D. Dissertation (Department of Electrical and Computer Engineering, University of California Santa Barbara, 2012).

[7] J. Bauters, “Ultra-Low Loss Waveguides with Application to Photonic Integrated Circuits,” Ph.D. Dissertation (Department of Electrical and Computer Engineering, University of California Santa Barbara, 2013).

Chapter 2

Background: Platforms for Photonic Integration

Chip-scale integrated optical components can be categorized into two main classifications according to their core functionality. First, there are passive components which generally facilitate the guiding, directing, and filtering of light in applications such as splitters, couplers, multiplexers, and reflectors. Second, there are active components which generally concern the generation or amplification of an optical signal on a chip. For clarity in terminology, this difference between passive and active components is further illustrated in Figure 2.1.

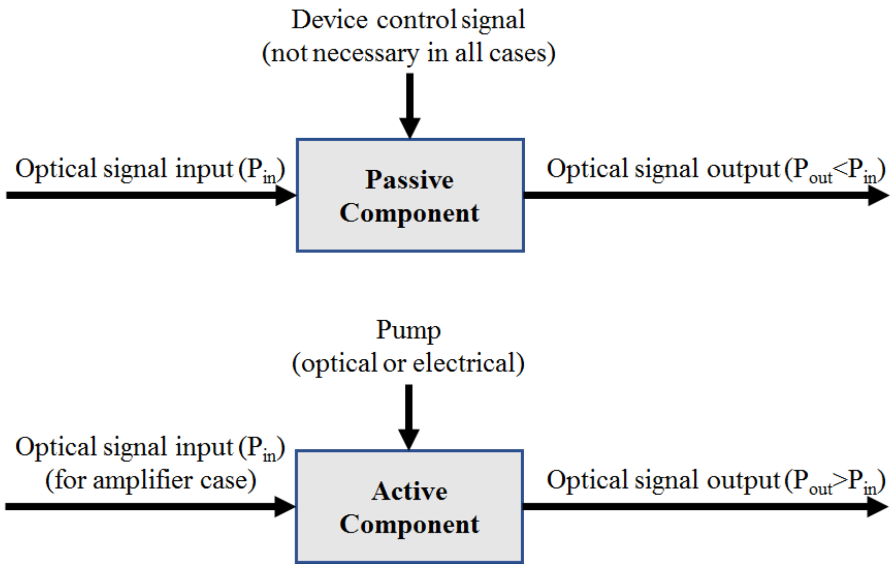

Figure 2.1: *Difference in components that are either 'passive' or 'active' in functionality. 'Passive' components may include an electrical or optical drive signal (such as in the case of a thermally tuned switch), but do not amplify an optical input or produce an optical output spontaneously as an 'active' component does.*

In the micro-electronics world, a broad range of applications can be served through a rather small set of basic building blocks such as transistors, diodes, and interconnection tracks. By connecting these basic building blocks in different topologies and numbers a vast variety of systems and circuits spanning multiple orders of magnitude in complexity can be realized [1]. In photonics a similar analogy holds, where proper design of basic passive and active building blocks can be combined into a broad set of devices and systems, allowing for a broad application space to flourish. This chapter will discuss the engineering considerations that feed into designing such an integration platform.

2.0 Chapter Synopsis

In this chapter, the scope of materials covered within this thesis is set and the relevant background research within this framework is discussed. The overall organizational flow of this chapter is shown schematically in Figure 2.2.

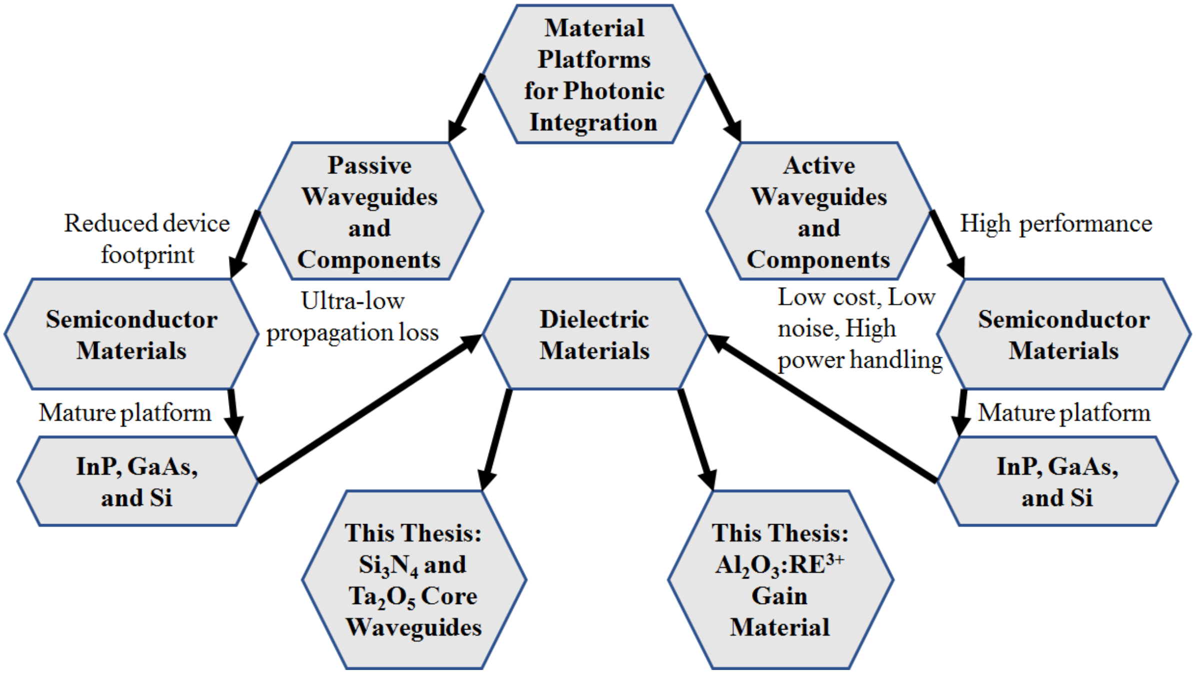

Figure 2.2: *Diagram of the organizational flow of the background research and information contained within this chapter. The rationale for each choice in advancement is written next to each arrow connecting the adjacent subject areas.* RE^{3+}*: rare-earth ion 3+.*

Section 2.1 begins by considering the various competing material platforms commonly utilized for integrated optical systems and devices, with emphasis on selecting a dielectric material type for passive waveguides. Section 2.2 then continues this examination on passive waveguides by covering appropriate choices for waveguide core material. Here Si_3N_4 and Ta_2O_5 are established as the core materials of choice for the work that follows. Section 2.3 again considers various competing material platforms, but this time an emphasis is placed upon active waveguides as both optical signal amplifiers and optical signal generators (lasers) instead of as solely passive sections. A broad range of semiconductor-based background research is presented, with a compelling case made for the use of rare-earth-ion-doped dielectric gain blocks.

2.1 Compound Semiconductor, Silicon, and Dielectric Waveguides: A Case for Dielectric Waveguides

As is discussed in detail in [2], the passive waveguide loss of an integration platform can be a serious constraint on advanced system performance, so much so that a high propagation loss can completely trump the potential advantages in stability, footprint, weight, power consumption, and cost offered by integration. Figure 2.3 gives an overview of the of the planar waveguide propagation losses reported for compound semiconductor, silicon, and dielectric photonics platform waveguides to date.

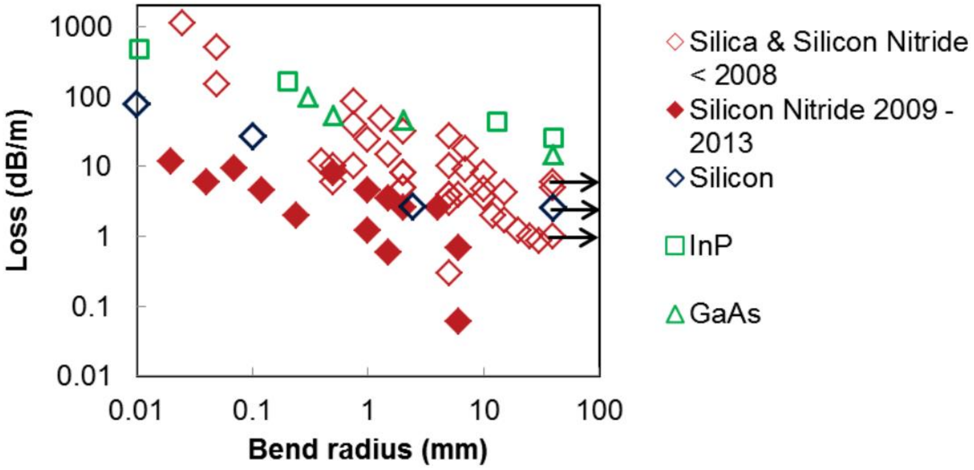

Figure 2.3: *Reported literature values of planar waveguide propagation losses as a function of bend radius. Straight waveguide loss data are shown at 60 mm radius. Figure taken from [3].*

From this collection, two important conclusions can be reached: 1) There is an inherent compromise in waveguide technology between simultaneously obtaining the lowest propagation loss and smallest system footprint, and thus a shift toward the lower left corner of the axes indicates an overall improvement in waveguide technology. 2) With the crucial restrictions placed on overall advanced integrated system performance by waveguide propagation loss, dielectric waveguides can provide a loss of reduction of up to 3 orders of magnitude over a compound semiconductor based alternative and up to 2 orders of magnitude over a silicon based alternative. This degree of loss reduction over competing integration technologies can offer enormous benefits towards overall integrated system efficiency, so long as both passive and active components can properly be designed and exploited. The remainder of this chapter will investigate the current breadth of research into both types of components.

2.2 Ultra-Low Loss Waveguides

Compared to bulk optics and fiber-based systems, photonic integrated circuits can offer improved reliability, efficiency, and stability in a more compact footprint and at a lower cost point. Many targeted PIC applications, for example, optical gyroscope rotational velocity sensors, communication network filters and multiplexers, true-time-delay antenna beam-steering networks, and optical buffers, require long on-chip optical path lengths and/or high quality factor resonators. As performance demands on these applications increase, waveguides with ultra-low propagation loss become necessary [4].

2.2.1 Core Materials

With a wide availability of low cost deposition methods and standard fabrication practices, the following analysis and discussion will focus on the amorphous dielectric materials of SiO_2, Si_3N_4, and Ta_2O_5 as waveguide core materials, with SiO_2 or air acting as a cladding material. These core materials provide low absorption loss over wide wavelength bands and feature the requisite refractive indexes to allow for waveguiding when used in conjunction with an SiO_2 or air cladding.

2.2.1.1 SiO_2

The material qualities and deposition methods of silica thin films make them ideal for use in a variety of applications that require on-chip low-loss optically guiding structures. Thermal SiO_2-based toroidal structures and wedge-shaped whispering gallery mode waveguides have shown impressive performance, with losses in the 0.1-0.01 dB/m regime [5][6][7][8]. Historically, such structures required tapered or bent fiber couplers to efficiently transfer light into their microtoroidal or wedge-shaped geometries, rendering further integration with other photonic components for increased functionality impossible. Within the past year an approach that allows for bus waveguide excitation of such designs has been demonstrated [9], but it remains to be seen if the wet chemical etching fabrication approach of the SiO_2-based features will allow for other functional components to be located on the same substrate. Therefore, an ultra-low loss planar waveguide platform that is suitable for resonator structures, spiral delays, and photonic integration is still required.

The early development of high quality planar waveguides involved a very low index contrast core surrounded by a silica cladding, with a core/cladding Δn of less than 1%, using Ge or P-doped SiO_2 as the core. With such a low Δn, the confinement within the waveguide core needed to be greater than 70% to achieve practical mm-level bend radii [10]. Losses in the 1-0.1 dB/m regime were successfully demonstrated [11], but the minimum allowable bend radius was only 30 mm.

2.2.1.2 Si_3N_4

Stoichiometric silicon nitride has a higher refractive index contrast with SiO_2 than such SiO_2-doped-core materials and offers the benefits of increased material stability and high refractive index regularity. Moreover, Si_3N_4 films deposited with low-pressure chemical vapor deposition (LPCVD) have thicknesses controllable to the nanometer scale and exhibit low (less than 0.4 nm) surface roughness, a quality necessary for maintaining low scattering loss at the top and bottom core-cladding interfaces [4]. Sidewall scattering, the primary contributor to loss in high-index-contrast planar waveguides, can be minimized, however, by using a high-aspect-ratio core geometry in which the width of the waveguide far exceeds the thickness. This allows one to keep the benefits of a stoichiometric material while also attaining low propagation loss. Losses in the 1-0.01 dB/m regime have successfully demonstrate using such a high aspect ratio design [4][12]. Such an ultra-low-loss waveguide (ULLW) platform can take advantage of the high index contrast between silica and silicon nitride to create waveguides that possess sub-millimeter bend radii and sub-dB/cm loss simultaneously. These characteristics enable applications previously supported only by fiber-based components to now be realized with a photonic integrated circuit (PIC) at a lower cost point and a smaller packaging footprint. This thesis will describe a series of waveguide sidewall Bragg gratings that are enabled by this ULLW platform.

2.2.1.3 Ta_2O_5

For all its benefits, the Si_3N_4-core based platform possesses certain limitations that can be addressed through the substitution of Ta_2O_5 as a core material, as described in this work. For example, nonlinear optical processes on photonic chips can be used to generate and process signals all-optically with speeds far superior to electronics. For best performance, such nonlinear processes generally require high mode confinement and dispersion engineering for phase matching [13][14]. Due to its high tensile film stress, depositing thick (>400 nm) layers of Si_3N_4 without cracking has historically proved to be a considerable fabrication challenge [13]. Furthermore, optical absorption in the 1.52 μm wavelength region due to nitrogen-hydrogen (N-H) bond resonances (hydrogen being an undesired impurity incorporated into the Si_3N_4 and SiO_2 films during fabrication) creates a 'floor' on the lowest achievable optical loss within the C-band [12]. Tantalum pentoxide (Ta_2O_5) is a CMOS compatible material that presents the opportunity to address both the requirements for nonlinear interactions and the fundamental loss limitations of Si_3N_4 as a waveguide core material, while at the same time preserving a high index contrast that allows for small bend radii (the refractive index of Ta_2O_5 at 1550 nm is roughly the same as Si_3N_4, 2.05). This thesis will present measurements of weekly guiding shallowly etched Ta_2O_5-core/SiO_2-clad waveguides that demonstrate loss that is both lower than the state of the art for a Ta_2O_5-core waveguide [15] and that demonstrated by a Si_3N_4-core waveguide of an equivalent geometry [4]. These losses are achieved through a refined core deposition and anneal processes, as well as through an optimized waveguide geometry and resulting required etching protocol.

2.3 On-Chip Integrated Lasers

As opposed to optical amplifiers, which concern the amplification of existing optical signals through spontaneous emissions processes, lasers are used for the generation of *new* optical signals through stimulated emission. As a basic concept, a laser cavity has two essential requirements: optical feedback and optical gain. In the case of a waveguide laser the optical feedback is usually provided by means of butt-coupled or end-deposited mirrors (which can be either dielectric of semiconductor-based), or integrated ring resonators or Bragg gratings. In such integrated designs, the resonator feedback is defined at same time a planar or channel waveguide is fabricated within the optical gain medium. Since the optical feedback elements and gain medium can be fabricated from the same material and on a common substrate, waveguide lasers allow for a monolithic design which facilitates stable and robust operation. Another key advantage of waveguide lasers is the fact that there is basically no beam divergence inside the cavity, so that extremely high optical intensities can be maintained over long lengths. This makes it possible to achieve high pump rates, resulting in low-threshold lasing. Monolithic integrated waveguide lasers can be broken down into two main classifications based upon their gain medium: semiconductor lasers and rare-earth-ion-doped dielectric lasers.

2.3.1 Semiconductor Lasers

Semiconductor lasers feature a crystalline semiconductor material as the principle gain medium. For the purposes of this thesis, wavelength ranges of interest will be restricted to the telecommunications O- (13xx nm) and C- (15xx nm) bands, where most laser designs feature a double heterostructure epitaxial layering scheme utilizing the InGaAsP and AlGaInAs quaternary systems.

2.3.1.1 Native Substrate Designs

Driven primarily by the explosive demand in the communications industry, semiconductor lasers, as well as photonic integrated circuits that utilize such lasers as part of their core functionality, based on native compound semiconductor substrates have reached impressive levels of technological performance. An immense variety of laser designs demonstrating elevated temperature operation with minimal performance degradation [1][17], wide tunability (40 nm), low linewidth (2 MHz), and high output power (>10 mW coupled into fiber) simultaneously [18][19] have successfully moved out of the research phase and are available for purchase commercially. The same can be said for photonic integrated circuits for communications and other systems that rely on the same material platforms [21][22][23][24]. While technological progress will undoubtedly continue in this area, further advances in integrated functionality and continued reductions in cost can be facilitated through a change of material system.

2.3.1.2 Heterogeneous-Si Integration

Within the most recent decade, significant attention within the optoelectronics research community has been shifted from compound semiconductor based material systems to silicon.

The main attraction here being the promise of leveraging silicon, with its extensive fabrication infrastructure and wealth of knowledge within its electronics industry, as a means to produce low cost integrated photonic circuits that can finally break the cost barrier of dense photonic systems. Optically pumped designs utilizing stimulated Raman scattering (SRS) in silicon waveguides and bonded III-V crystalline films were demonstrated in the mid-2000s [25][26][27], with an electrically pumped design exploiting the bonded thin film approach following shortly thereafter [28]. Within a brief period following, more complex laser cavity configurations such as distributed feedback lasers [29], racetrack ring lasers [30], and mode-locked lasers [31] were demonstrated by researchers. Photonic integrated circuits based upon this technology are maturing fast as increasingly complex circuits are reported with tens of integrated components, including on-chip lasers [32]. Nevertheless, the passive waveguide loss compared to dielectric alternatives, combined with the two-photon absorption (TPA) limited power handling capabilities of the Si waveguiding layer, have necessitated further innovation in silicon substrate-based optoelectronic devices.

2.3.1.3 Heterogeneous-Si on Ultra-Low-Loss Waveguide Integration

Ultra-low-loss silica-based waveguides (ULLWs) on silicon have propagation losses 100 to 1000 times lower than silicon or III-V based semiconductor waveguides. Additionally, they have demonstrated efficient coupling with optical fibers and reduced sensitivity to fabrication perturbations. However, the ultra-low-loss and native silicon waveguides are very different. The ULLWs support a large mode with a low effective index (~1.5), and the silicon waveguides have a smaller mode with a much higher index (~3.4). In both [33] and [34] approaches that enable the integration and low loss coupling of ultra-low-loss waveguides with heterogenous-Si active elements are detailed. Each leverage low loss and broad bandwidth adiabatic tapered mode converters (sometimes referred to as spot size converters) from the dielectric-based waveguides to the Si-based waveguides. [35] takes this approach an additional step further and manages to successfully integrate eight hybrid III-V/silicon photodetectors and a Si_3N_4-core waveguide-based arrayed waveguide grating router as a demultiplexer. While these results are promising, demonstrating a laser light source has so far proved an extremely complicated endeavor, owing to the heightened fabrication complexity that comes along with requiring two separate wafer bonding steps on top of the 10+ required lithographic patterning steps.

2.3.2 Rare-Earth-Ion-Doped Dielectric Lasers and Amplifiers

Rare-earth-ion-doped dielectric lasers and amplifiers feature an optically-pumped ionic species within a dielectric host material as the principle gain medium. Figure 2.4 provides a simple illustration highlighting the difference in operation between devices that rely on either electrically or optically pumped gain materials.

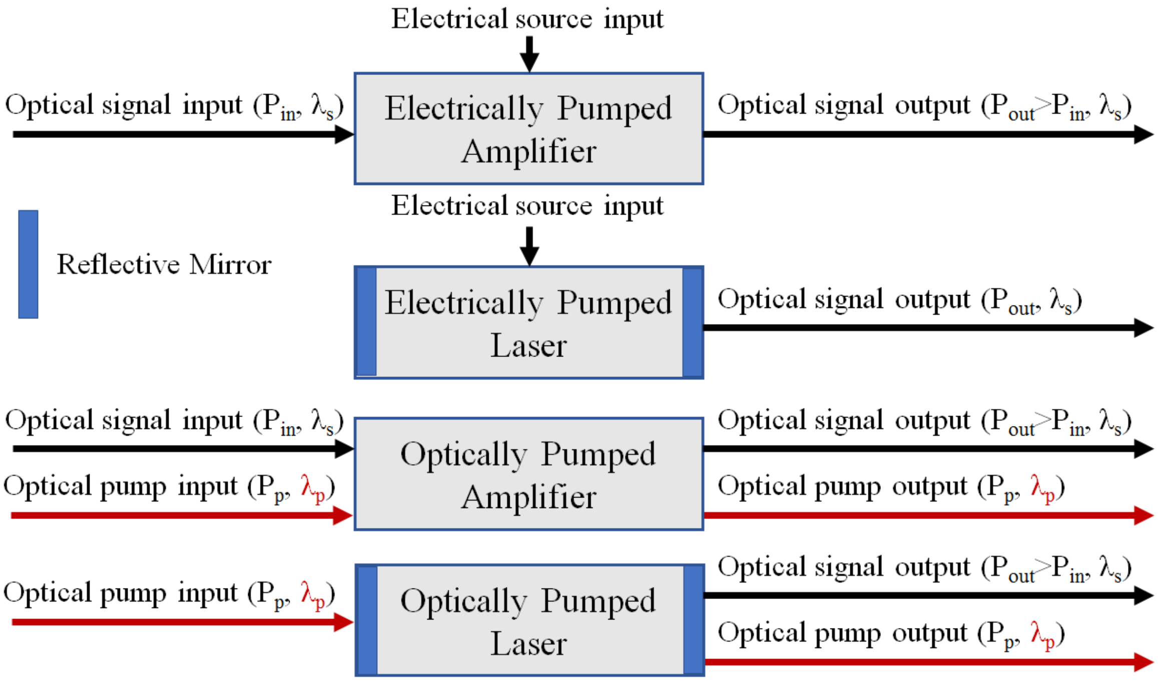

Figure 2.4: *Diagram of electrically pumped optical amplifiers and lasers (top two) vs. optically pumped optical amplifiers and lasers (bottom two). The reflective mirrors for the optically pumped case must allow transmission of the optical pump light at* λ_p *into the cavity to excite the gain medium. The output mirror may be reflective for the pump, allowing a double-pass configuration.*

For the purposes of this thesis, wavelength ranges of interest will be restricted to the telecommunications O- (13xx nm) and C- (15xx nm) bands, where most laser designs feature either erbium (Er^{3+}, 15xx nm) or neodymium (Nd^{3+}, 13xx nm) as the dopant species. In addition to higher output powers and higher demonstrated operating temperatures [36], lasers based on such solid-state gain material have exhibited superior noise performance relative to semiconductor lasers due to their larger intracavity powers, smaller intracavity losses, and negligible gain/index coupling [37].

Early waveguide-based laser and amplifier devices were demonstrated in a variety of glass-based host materials, including lithium niobate ($LiNbO_3$) and phosphate glasses [38][39]. Recently, a reliable, reproducible, and low cost reactive co-sputtering process was developed that allows for high volume rare-earth-ion-doped film deposition of a variety of dopant species on arbitrary substrates, including Si [40]. Further optimization of this technique allowed for the demonstration of on-chip waveguide amplifiers with an 80 nm gain bandwidth, 2 dB/cm peak gain, and 20 dB net gain [41][42]. This was quickly followed by demonstration of monolithic integration between doped active waveguides and Si-based passive waveguides [43]. This thesis details an approach that allows for the exploitation of both this rare-earth-ion-doped gain media deposition technique and the additional benefits of the previously discussed dielectric-based ultra-low-loss waveguides to be combined. The resulting on-chip optically pumped lasers and amplifiers simultaneously demonstrate record low optical pump thresholds, record high temperature operation, and low lasing linewidths, while at the same time being fully amenable to high volume Si manufacturing processes. Additionally, the cavity designs are fully integrable with previously demonstrated fully passive dielectric-based ultra-low-loss waveguides.

2.4 Chapter Summary

This chapter discussed and explored the various available platforms for photonic integration, including those based on either crystalline semiconductor or amorphous glass materials. A case for dielectric-based passive waveguides and rare-earth-ion-doped dielectric-based active waveguides was presented. Chapter 3 will introduce the basic functional integration building blocks that are developed within this thesis, with the remaining chapters delving into greater detail on the analysis, design, fabrication, and characterization of each component.

2.5 References

[1] M. Smit, J. van der Tol, and M. Hill, “Moore’s law in photonics” Laser Photonics Rev. 6, 1-13 (2012).

[2] J. Bauters, “Ultra-Low Loss Waveguides with Application to Photonic Integrated Circuits,” Ph.D. Dissertation (Department of Electrical and Computer Engineering, University of California Santa Barbara, 2013).

[3] M. J. R. Heck, J. F. Bauters, M. L. Davenport, D. T. Spencer, and J. E. Bowers, “Ultralow loss waveguide platform and its integration with silicon photonics.” Laser & Photonics Reviews 8(5), 667-686 (2014).

[4] J.F. Bauters, M.J.R. Heck, D. John, D. Dai, M.-C. Tien, J.S. Barton, A. Leinse, R.G. Heideman, D.J. Blumenthal, and J.E. Bowers, “Ultra-low-loss high-aspect-ratio Si_3N_4 waveguides,” Opt. Express 19(4), 3163-3174 (2011).

[5] T. J. Kippenberg, S. M. Spillane, and K. J. Vahala, “Demonstration of ultra-high-Q small mode volume toroid microcavities on a chip,” Appl. Phys. Lett. 85(25), 6113–6115 (2004).

[6] E. Ostby, “Photonic whispering-gallery resonators in new environments,” Ph.D. Dissertation (Department of Electrical Engineering, California Institute of Technology, 2009).

[7] H. Lee, T. Chen, J. Li, O. Painter, and K. J. Vahala, “Ultra-low-loss optical delay line on a silicon chip,” Nature Comm. 3, 867 (2012).

[8] T. Chen, H. Lee, and K. J. Vahala, "Design and characterization of whispering-gallery spiral waveguides," Opt. Express 22, 5196-5208 (2014).

[9] K. Y. Yang, D. Y. Oh, S. H. Lee, Q.-F. Yang, X. Yi, and K. Vahala, “Integrated Ultra-High-Q Optical Resonator,” arXiv:1702.05076 (2017).

[10] D. Spencer, “Ultra-Narrow Bandwidth Optical Resonators for Integrated Low Frequency Noise Lasers,” Ph.D. Dissertation (Department of Electrical and Computer Engineering, University of California Santa Barbara, 2016).

[11] R. Adar, M. Serbin, and V. Mizrahi, “Less than 1 dB per meter propagation loss of silica waveguides measured using a ring resonator,” J. Lightwave Technol. 12(8), 1369–1372 (1994).

[12] J.F. Bauters, M.J.R. Heck, D.D. John, J.S. Barton, C.M. Bruinink, A. Leinse, R.G. Heideman, D.J. Blumenthal, and J.E. Bowers, “Planar waveguides with less than 0.1 dB/m propagation loss fabricated with wafer bonding,” Opt. Express 19(24), 24090-24101 (2011).

[13] D.J. Moss, R. Morandotti, A.L. Gaeta, M. Lipson, “New CMOS-compatible platforms based on silicon nitride and Hydex for nonlinear optics,” Nature Photon. 7, 597–607 (2013).

[14] J.S. Levy, A. Gondarenko, M.A. Foster, A.C. Turner-Foster, A.L. Gaeta, and M. Lipson, “CMOS-compatible multiple-wavelength oscillator for on-chip optical interconnects,” Nature Photon. 4, 37–40 (2010).

[15] M. Itoh, T. Kominato, M. Abe, M. Itoh, and T. Hashimoto, "Low-Loss Silica-Based SiO_2-Ta_2O_5 Waveguides With Extremely High Δ Fabricated Using Sputtered Thin Films," J. Lightwave Technol. 33, 318-323 (2015).

[16] C. C. Lin, M. C. Wu and W. H. Wang, "Facet coating effects on 1.3 and 1.55 µm strained multiple-quantum-well AlGaInAs/InP laser diodes," in *IEE Proceedings - Optoelectronics*, 146(6) 268-272, (1999).

[17] R. Paoletti et al., "Highly reliable and high yield 1300 nm InGaAlAs directly modulated ridge Fabry-Perot lasers, operating at 10 Gb/s, up to 110°C, with constant current swing," *OFC/NFOEC Technical Digest. Optical Fiber Communication Conference*, 2005.

[18] V. Jayaraman, Z.M. Chuang, and L.A. Coldren, “Theory, Design, and Performance of Extended Tuning Range Semiconductor Lasers with Sampled gratings,” IEEE Jour. of Quant. Electron., 29(6), 1824-1834, (1993).

[19] E. J. Skogen, “Wavelength Agile Photonic Integrated Circuits Using Quantum Well Intermixing,” Ph.D. Dissertation (Department of Electrical and Computer Engineering, University of California Santa Barbara, 2003).

[20] P. W. Juodawlkis et al., "High-Power, Low-Noise 1.5-µm Slab-Coupled Optical Waveguide (SCOW) Emitters: Physics, Devices, and Applications," IEEE Jour. of Sel. Top. in Quant. Electron., 17(6) 1698-1714, (2011).

[21] T. L. Koch and U. Koren, "Semiconductor photonic integrated circuits," IEEE Jour. of Quant. Electron., 27, 641-653 (1991).

[22] M. L. Masanovic, V. Lal, J. A. Summers, J. S. Barton, E. J. Skogen, L. G. Rau, L. A. Coldren, and D. J. Blumenthal, "Widely Tunable Monolithically Integrated All Optical Wavelength Converters in InP," J. Lightwave Technol. 23, 1350 (2005).

[23] D. J. Blumenthal *et al*., "All-optical label swapping networks and technologies," Jour. of Light. Techn., 18(12), 2058-2075 (2000).

[24] M. Lauermann et al., “Multi-Channel, Widely-Tunable Coherent Transmitter and Receiver PICs Operating at 88 Gbaud/16-QAM,” *OFC/NFOEC Technical Digest. Optical Fiber Communication Conference*, 2017.

[25] O. Boyraz and B. Jalali, "Demonstration of a silicon Raman laser," Opt. Express 12, 5269-5273 (2004).

[26] H. Rong, R. Jones, A. Liu, O. Cohen, D. Hak, A. W. Fang, M. Paniccia, “A continuous-wave Raman silicon laser.” Nature, 433, 725–727 (2005).

[27] H. Park, A. W. Fang, S. Kodama, and J. E. Bowers, "Hybrid silicon evanescent laser fabricated with a silicon waveguide and III-V offset quantum wells," Opt. Express 13, 9460-9464 (2005).

[28] A. W. Fang, H. Park, O. Cohen, R. Jones, M. J. Paniccia, and J. E. Bowers, "Electrically pumped hybrid AlGaInAs-silicon evanescent laser," Opt. Express 14, 9203-9210 (2006).

[29] A. W. Fang, E. Lively, Y.-H. Kuo, D. Liang, and J. E. Bowers, "A distributed feedback silicon evanescent laser," Opt. Express 16, 4413-4419 (2008).

[30] A. W. Fang, R. Jones, H. Park, O. Cohen, O. Raday, M. J. Paniccia, and J. E. Bowers, “Integrated AlGaInAs-silicon evanescent racetrack lasers and photodetector,” Optics Express, Vol. 15, Issue 5, pp. 2315-2322, (2007).

[31] B. R. Koch, A. W. Fang, O. Cohen, and J. E. Bowers, “Mode-locked silicon evanescent lasers,” Opt. Express 15, 11225-11233 (2007).

[32] M. J. R. Heck, J. F. Bauters, M. L. Davenport, J. K. Doylend, S. Jain, G. Kurczveil, S. Srinivasan, T. Yongbo, and J. E. Bowers, "Hybrid Silicon Photonic Integrated Circuit Technology," IEEE Jour. of Selec. Top. in Quant. Electron. 19, 6100117 (2013).

[33] J. F. Bauters, M. L. Davenport, M. J. R. Heck, J. K. Doylend, A. Chen, A. W. Fang, and J. E. Bowers, "Silicon on ultra-low-loss waveguide photonic integration platform," Opt. Express 21, 544-555 (2013).

[34] T. Tsuchizawa, K. Yamada, T. Watanabe, S. Park, H. Nishi, R. Kou, H. Shinojima, and S. Itabashi, “Monolithic integration of silicon-, germanium-, and silica-based optical devices for telecommunications applications,” IEEE Journ. of Sel. Top. in Quant. Elec. 17, 516–525 (2011).

[35] M. Piels, J. F. Bauters, M. L. Davenport, M. J. R. Heck, and J. E. Bowers, "Low-Loss Silicon Nitride AWG Demultiplexer Heterogeneously Integrated With Hybrid III–V/Silicon Photodetectors," J. Lightwave Technol. 32, 817-823 (2014).

[36] M. Belt and D. J. Blumenthal, “High Temperature Operation of an Integrated Erbium-Doped DBR Laser on an Ultra-Low-Loss Si3N4 Platform,” in Optical Fiber Communication Conference/National Fiber Optic Engineers Conference 2015, OSA Technical Digest (online) (Optical Society of America, 2015), paper Tu2C.7.

[37] C. Henry, “Theory of the linewidth of semiconductor lasers,” IEEE J. Quantum Electron., vol. 18, no. 2, pp. 259–264, Feb. 1982.

[38] I. Baumann, S. Bosso, R. Brinkmann, R. Corsini, M. Dinand, A. Greiner, K. Sch¨afer, J. S¨ochtig, W. Sohler, H. Suche, and R. Wessel, “Er-doped integrated optical devices in LiNbO3”, IEEE Journal of Selected Topics in Quantum Electronics 2, 355 (1996).

[39] D. L. Veasey, D. S. Funk, N. A. Sanford, and J. S. Hayden, “Arrays of distributedBragg-reflector waveguide lasers at 1536 nm in Yb/Er codoped phosphate glass”, Applied Physics Letters 74, 789 (1999).

[40] K. Wörhoff, J. D. B. Bradley, F. Ay, D. Geskus, T. P. Blauwendraat, and M. Pollnau, “Reliable low-cost fabrication of low-loss Al2O3:Er3+ waveguides with 5.4-dB optical gain,” IEEE J. Quantum Electron. 45(5), 454– 461 (2009).

[41] J. Bradley, L. Agazzi, D. Geskus, F. Ay, K. Wörhoff, and M. Pollnau, "Gain bandwidth of 80 nm and 2 dB/cm peak gain in Al_2O_3:Er^{3+} optical amplifiers on silicon," J. Opt. Soc. Am. B **27**(2), 187-196 (2010).

[42] S. A. Vázquez-Córdova, M. Dijkstra, E. H. Bernhardi, F. Ay, K. Wörhoff, J. L. Herek, S. M. García-Blanco, and M. Pollnau, "Erbium-doped spiral amplifiers with 20 dB of net gain on silicon," Opt. Express 22, 25993-26004 (2014).

[43] L. Agazzi, J. D. B. Bradley, M. Dijkstra, F. Ay, G. Roelkens, R. Baets, K. Wörhoff, and M. Pollnau, “Monolithic integration of erbium-doped amplifiers with silicon-on-insulator waveguides,” Opt. Express 18(26), 27703– 27711 (2010).

Chapter 3

Integration Building Blocks

The resulting overall performance of a fully integrated photonic circuit will ultimately depend upon the design and individual effectiveness of its constituent elements. As is traditionally the case with such engineering endeavors, important compositional trade-offs will arise en route to the optimum PIC or component design per intended application. Thus, it is necessary to develop a proper understanding of the core structure, functionality, and behavior of each individual functional block that will eventually comprise the resulting circuit or device.

3.0 Chapter Synopsis

In this chapter, the main passive and active building blocks that form a basis set of optical transmission, routing, filtering, and amplification functionality on the ultra-low loss waveguide (ULLW) platform [1][2] are discussed: passive waveguide delays, waveguide sidewall gratings and filters, and bus-coupled ring resonators, as well as active rare-earth-ion-doped waveguide amplifiers. These building blocks are then combined to create a novel set of high performance distributed feedback and distributed Bragg reflector lasers, in addition to a series of deeply etched tight bend radius racetrack ring resonators. The demonstration of these rare-earth-ion-doped waveguide amplifiers and lasers represents the first time light amplification and transmission capabilities have been integrated within the ULL waveguide platform.

3.1 Passive Components

3.1.1 Waveguide Delays

To realize their requisite complex functionality, all photonic integrated circuits need to interconnect multiple and varied components. This requires that the optical signals be routed throughout the various functional elements on chip. As will be outlined below, both a buried ridge-type and a deeply etched-type waveguiding scheme can be employed, with each separate design featuring different specific applications to which their single optical mode geometry is tailored towards. Within the specific material platform constraints of the ULL waveguide platform this means that due to the lower required extent of etching during the fabrication process, the buried ridge waveguide implementation demonstrates a lower measure of waveguide propagation loss than its deeply etched counterpart. Such a design comes at the expense of a larger minimum bend radius though, which is where the deeply etched waveguide implementation finds its niche. From a PIC design perspective having both types of waveguide available depending upon the circuit's operational objective is best, which is why the additional development step of adiabatic mode converters, or deep to shallow transition sections, was taken. Such components allow for coupling between the two disparate waveguide elements with low reflection and extraneous scattering loss. A schematic of each of these different waveguide types, as well as the adiabatic transition region between, is shown in Figure 3.1.

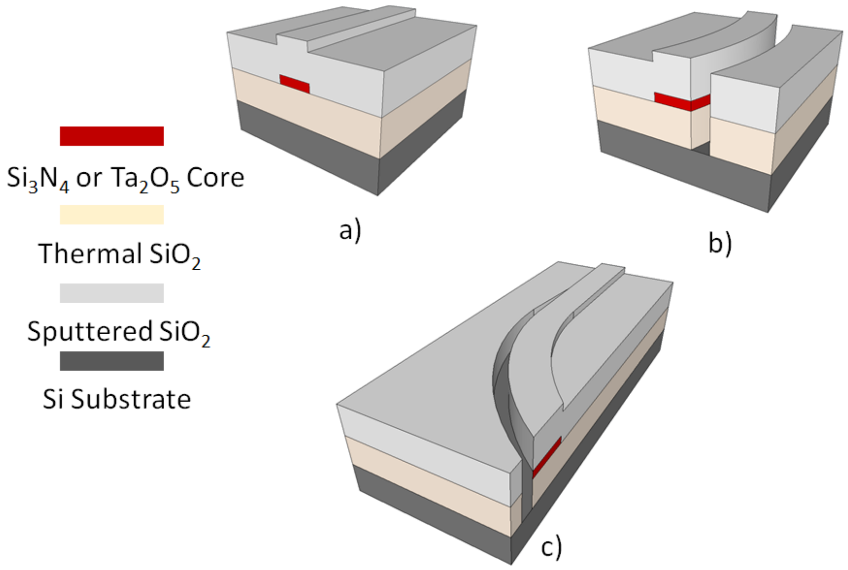

Figure 3.1: *Three-dimensional schematic representation of (a) a weekly guiding buried ridge waveguide, (b) a strongly guiding deeply etched waveguide, and (c) an adiabatic transition region that joins the two waveguide geometries from (a) and (b).*

Specific implementations of each design, complete with optical mode profiles and exact dimensions will be given in Chapter 4. Due to the similarities in their optical properties, either Ta_2O_5 or Si_3N_4 can be used as a core material for such waveguide designs. This will be covered in further detail in Chapter 4.

3.1.1.1 Weekly Guiding Buried Ridge Waveguides

Figure 3.1a shows a weekly guiding buried ridge waveguide, which consists of a buried Si_3N_4 or Ta_2O_5 core material surrounded by a thermal SiO_2 lower cladding layer and a sputtered SiO_2 upper cladding layer, all still present on the host Si substrate. The main advantage of such a waveguide geometry is that its high single-mode aspect ratio (width:thickness) design can achieve extremely low loss values [3] through the combination of optimized material properties and a low sidewall roughness etch step. The exact dimensions and composition of the buried ridge waveguide will determine the overall magnitude of index contrast for this structure. Bends can also be realized in this platform; however, they cannot be very compact (<250 μm bend radius), due to the small index contrast of the shallow etch. Bend radii on the order of 5-10 mm are generally used [5][6].

3.1.1.2 Strongly Guiding Deeply Etched Waveguides

Figure 3.1b shows a strongly guiding deeply etched waveguide, which consists of a buried Si_3N_4 or Ta_2O_5 core material clad by SiO_2 transversely and by air laterally. This combination provides the largest index contrast possible and allows for very compact components (due to the tight <100 μm bends) to be designed. While such a deep SiO_2 etching step commonly is done through a wet etching process [7] to achieve low sidewall roughness values, such an approach will cause a wedged sidewall profile due to the isometric behavior of the wet etchant. Chapter 4 describes a Ti hard-mask process that leverages an inductively-coupled plasma (ICP) etching procedure that results in a highly vertical sidewall profile, while at the same time keeping the sidewall roughness values low to achieve low optical propagation loss.

3.1.1.3 Deep to Shallow Transition Sections

Figure 3.1c shows both a weekly guiding buried ridge waveguide and a strongly guiding deeply etched waveguide interfaced to one another through an adiabatically tapered transition section. Such a taper structure couples light very efficiently between the two waveguide types and minimizes any reflections that could cause a detriment to overall PIC performance.

3.1.2 Waveguide Sidewall Gratings and Filters

Figure 3.2 depicts the structure of an integrated waveguide sidewall Bragg grating filter. A fine-period corrugation etched into the surface of an otherwise uniform waveguide creates a coupling between the forward- and backward-traveling light in the structure. The grating reflects light in a tailored wavelength range, centered at the so-called Bragg wavelength. As such, the Bragg grating forms a convenient implementation of an integrated optical bandpass filter.

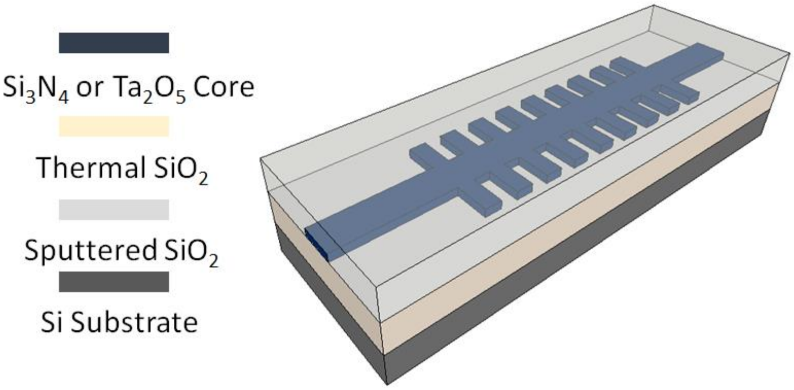

Figure 3.2: *Three-dimensional diagram of an integrated waveguide sidewall optical Bragg grating.*

The integrated sidewall Bragg gratings here offer several advantages over their fiber counterparts, with chief among them being fabrication precision. The beginning and end of the Bragg grating can be sharply delineated rather than continuously tapered and abrupt phase shifts can be introduced at any point in the grating, allowing for section by section control over the design.

As with the passive waveguide delays discussed above, specific implementations of each grating design, complete with optical mode profiles and exact dimensions will be given in Chapter 4. Due to the similarities in their optical properties, either Ta_2O_5 or Si_3N_4 can be used as a core material for such grating designs. This will be covered in further detail in Chapter 4.

3.1.3 Bus-Coupled Racetrack Ring Resonators

Figure 3.3 depicts the structure of an integrated bus-coupled racetrack ring resonator. The directional coupler structure, as opposed to the traditional single bus waveguide coupler, allows for an additional degree of design flexibility of the magnitude of coupling over a broad wavelength range between the input/output waveguide and the central ring resonator.

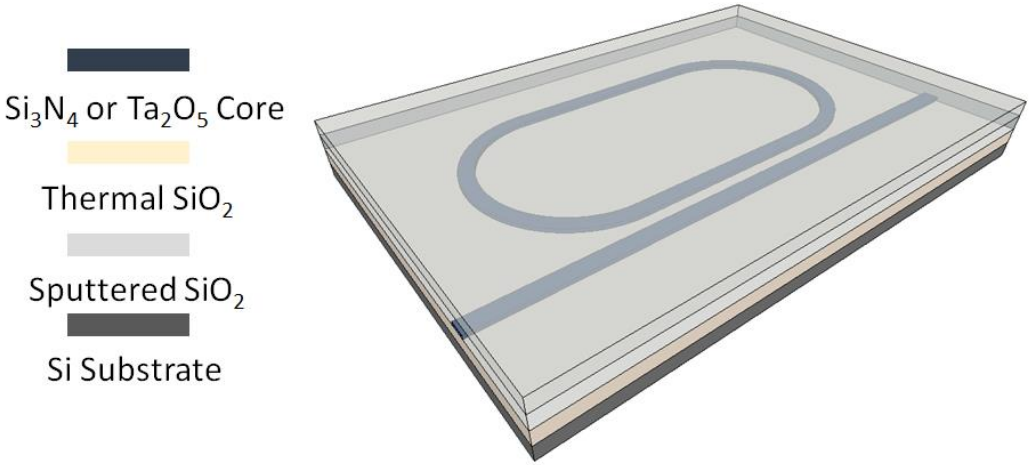

Figure 3.3: *Three-dimensional graphic of an integrated bus-coupled racetrack ring resonator.*

The transmission spectrum of the bus waveguide with a single ring resonator will show dips around the ring resonances. This way, the ring resonator behaves as a spectral filter, which can be used for applications in optical communication, especially wavelength division multiplexing (WDM). Alternatively, these ring spectra can be used for sensing, as the shape of the resonance dips are very sensitive to a variety of effects, which can be detrimental (stability of a filter) or advantageous (as a sensor, or for tuning) [8].

As with the passive waveguide delays discussed above, specific implementations of each ring design, complete with optical mode profiles and exact dimensions will be given in

Chapter 4. Due to the similarities in their optical properties, either Ta_2O_5 or Si_3N_4 can be used as a core material for such ring designs. This will be covered in further detail in Chapter 4.

3.2 Rare-Earth-Ion-Doped Dielectric Active Components

3.2.1 Rare-Earth-Ion-Doped Waveguide Amplifiers

Figure 3.4 gives the structure of an integrated rare-earth-ion-doped waveguide amplifier, implemented within the framework of the ULLW platform. Here, amorphous aluminum oxide (Al_2O_3), is utilized as the host material for the rare-earth (RE) ions that when optically excited through a pump beam will luminesce in the desired applicable wavelength range. For devices operating in the telecommunications C-band, the dopant erbium (15xx nm, Er^{3+}) is used, while for devices operating in the telecommunications O-band, the dopant neodymium (13xx nm, Nd^{3+}) is used. This material (Al_2O_3) has been widely studied as a gain medium for optically-pumped active devices by various research groups over the past several decades [9][10][11][12][13], so little material development work must be done to harness its optical properties for use within the ULL waveguide platform.

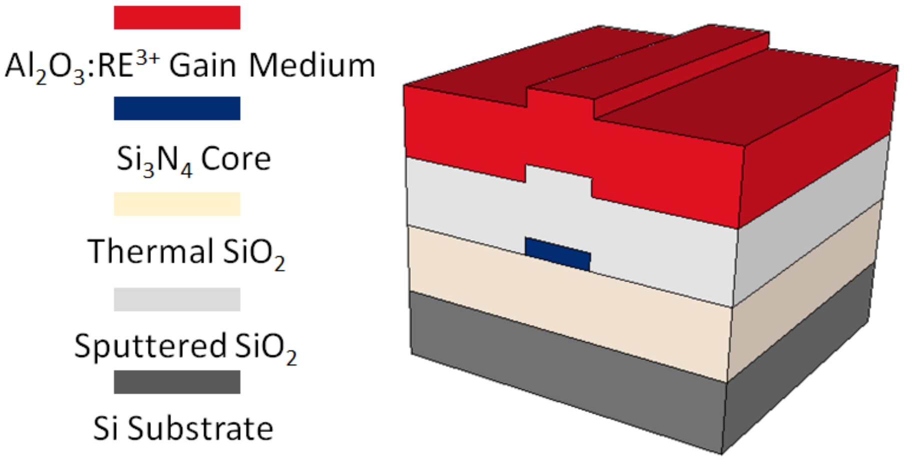

Figure 3.4: *Three-dimensional schematic representation of a waveguide-based rare-earth-ion-doped amplifier. The RE-ion containing gain layer is deposited by a reactive co-sputtering process.*

Specific implementations of the amplifier component design, complete with optical mode profiles and exact dimensions will be given in Chapter 5.

3.2.2 Active Mirror Distributed Bragg Reflector (DBR) Lasers

Figure 3.5 shows the device architecture of an integrated rare-earth-ion-doped waveguide distributed Bragg reflector laser with active mirrors. The lasing cavity can be considered analogous to a standard traditional Fabry-Pérot cavity, but here instead of traditional reflector approaches, the lithographically defined waveguide sidewall grating mirrors allow for precise cavity and reflector definition.

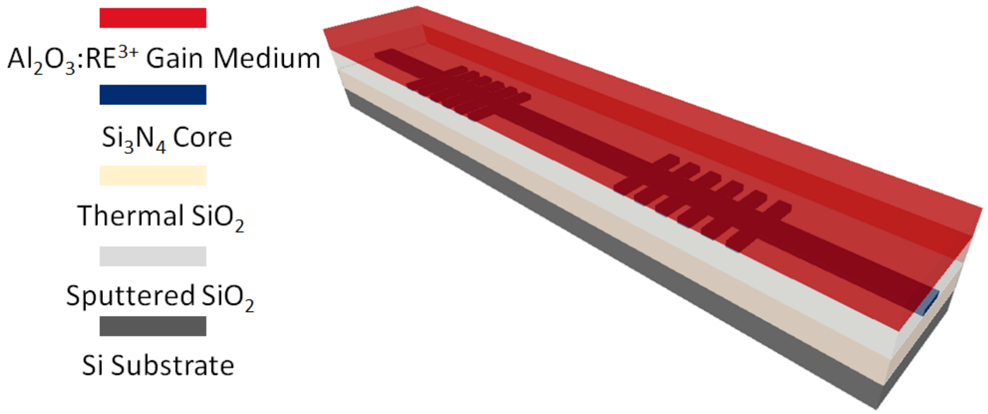

Figure 3.5: *Three-dimensional diagram of a waveguide-based rare-earth-ion-doped distributed Bragg reflector laser cavity. Due to the lithographic nature of the cavity construction, both mirrors can be independently designed to optimize lasing performance. Here the* Al_2O_3*:RE*$^{3+}$ *gain medium is deposited over both the central cavity section and the mirror sections on the device input and output.*

In addition to its stand-alone performance and ease of fabrication advantages, another interesting prospect of such a device is the potential for monolithic integration with other shared components on the ULLW platform. This would enable novel photonic integrated circuits for various applications in wavelength division multiplexed networks, sensing, and optical signal processing. Specific details of the laser device design, complete with optical mode profiles and exact cavity and reflector dimensions will be given in Chapter 6.

3.2.3 Distributed Feedback (DFB) Lasers

Figure 3.6 presents the device geometry of an integrated rare-earth-ion-doped waveguide distributed Bragg reflector laser. With the lithographically defined waveguide sidewall gratings allowing for precise definition of cavity parameters, the central quarter wavelength shift region can be fabricated abruptly (as depicted in Figure 3.6), or in a distributed manner using apodization techniques. Furthermore, by placing the phase shift asymmetrically with respect to the center of the cavity, a bias of the laser outcoupling can be attained in a preferential direction of the cavity.

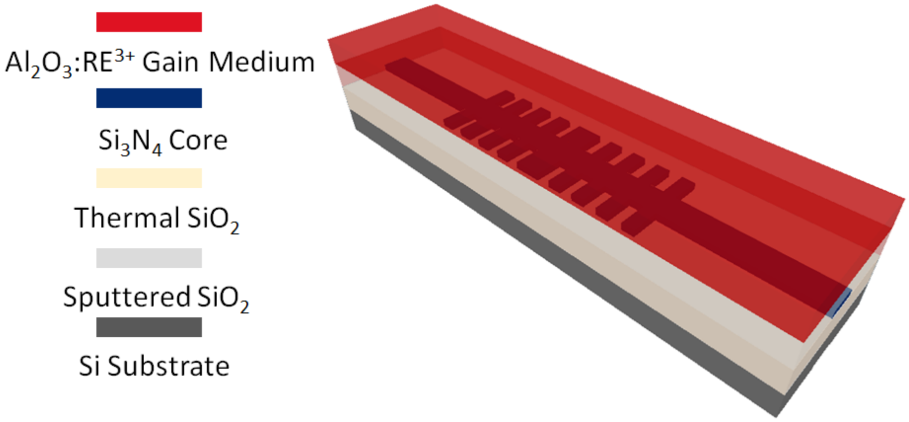

Figure 3.6: *Three-dimensional graphic of a waveguide-based rare-earth-ion-doped distributed feedback reflector laser cavity. The* $\lambda/4$ *phase shift section is visible in the central region of the device.*

Such a rare-earth-ion-doped DFB laser design, along with its previously detailed DBR laser complement, are the first demonstrations of light generation functionality on the ultra-low loss waveguide platform. Specific details of the laser device design, complete with optical mode profiles and exact cavity and reflector dimensions will be given in Chapter 6.

3.3 Chapter Summary

In this chapter, the basic functional integration building blocks detailed within this thesis were presented and surveyed. Each of these components or devices form a basis set of functional elements within the ultra-low loss waveguide platform. The most essential elements, passive weekly confined and strongly guiding passive waveguides delays, as well as an adiabatic tapered transition region between the two, were shown first. To realize low propagation loss in such structures, an emphasis needs to be placed on the quality of the etch step during fabrication to ensure that low sidewall roughness is achieved. Next, passive waveguide sidewall Bragg gratings, as well as bus-coupled racetrack ring resonators were introduced. Both structures can be leveraged for lithographically defined wavelength selective filtering, resonator mirror construction, or lasing cavity definition. Finally, an optically-pumped active rare-earth-ion-doped waveguide amplifier component was presented, with a straightforward geometrical construction allowing for ease of integration with other ULLW platform elements. As was shown, this active section can be integrated with the waveguide sidewall grating mirrors to fabricate a new class of on-chip laser in either a distributed Bragg reflector or distributed feedback construction.

3.4 References

[1] J. Bauters, “Ultra-Low Loss Waveguides with Application to Photonic Integrated Circuits,” Ph.D. Dissertation (Department of Electrical and Computer Engineering, University of California Santa Barbara, 2013).

[2] J.F. Bauters, M.J.R. Heck, D. John, M.-C. Tien; A. Leinse, R.G. Heideman, D.J. Blumenthal, and J.E. Bowers, "Ultra-low loss silica-based waveguides with millimeter bend radius," in Optical Communication (ECOC), *2010 36th European Conference and Exhibition on,* (2010).

[3] J.F. Bauters, M.J.R. Heck, D. John, D. Dai, M.-C. Tien, J.S. Barton, A. Leinse, R.G. Heideman, D.J. Blumenthal, and J.E. Bowers, “Ultra-low-loss high-aspect-ratio Si_3N_4 waveguides,” Opt. Express 19(4), 3163-3174 (2011).

[4] S. Gundavarapu, T. Huffman, M. Belt, R. Moreira, J. Bowers, and D. Blumenthal, “Integrated Ultra-Low-Loss Silicon Nitride Waveguide Coil for Optical Gyroscopes,” in *Optical Fiber Communication Conference*, OSA Technical Digest (online) (Optical Society of America, 2016), paper W4E.5.

[5] R. Moreira, S. Gundavarapu, and D. Blumenthal, "Compact programmable monolithically integrated 10-stage multi-channel WDM dispersion equalizer on low-loss silicon nitride planar waveguide platform," *2015 Optical Fiber Communications Conference and Exhibition (OFC),* Los Angeles, CA, (2015).

[6] R. Moreira, “Integrated Optical Delay Line Circuits on a Ultra-low Loss Planar Waveguide Platform,” Ph.D. Dissertation (Department of Electrical and Computer Engineering, University of California Santa Barbara, 2016).

[7] H. Lee, T. Chen, J. Li, K. Y. Yang, S. Jeon, O. Painter, and K. J. Vahala, “Chemically etched ultrahigh-Q wedge-resonator on a silicon chip,” Nature Photonics 6, 369-373 (2012).

[8] W. Bogaerts, P. De Heyn, T. Van Vaerenbergh, K. De Vos, S. Kumar Selvaraja, T. Claes, P. Dumon, P. Bienstman, D. Van Thourhout, and R. Baets, “Silicon microring resonators,” Laser & Photon. Rev. 6, 47-73 (2012).

[9] G. N. van den Hoven, R. Koper, A. Polman, C. van Dam, J. W. M. van Uffelen, and M. K. Smit, “Net optical gain at 1.53 μm in Er-doped Al_2O_3 waveguides on silicon,” Appl. Phys. Lett. 68, 1886-1888 (1996).

[10] R. Serna and C. N. Alfonso, “In situ growth of optically active erbium doped Al_2O_3 thin films by pulsed laser deposition,” Appl. Phys. Lett. 69, 1541-1543 (1996).

[11] S. Musa, H. J. van Weerden, T. H. Yau, and P. V. Lambeck, “Characteristics of Er-doped Al_2O_3 films deposited by reactive co-sputtering,” IEEE Journ. Of Quant. Elec. 36, 194-196 (2000).

[12] J. Bradley, L. Agazzi, D. Geskus, F. Ay, K. Wörhoff, and M. Pollnau, "Gain bandwidth of 80 nm and 2 dB/cm peak gain in Al_2O_3:Er^{3+} optical amplifiers on silicon," J. Opt. Soc. Am. B **27**(2), 187-196 (2010).

[13] J. Yang, “Neodymium-doped Waveguide Amplifiers and Lasers for Integrated Optical Applications,” Ph.D. Dissertation (Department of Electrical Engineering, Mathematics, and Computer Science, University of Twente, 2010).

Chapter 4

Si_3N_4 and Ta_2O_5 Passive Waveguide Components

For a feasible and practical low loss waveguide technology platform, there are three essential requirements that must be met [1]. First, in the interest of device packaging, application performance, and most importantly cost, the on-chip footprint of a photonic integrated circuit should be as flexible as possible. With the current high cost estimates for multi-project wafer (MPW) fabrication runs, available waveguide designs should be able to conserve real estate (through minimization of bend radius) when required, while at the same time achieving as low of a propagation loss as possible. Secondly, the fabrication of a planar lightwave circuit should be both uniform and reproducible over this same range of on-chip area. Specific target applications, such as integrated waveguide optical gyroscopes [2], receive a performance benefit from an increased device area. In such a device, optical waveguides must have uniform loss and scattering characteristics over the entirety of the centimeter scale diameter of the circular gyroscope coil. Finally, to meet demands of complex higher functionality, multiple passive components should exist and be integrable with one another.

4.0 Chapter Synopsis

This chapter details the complete analysis, design, fabrication, and characterization of a number of passive waveguide components that meet all three necessary specifications outlined above. Table 4.1 lists all components detailed. The weakly and strongly guiding waveguide sections as well as the transitions between the two types will be used in a variety of applications, including microwave signal generation, where optical amplification will not be available. For this reason, it is crucial to reduce the optical propagation loss as much as possible. The waveguide sidewall Bragg gratings can demonstrate immediate use as low-linewidth laser resonator mirrors (which benefit from coupling constants below 10 cm^{-1}) and as part of grating-assisted directional couplers (which benefit from the increased bandwidth provided by larger coupling constants [3]).

Table 4.1: *Passive components developed within this chapter, as well as their respective design requirements for the applications discussed above.*

Waveguide Component	Design Requirement
Weekly guiding buried ridge waveguide	Propagation loss <5 dB/m, minimum bend radius <1 mm
Strongly guiding deeply etched waveguide	Propagation loss <70 dB/m, minimum bend radius <100 μm
Deep to shallow waveguide transition	Loss of <1 dB/transition
Waveguide sidewall Bragg grating	Coupling constants between 0.1-200 cm^{-1}

Section 4.1 begins with a discussion on the similarities in designing waveguides that feature either Si_3N_4 or Ta_2O_5 as a core material. Section 4.2 presents the analysis and design of two different classes of waveguide: an ultra-low loss weekly guiding buried ridge and a tightly confined low bend radius deeply etched ridge. Additionally, a tapered waveguide transition section is presented that allows for effective low loss mode conversion between the deep and shallowly etched waveguides. Section 4.3 covers the coupled mode theory and T-matrix formalism required to design a new class of waveguide sidewall grating reflector, while Section 4.4 details the analysis required to design passive bus-coupled ring resonators. Section 4.5 outlines the fabrication of each of these components, with special emphasis given to the optimization of both the sidewall grating lithography and the deep SiO_2 etch protocol. In Sections 4.6, 4.7 and 4.8 the fabricated waveguides and components are then characterized to quantify their optical performance. Section 4.6 demonstrates record ultra-low loss Ta_2O_5-core waveguides with losses as low as 3±1 dB/m across the entire telecommunications C-band z,

deeply etched waveguides with a bend radius down to 62.5 μm and losses in the 70 dB/m range across the entire telecommunications O-band, and tapered waveguide mode converters with losses as low as 0.6 dB/transition. Section 4.7 describes the measurement of waveguide sidewall gratings in Si_3N_4 with a vast range of coupling constants between 0.19 and 310 cm^{-1} [4][5]. Finally, Section 4.8 presents the measurements of bus-coupled racetrack ring resonators that feature both the deeply etched waveguides and tapered waveguide mode converters.

4.1 Si_3N_4 and Ta_2O_5 - Passive Design Similarities

Tantalum pentoxide (Ta_2O_5) is a CMOS compatible material [6][7] that presents the opportunity to address both the requirements for nonlinear interactions and the fundamental loss limitations of Si_3N_4 as a waveguide core material, while at the same time preserving a high index contrast that allows for small bend radii (the refractive index of Ta_2O_5 at 1550 nm is roughly the same as Si_3N_4, 2.05). Furthermore, the broadband transparent nature of the material means that it is suitable for wavelengths spanning the ultraviolet to the long wavelength infrared (300-8000 nm) [8]. Due to the material's extremely large band-gap value (3.8 eV), two-photon absorption (TPA) and TPA-induced free-carrier absorption are of little to no concern when operating Ta_2O_5-based devices at high powers. Finally, due to the low value of film stress of Ta_2O_5 when compared to a Si_3N_4-core based alternative (100 MPa for Ta_2O_5 vs. 800 MPa for stoichiometric LPCVD Si_3O_4), fabricating thick, high mode confinement waveguides will be less of a fabrication challenge. By sheer serendipity, the similarity in refractive index between Si_3N_4 and Ta_2O_5, coupled with the aforementioned additional benefits of Ta_2O_5 as a core material, means that substitution of the Si_3N_4-core in the ultra-low loss waveguide platform by Ta_2O_5-core will only create tertiary fabrication issues, with the majority of the optical design steps being unchanged [1].

4.2 Waveguide Delays

In a photonic integrated circuit, waveguides delays are the “wires” used to route the generated or coupled on-chip optical signals. While the choice of integration platform (as discussed in Chapter 3) forms the basis material layer framework of the waveguides in the active or passive component sections, the lateral component of the waveguide cross-sectional geometry is mainly determined by the structural etch profile design. Most commonly waveguide structures are classified as either weekly guiding or strongly guiding according to the degree of lateral mode confinement present [9], with the possibility of mode transference between such geometries existing though adiabatic transitions. The following sections give insight into the design and analysis of each of these waveguide elements (weekly guiding sections, strongly guiding sections, and adiabatic mode transitions) featured in this work.

4.2.1 Weekly Guiding Buried Ridge Waveguides

The history of optical fiber loss reduction suggests that a large modal overlap with undoped silica is a path to ultra-low propagation loss [10]. Following this fiber-based loss reduction analogy, the Si_3N_4-core based ultra-low loss waveguide platform was developed after extensive effort [1]. The following section presents some of the analysis and design considerations necessary to achieve the high magnitude of loss reduction demonstrated as compared to competing waveguide geometry alternatives.

4.2.1.1 Analysis and Design

The cross-sectional geometry and material stack for such weekly guiding buried ridge waveguides follow the loss reduction and photonic integration approach reported in [11] and [12]. With Si_3N_4 and Ta_2O_5 having roughly equivalent optical indexes of refraction, the majority of the waveguide design rules for Si_3N_4 core structures will also apply to waveguides featuring a Ta_2O_5 core (as described in Section 4.1). In general, when designing a waveguide cross section to minimize loss, there is an inherent compromise between optical confinement and core/cladding interfacial scattering loss. This trade-off manifests itself as an optimization between the lowest possible waveguide bend radius (as a practical matter given available on-chip PIC real estate) and the largest reduction in interfacial scattering loss contributions. When considering nonlinear applications, a high degree of optical confinement within the waveguide core is desirable, but this design parameter comes at the expense of an acute sensitivity to waveguide core sidewall scattering.

For planar waveguides, the roughness value at the waveguide sidewall due to optimized dry etching is typically an order of magnitude larger than that of the roughness value for the deposited top/bottom interfaces (1-10 nm vs. <1 nm on average). This implies that the optimum lowest loss single-mode core geometry for a given bend radius has the highest single-mode aspect ratio (width:thickness). Here 90 nm Ta_2O_5 core thickness is chosen, with a width of 2.8 μm (the widest possible single-mode core width for the given core thickness). This high aspect ratio design (width:thickness > 10:1) ensures the waveguide will support only a single spatial mode in the C-band, while at the same time allowing tight (<1 mm with no additional loss penalty) bends. Figure 4.1a and Figure 4.1b give a schematic representation of the cross section of the waveguide, while Figure 4.1c shows the simulated

(FIMMWAVE by Photon Design) transverse electric (TE) polarized optical mode profile for the 1590 nm wavelength.

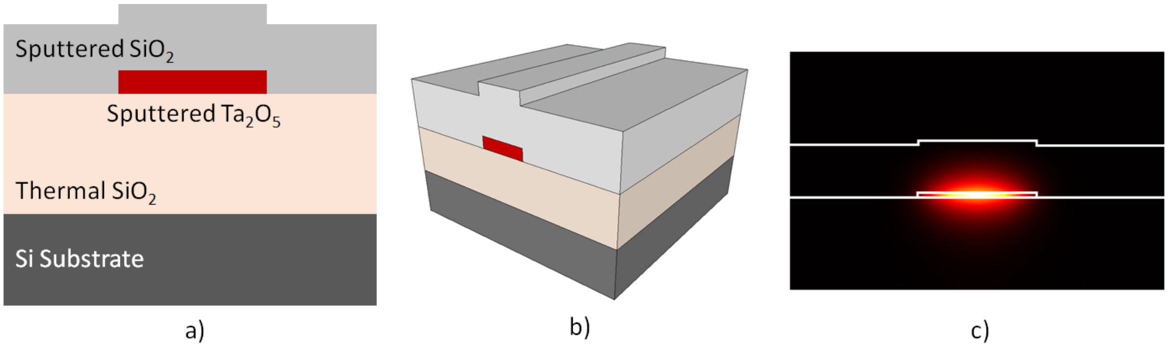

Figure 4.1: *(a) Cross-sectional geometry of the weekly guiding Ta_2O_5-core/SiO_2-clad waveguide. The thermal SiO_2 lower cladding, Ta_2O_5 core, and sputtered SiO_2 upper claddings layers are 15 μm, 90 nm, and 1.1 μm thick, respectively. The width of the Ta_2O_5 core is 2.8 μm. (b) Three-dimensional schematic image of the geometry. (c) Simulated (FIMMWAVE) optical mode profile of the fundamental TE waveguide mode at the 1.55 μm wavelength. The calculated modal intensity diameters ($1/e^2$) are 2.7 μm in the horizontal by 1.1 μm in the vertical. These dimensions were confirmed experimentally through facet imaging utilizing an infrared camera. The calculated core confinement factor (Γ) is 0.15 and the effective index (n_{eff}) is 1.474.*

The transverse magnetic (TM) polarized mode for such a geometry will have a lower confinement factor within the waveguide core (larger modal cross-sectional area) and thus a larger critical bend radius. The critical bend radius is defined as the radius at which the total propagation loss is dominated by the contribution from bend loss, rather than from material or interfacial scattering losses.

4.2.2 Strongly Guiding Deeply Etched Waveguides

A deeply etched waveguiding structure creates a very ‘strong’ lateral optical mode confinement by way of leveraging a substantial magnitude etch-induced index discontinuity. Such a design allows for the fabrication of very sharp waveguide bends without causing any radiation losses. The optical mode traveling through a circular waveguide bend travels at different speeds at different radial distances from the axis of propagation. This can be represented by a transformation of the lateral index profile [13]. As expected, this distorted index profile results in a distortion of the optical mode shape. The optical mode tends to shift towards the outer edge of the waveguide, with the degree of shifting increasing for progressively smaller bend radii.

4.2.2.1 Analysis and Design

Figure 4.2a and Figure 4.2b give a schematic representation of the cross section of a deeply etched waveguide, while Figure 4.2c shows the simulated (FIMMWAVE by Photon Design) transverse electric (TE) polarized optical mode profile for the 1340 nm wavelength. Here a deep SiO_2 etching protocol was employed to create a deep trench with the thermal oxide lower cladding. The following sputtered Al_2O_3 deposition has some residual sidewall coverage, as pictured on the immediate right edge of the Si_3N_4 waveguide. It is also obvious from the simulated mode profile that the 62.5 μm bend radius is distorting the optical mode by shifting it towards the outer edge of the waveguide.

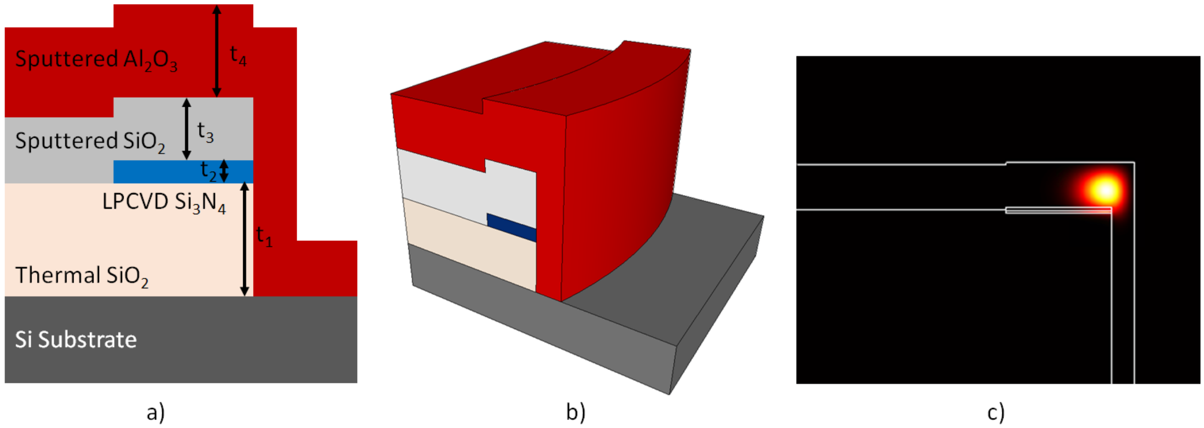

a) b) c)

Figure 4.2: *(a) Cross-sectional geometry of a strongly guiding* Si_3N_4*-core/*SiO_2*/*Al_2O_3*-clad waveguide. The respective layer thicknesses are as follows:* $t_1 = 6.0\ \mu m$, $t_2 = 0.08\ \mu m$, $t_3 = 0.1\ \mu m$, $t_4 = 1.5\ \mu m$*. The width of the* Si_3N_4*-core is 2.8 μm. Due to the nature of the sputter deposition step, 40% of the thickness of the* Al_2O_3 *upper cladding will be deposited on the deeply etched* SiO_2 *sidewall. (b) Three-dimensional schematic image of the geometry. (c) Simulated optical mode profile (FIMMWAVE) of the fundamental TE waveguide mode at the 1.34 μm wavelength with a waveguide lateral bend radius of 62.5 μm. The simulated effective index (*n_{eff}*) is 1.566.*

The large index discontinuity between the Al_2O_3 cladding and air at the right boundary successfully guides the mode around the tight bend. Analysis of the bend loss and confinement factor of this structure for a variety of different bend radii is given in Figure 4.3. Such a small bend radius (down to 62.5 μm) allows for significant area reduction in a variety of optical circuits and devices that employ waveguide bends, including ring resonator structures.

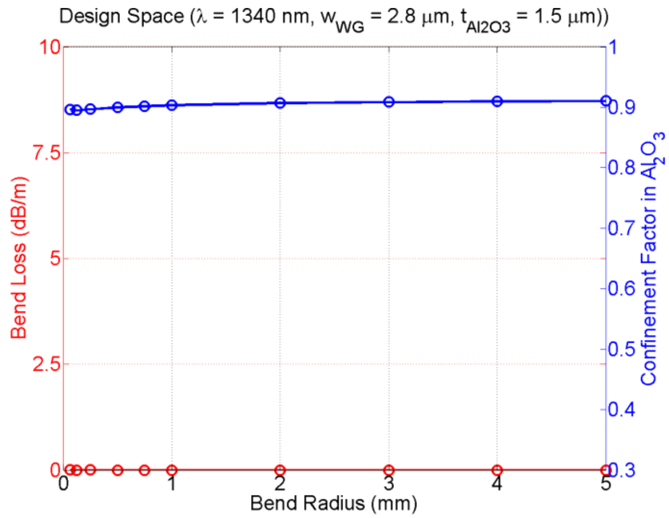

Figure 4.3: *Simulated (FIMMWAVE) bend loss and mode confinement factor in the* Al_2O_3 *cladding for the design presented in Figure 4.2. As the bend radius decreases from the millimeter scale down to the tens of micrometer scale the bend loss shows no appreciable increase and the mode stays within the lateral confines of the 1.5* μm *thick* Al_2O_3 *layer.*

4.2.3 Deep to Shallow Transition Sections

To avoid a sudden discontinuity between the two types of waveguides (shallow and deeply etched), which could cause reflection and scattering of the optical signal, adiabatic tapered transition regions between the two become crucial propagation elements. Such structures allow for efficient optical coupling between waveguide types, and thus expand the platform's integration possibilities to allow for structures and components that contain either waveguide design where appropriate.

4.2.3.1 Tapered Waveguide Couplers

Figure 4.4a below gives schematic overview of a deeply etched adiabatic tapered transition region between a strongly confined waveguide bend and a weekly confined straight waveguide section, while Figure 4.4b gives a scanning electron microscope image of a fabricated version of this design.

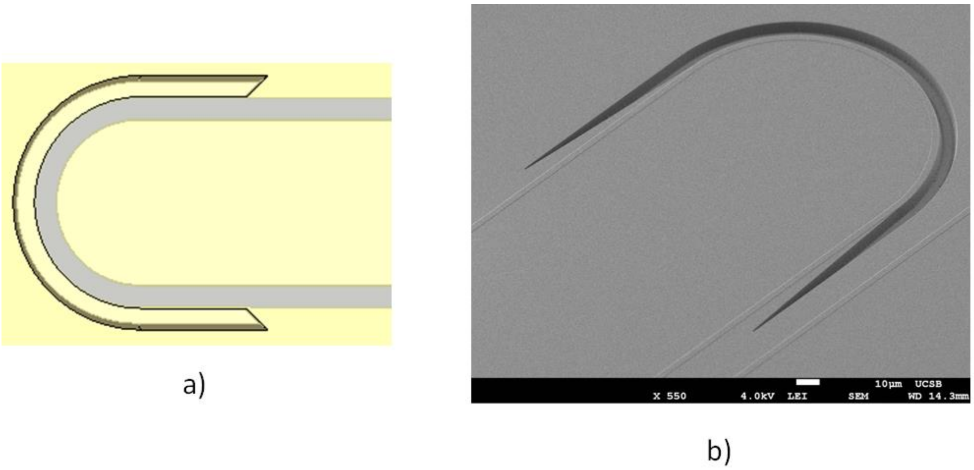

Figure 4.4: *(a) Schematic illustration of a weekly guiding* Si_3N_4*-core/*SiO_2*-clad waveguide featuring a tapered transition into a deeply etched strongly guiding bent waveguide. (b) SEM image of a fabricated version of this design. This fabrication split does not feature the straight region of the transition section.*

When designing such tapered transition regions, a fundamental engineering trade-off exists between complete adiabaticity and excess scattering loss. Here the component designer is pulled in two opposite directions: increase the tapered section length to provide as gradual, and thus as efficient, transition between waveguide types as possible, while at the same time keeping the excess scattering loss, which is directly proportional to component length, associated with such a structure to minimum. Inevitably an optimum point will exist based upon the fabrication process parameters. Besides the taper length, the other important parameter of interest when designing such structures is the width or ‘pointiness’ of the taper tip. To ensure efficient mode coupling, low reflection, and low scattering loss between waveguide sections, the taper tip region should be as narrow as the fabrication process will allow.

4.2.3.2 Finite Difference Time Doman (FDTD) Design

To quantify the transition efficiency and bend loss performance of a series of adiabatic tapered transitions and deeply etched strongly guiding bent waveguides, a sequence of finite difference time domain (FDTD) simulations using the Lumerical FDTD solutions software package were performed on structures similar to that shown in Figure 4.2 and Figure 4.4. Such a numerical analysis technique, while computationally intensive, allows for the quantification of both the transmission and reflection profiles of the structure under investigation. An example calculation is shown in Figure 4.5.

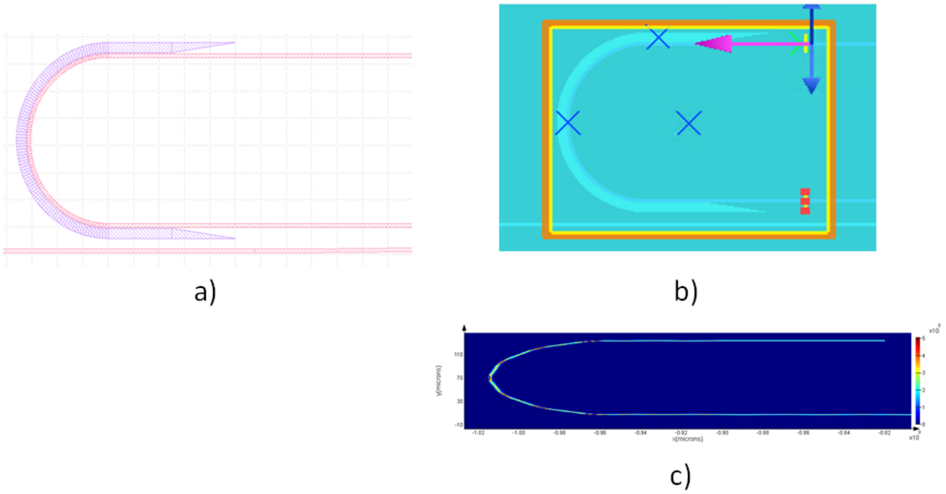
a)

b)

c)

Figure 4.5: *(a) Lithography mask layout snapshot of a strongly guiding deeply etched waveguide bend structure with adiabatic tapered mode converters. The pink structures are a shallowly etched* Si_3N_4 *core material, while the purple features are the deeply etched* SiO_2 *cladding regions. Here the bend radius is 62.5 µm, the waveguide width is 2.8 µm, the deep etch width is 7.5 µm, and the taper transition regions are 100 µm long straight sections*

followed by 100 μm long adiabatic sections. (b) Lumerical FDTD simulation screen capture showing the implementation of the structure described in (a). The mode field monitors and simulation region boundaries are shown as blue x's and orange lines, respectively. (c) Resulting calculated optical field profile of the structure. The entire transmission through both tapers and the 62.5 μm bend radius waveguide features a loss less than 0.2 dB (>97% transmission efficiency). As was shown in Figure 4.3, the calculated bend loss for this structure is below 0.01 dB/m for all radii from 62.5 μm to 5 mm.

4.3 Waveguide Sidewall Bragg Grating Filters

Bragg grating structures are an integral part of the diverse array of components that comprise modern optical systems. These include distributed tunable Bragg reflector (DBR) lasers, distributed feedback (DFB) lasers, dispersion compensators, and wavelength-division multiplexed (WDM) channel filters. With the current push towards coherent transmission and detection schemes, stable and extremely narrow linewidth lasers have become increasingly more important. A low loss grating capable of providing high reflectivity, while at the same time maintaining an extremely selective passband, is necessary to realize a new generation of coherent optical devices. Furthermore, low loss is critical in the scaling of large area photonic integrated circuits with stringent power requirements.

There have been prior results reported on sidewall grating technologies that include patterning through reactive-ion etching [17] and direct-write spatial-phase-locked electron beam lithography [18]. Prominent results in these approaches have bandwidths on the order of 0.12 nm with coupling constant values of roughly 4.5 cm^{-1} [19]. The limitations to these approaches include their reliance on strict etch tolerances, as well as their requirements for multiple lithographic patterning and etch steps [18][19]. The limitations of prior approaches are primarily due to a combination of both design constraints and fabrication technology.

This section covers the design of a collection of sidewall gratings in ultra-low-loss Si_3N_4 planar waveguides. Through a precise design approach that leverages lithographically defined waveguide geometry, the presented sidewall gratings can achieve a wide range of coupling constants, including the very low values required for an exceptionally narrow passband. Just as well, since the gratings are all defined in a single lithographic step, multiple types of gratings can follow one another along the same waveguide section. This creates an opportunity for integrated circuits with complex filter functions. The requirement of only a single lithography step means that such structures are ideal candidates for integration within the ULL waveguide platform.

4.3.1 Coupled Mode Theory

To analyze the behavior of such structures we turn to a coupled-mode approach. Here we express the solution to the more complex grating geometry in terms of the original basis set of eigenmodes of the simpler straight waveguide structure. We can simplify the forthcoming analysis by first defining a set of normalized parameters [20]. We begin by defining a detuning parameter,

$$\boldsymbol{\delta = \beta - \beta_o = \frac{\omega - \omega_o}{\omega_o} \cdot \frac{\pi}{\Lambda} \cdot \frac{\bar{n}(\lambda)}{\bar{n}_{Bragg}}} \tag{4.1}$$

where, β is the propagation constant of the waveguide, β_o is the propagation constant at the Bragg frequency ω_o (or equivalently the Bragg wavelength λ_o), $\bar{n}_{Bragg}$ is the effective index of the material specifically at the Bragg wavelength, and $\bar{n}(\lambda)$ is the effective index of the material over all wavelengths. The Bragg period of the structure, Λ, is given by

$$\boldsymbol{\Lambda} = \frac{\boldsymbol{\lambda_o}}{\mathbf{2\bar{n}}} \tag{4.2}$$

For waveguides containing gain or loss, β is complex, meaning that so too is the detuning parameter. It is now convenient to define a decay constant, σ, such as

$$\boldsymbol{\sigma^2 = \tilde{\kappa}^2 - \tilde{\delta}^2} \tag{4.3}$$

where the tildes are added to explicitly indicate that the coupling constant, κ, detuning parameter, δ, and decay constant, σ, can be complex. Through Equations 4.1 and 4.3 we can solve for the field reflectivity spectrum of the grating

$$\boldsymbol{\tilde{r}_g = -j\frac{\tilde{\kappa}\tanh(\tilde{\sigma}L_g)}{\tilde{\sigma}+j\tilde{\delta}\tanh(\tilde{\sigma}L_g)}} \tag{4.4}$$

where Lg is the grating length. The power reflection spectrum is given by the absolute square of Equation 4.4. With Equations 4.1 and 4.4 in mind, as well as the condition that power is only input into one side of the structure, the coupling constant of the grating can be approximated as one half of the reflection bandwidth. This is illustrated in Figure 4.6.

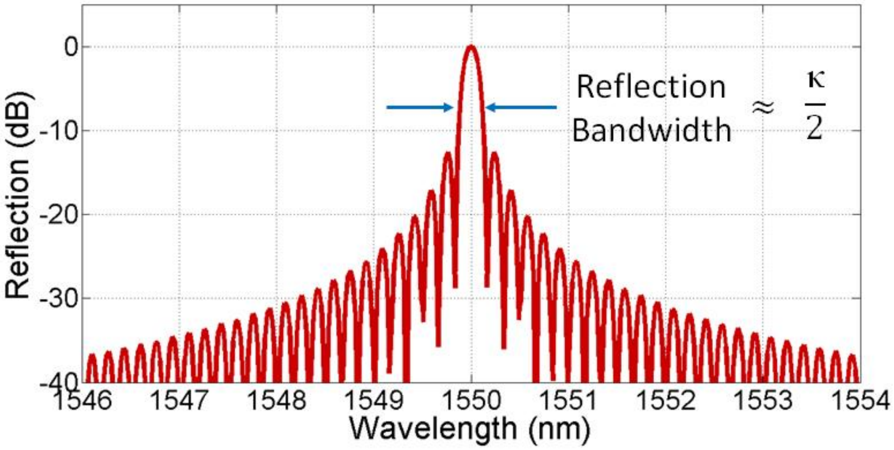

Figure 4.6: *Power reflection spectrum of a grating given by the absolute square of Equation 4.4. The curve has the expected sin x/x spectrum with the development of a well-defined transmission stopband (or reflection bandwidth) characterized by κ/2.*

A wide range of coupling constant values, and hence grating bandwidths, can be achieved through proper grating design.

4.3.2 Transfer-Matrix Modeling

Transfer, scattering, or fundamental (T-,S-, or F-) matrix formalism as a concept is widely known as a design methodology that reduces the wavelength dependent reflection and transmission analysis of axial structures with numerous impedance discontinuities to a mathematical exercise in matrix multiplication [21][22]. Such impedance discontinuities that can be modeled with this technique are as simple as interfaces between an optical waveguide and the chip facet onto which it impinges, or as complex as the entirety of a distributed phase shift distributed feedback laser cavity in which the coupling constant of the grating varies spatially along the direction of optical propagation [24].

To begin, the general form of a scattering matrix is given below [25]:

$$\begin{bmatrix} a_-(0) \\ a_+(z) \end{bmatrix} = \begin{bmatrix} S_{11} & S_{12} \\ S_{21} & S_{22} \end{bmatrix} \begin{bmatrix} a_+(0) \\ a_-(z) \end{bmatrix} \tag{4.5}$$

where the quantities a± are length-N vectors, and S_{ij} are N × N matrices. With some algebraic manipulation, it is possible to relate the elements of the scattering matrix to the elements of the corresponding transfer matrix:

$$\begin{bmatrix} S_{11} & S_{12} \\ S_{21} & S_{22} \end{bmatrix} = \begin{bmatrix} -T_{22}^{-1}T_{21} & T_{22}^{-1} \\ (T_{11} - T_{12}T_{22}^{-1}T_{21}) & T_{12}T_{22}^{-1} \end{bmatrix} \tag{4.6}$$

Similarly, it is possible to write the transfer matrix elements in terms of the scattering matrix elements:

$$\begin{bmatrix} T_{11} & T_{12} \\ T_{21} & T_{22} \end{bmatrix} = \begin{bmatrix} S_{21} - S_{22}S_{12}^{-1}S_{11} & S_{22}S_{12}^{-1} \\ -S_{12}^{-1}S_{11} & S_{12}^{-1} \end{bmatrix} \tag{4.7}$$

Because the scattering matrix describes the outputs in terms of the inputs, one might ask why transfer matrices are used at all. The benefit of the transfer matrix is that arbitrary structures can be analyzed by simply multiplying the transfer matrices of each segment. Scattering matrices cannot be cascaded in this manner.

For structures which do not have any optical gain or loss, there are additional constraints placed on the transfer matrix and scattering matrix by the requirements of power conservation and time reversal symmetry. Power conservation simply means that the net amount of power flowing into the device must be 0. Time reversal symmetry means that for every valid solution to Maxwell’s equations, another solution may be obtained by replacing t by −t, β by −β, E by E^* and H by $-H^*$, where * denotes a complex conjugate. For scattering matrices, this means that:

$$S = S^T \tag{4.8}$$

and for transfer matrices:

$$T_{22} = T_{11}^* \; and \; T_{21} = T_{12}^* \tag{4.9}$$

Therefore, only two elements of the transfer matrix are needed to completely describe a lossless system. For a uniform waveguide section without loss and propagation constant β, the transfer matrix is:

$$T = \begin{bmatrix} e^{-j\beta z} & 0 \\ 0 & e^{+j\beta z} \end{bmatrix} \tag{4.10}$$

In equation 4.10, forward traveling waves propagate with wavevector β and backward traveling waves propagate with wavevector −β. If the waveguide has loss or gain, the appropriate transfer matrix is:

$$T = \begin{bmatrix} e^{-(\alpha+j\beta)z} & 0 \\ 0 & e^{+(\alpha+j\beta)z} \end{bmatrix} \tag{4.11}$$

where positive values of α correspond to loss and negative values correspond to gain. To calculate the reflection and transmission from a singular dielectric interface, the effect can be modeled using the simple Fresnel reflection equations so long as the electromagnetic modes are reasonably well matched on both sides of the discontinuity. The transfer matrix describing Fresnel reflection at a dielectric interface between two materials with indices n_1 and n_2 is:

$$T = \frac{1}{2\sqrt{n_1 n_2}} \begin{bmatrix} n_1 + n_2 & n_2 - n_1 \\ n_2 - n_1 & n_1 + n_2 \end{bmatrix} \tag{4.12}$$

This transfer matrix relates the mode amplitudes immediately to the adjoining sides of the interface. More generally, the transfer matrix for a partially reflecting surface can be always be cast in the following form:

$$T = \frac{j}{\sqrt{1-r^2}}\begin{bmatrix} 1 & r \\ r & 1 \end{bmatrix} \tag{4.13}$$

where r is a real number representing the amplitude reflection coefficient. Cascading equations 4.11 and 4.12 allows for the mathematical representation of a Bragg grating structure. For a standard linear Bragg grating (as is shown in Figure 4.7) of length L and grating strength κ the transfer matrix takes the form:

$$T = \begin{bmatrix} \cosh(\sigma L) - j\frac{\delta}{\sigma}\sinh(\sigma L) & \frac{\kappa}{\sigma}\sinh(\sigma L) \\ \frac{\kappa^*}{\sigma}\sinh(\sigma L) & \cosh(\sigma L) + j\frac{\delta}{\sigma}\sinh(\sigma L) \end{bmatrix} \tag{4.14}$$

where the parameters δ is given by:

$$\delta = \beta - \frac{\pi}{\lambda} \tag{4.15}$$

in which β is the waveguide propagation constant, Λ is the Bragg period of the structure given in Equation 4.2, λ is the wavelength of interest, and σ is defined in Equation 4.3.

As was shown, the transfer matrix formalism is still valid for complex propagation constants. This means that threshold gain and lasing wavelengths of active laser structures can also be numerically calculated. Further examples of this technique on a variety of integrated waveguide devices, such as Michelson interferometers with mismatched arms, is given in [25]. Appendix 2 includes the full MATLAB code block used to design the waveguide sidewall grating structures presented in this thesis.

4.3.3 Reflector Design

With coupled mode theory and transfer matrix modeling approaches in mind, a design framework now exists to characterize the interaction between the coupled forward-traveling and backward-traveling modes of such waveguide-based devices.

4.3.3.1 Resonator Mirrors and Filters

Figure 4.7 below gives a schematic representation of a standard linear Bragg grating implemented within the waveguide sidewall framework.

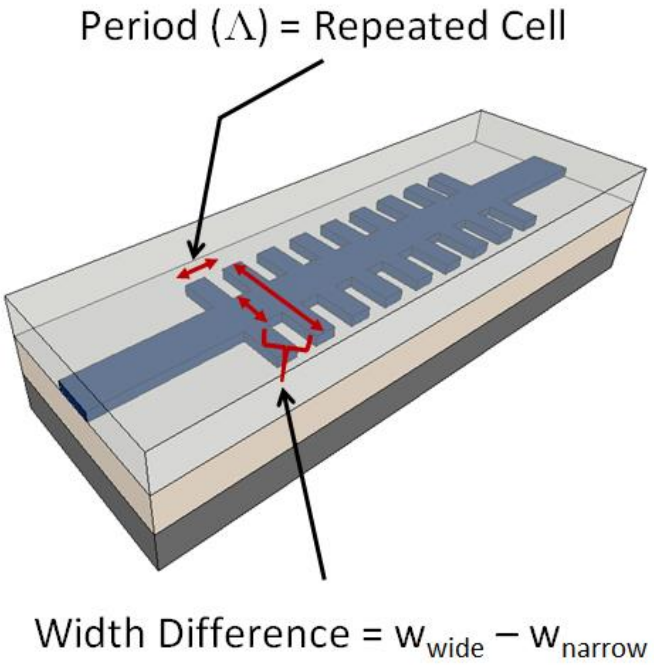

Figure 4.7: *Schematic representation of a linear Bragg grating structure with periodic width perturbations along the waveguide propagation length. The period of the structure is denoted as Λ.*

Here the Bragg period of the structure (Λ), or the total length of a single repeating cell of the structure, controls the Bragg frequency ω_o (or equivalently the Bragg wavelength λ_o). The width difference between the wide and narrow sections controls the grating modulation strength (κ). As a qualitative matter of intuition, a greater width difference between grating half-periods will induce a greater magnitude of reflection per unit length. Quantitative measurements describing the extent of the width difference's effect on measured κ values is shown later in Section 4.7 (Figure 4.26). Additionally, for equivalent length gratings, a larger coupling constant will yield a large grating bandwidth. Such design is readily amenable to high volume nanophotonics manufacturing, as the entirety of the structure's properties of interest are most heavily influenced at the lithography stage, rather than the etching stage, which traditionally imparts a higher degree fabrication process variability.

4.3.3.1.1 Apodization

Apodization, or "removing the foot", is an optical filtering technique that in the framework of fiber or waveguide gratings means to modulate the grating strength or coupling coefficient (κ) along the grating length [26]. This technique can be leveraged to significantly reduce the magnitude of undesired sidelobes that are commonly present in the grating reflectivity spectrum of such a linear design as presented in Figure 4.7. Figure 4.8 below gives a schematic representation of an apodized waveguide sidewall grating and an example coupling constant profile comparison between a linear (unapodized) and an apodized design.

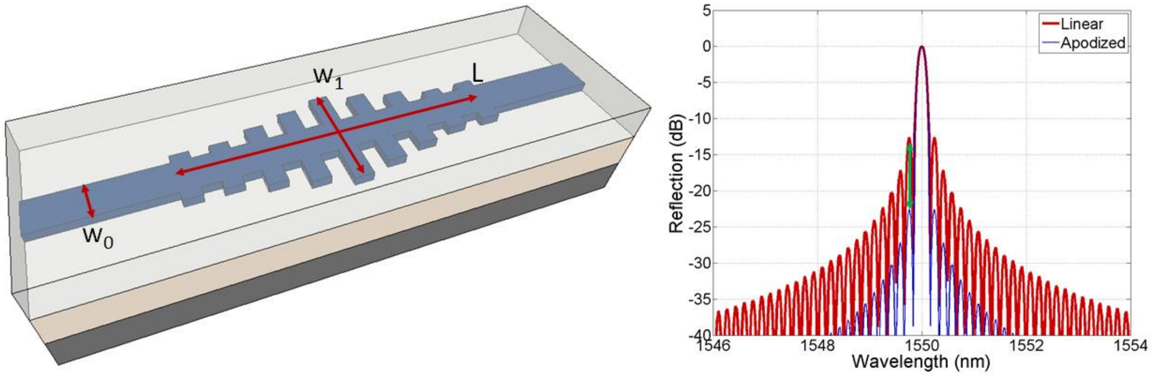

Figure 4.8: *(Left) Schematic representation of an apodized Bragg grating structure with modulated periodic width perturbations along the waveguide propagation length. The parameters from Equation 4.16 are labeled on the structure. (Right) Reflection profile comparison between a linear grating and an apodized grating. The apodization applied has successfully reduced the magnitude of the grating sidelobes as indicated by the green arrow. These profiles were generated through the T-matrix approach covered in Section 4.3.2.*

When determining which apodization profile is best, the intended final grating application should be kept at the forefront, as many such windowing functions exist (Gauss, Hamming, Tanh, and Blackman just to name a few) [26]. As an example, a Tanh windowing function gives a broad spectral response with a flat-topped passband (ideal for dispersion compensation), while a Blackman window function gives a narrow spectral response with a less than flat-passband (ideal for narrow linewidth optical filtering) [26]. For example, a Blackman window function within such a sidewall grating formalism would have the form [5]:

$$\boldsymbol{w(z) = w_0 + (w_1 - w_0)\times\frac{1+(1+B)cos(2\pi\frac{x-\frac{1}{2}L}{L}))+Bcos(4\pi(\frac{x-\frac{1}{2}L}{L}))}{2+2B}} \tag{4.16}$$

where w_0 is the nominal 2.8 μm waveguide width, w_1 is the target value of waveguide width difference, L is the total grating length, and B is the Blackman window parameter (held at 0.18). Finally, when applying an apodization profile to a grating, a successful reflector design must account for the possibility of reduction in peak reflectivity that is possible as compared to the linear case. As illustrated in Figure 4.8 (right), the apodized design featuring the Tanh window function will have a lower total peak reflectivity than the linear design. This can be accounted for by increasing the coupling constant for the Tanh design at its central length value to compensate.

4.4 Bus-Coupled Racetrack Ring Resonators

As an alternative to Bragg grating structures as optical feedback elements, an on-chip integrated resonator design can be formed by wrapping a waveguide back onto itself to create a racetrack ring resonator. Another bus waveguide is brought into close proximity of the straight section of the racetrack resonator to form a directional coupler, which allows for a tailored coupling of light into and out of the structure. Compared to grating-based resonator structures, this design offers a simple and straightforward implementation. A schematic of such a design is shown in Figure 4.9.

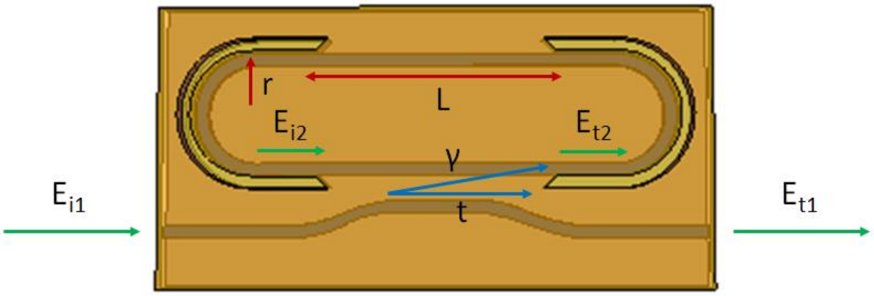

Figure 4.9: *Layout of the racetrack ring resonator. The design integrates together each of the main waveguide components described in Section 4.2. The parameters shown with red arrows are the ring racetrack length (L), and the ring radius (r). The parameters shown with green and blue arrows are described in Equation 4.17.*

In this structure, the waveguides are all nominally 2.8 μm wide to ensure single mode operation, and the coupling gap between the racetrack and the bus waveguide is 1 μm to allow for fabrication simplicity. The deeply etched strongly guiding waveguide bends have etched sections that are 7.5 μm wide, and the S-bend waveguides on either side of the central straight coupling region allow the bus waveguide to have 7.5 μm of offset from the deeply etched bend tapers.

4.4.1 Single Bus Ring Resonators

The implemented configuration of a single bus ring resonator is shown in Figure 4.9. To theoretically describe such a structure, the approach given in [27] is taken. Defining that a single unidirectional mode of the resonator is excited, the coupling is lossless, a single polarization is considered, and the various kinds of losses occurring along the propagation of light in the ring resonator are incorporated into the attenuation constant, the interaction can be described by the matrix relation:

$$\begin{bmatrix} \boldsymbol{E_{t1}} \\ \boldsymbol{E_{t2}} \end{bmatrix} = \begin{bmatrix} \boldsymbol{t} & \boldsymbol{\gamma} \\ -\boldsymbol{\gamma^*} & \boldsymbol{t^*} \end{bmatrix} \begin{bmatrix} \boldsymbol{E_{i1}} \\ \boldsymbol{E_{i2}} \end{bmatrix} \tag{4.17}$$

The complex mode amplitudes E are normalized, so that their squared magnitude corresponds to the modal power. The coupler parameters t and γ depend on the specific coupling mechanism used. The $*$ denotes the conjugated complex value of t and γ, respectively. The network under consideration is reciprocal, so the matrix is symmetric. Therefore:

$$\left|\boldsymbol{t^2}\right| + \left|\boldsymbol{\gamma^2}\right| = \boldsymbol{1} \tag{4.18}$$

To further simplify the model, E_{i1} is chosen to be equal to 1. Then, the round trip in the ring is given by:

$$\boldsymbol{E_{i2} = \alpha e^{j\theta} E_{t2}} \tag{4.19}$$

where α is the loss coefficient of the ring (zero loss: $\alpha = 1$) and $\theta = 2\pi n_{eff}C/\lambda$. Here n_{eff} is the effective index of the mode within the ring structure, C is the circumference of the ring resonator (including the distance traveled in the racetrack sections), and λ is the wavelength of interest. From Equations 4.17 and 4.19 the solutions for the fields within the structure are:

$$\boldsymbol{E_{t1} = \frac{-\alpha + te^{-j\theta}}{-\alpha t^* + e^{-j\theta}}} \tag{4.20}$$

$$\boldsymbol{E_{i2} = \frac{-\alpha\gamma^*}{-\alpha t^* + e^{-j\theta}}} \tag{4.20}$$

$$\boldsymbol{E_{t2} = \frac{-\gamma^*}{1 - \alpha t^* e^{j\theta}}} \tag{4.20}$$

This leads to the transmitted power P_{t1} of the output waveguide as:

$$\boldsymbol{P_{t1} = |E_{t1}|^2 = \frac{\alpha^2 + |t|^2 - 2\alpha|t|cos(\theta + \phi_t)}{1 + \alpha^2|t|^2 - 2\alpha|t|cos(\theta + \phi_t)}} \tag{4.21}$$

and the circulating power P_{i2} in the ring as:

$$P_{i2} = |E_{i2}|^2 = \frac{\alpha^2(1-|t|^2)}{1+\alpha^2|t|^2-2\alpha|t|cos(\theta+\phi_t)} \tag{4.22}$$

where t = |t|exp(jϕ_t), with |t| representing the coupling losses and ϕ_t the phase of the coupler. An example of the wavelength depended filter characteristic for such a ring resonator configuration is shown in Figure 4.10.

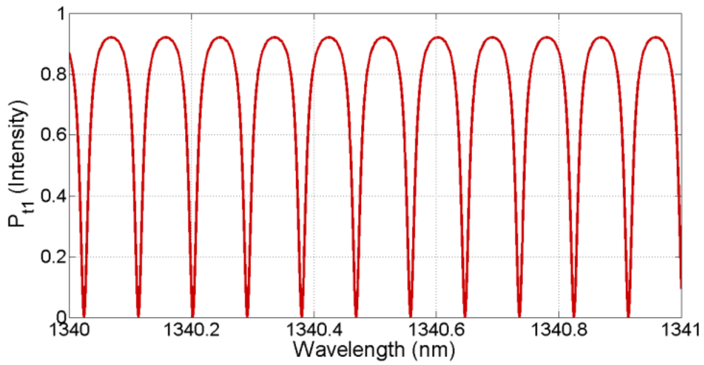

Figure 4.10 *Power transmission spectrum through a single bus coupled ring resonator using Equation 4.21. The curve has the expected Fabry-Pérot like spectrum with the notch type filter characteristic.*

4.4.2 Coupling Region Analysis and Design

As is shown in Figure 4.9, the coupling region includes two weakly bent, but lengthy, waveguide S-bends on either side of the straight central region. These S-bends will introduce significant coupling between the bus waveguide and the racetrack ring cavity, so a coupled mode theory approach, which is widely used throughout the literature for straight bus coupled waveguides, will not be taken here. Instead, the design of the coupling region follows the same finite difference time domain (FDTD) approach as that done for the tapered waveguide couplers in Section 4.3. Figure 4.11 shows the results of a series of Lumerical FDTD solutions software package calculations of the structure given in Figure 4.9.

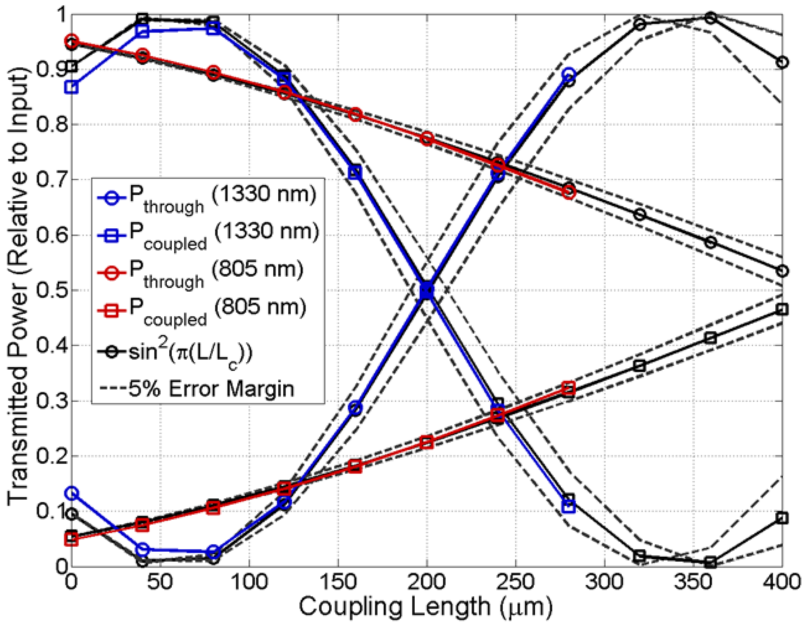

Figure 4.11: *FDTD simulation results for the structure shown in Figure 4.9. The transmitted power through the bus waveguide (T) relative to the input power is given vs. length of the straight coupling section. Included for additional qualitative understanding is the results of a standard coupled mode theory approach [23]. Due to the weakly bent S-bends on either side of the central straight coupling region, the coupled mode result must include an extra 175 μm of length in addition to the central region's length to match with the FDTD results. The included error margins highlight that as coupling length increases any deviations from the nominal design, for instance through fabrication non-idealities, will cause an increased amount of coupling deviation in the transmitted power value.*

The simulation was done over two distinct wavelength ranges, 1330 nm and 808 nm, which correspond to the respective favored luminescence and pump wavelengths of the neodymium dopant atom, as will be discussed in Chapter 5.

4.5 Si_3N_4 and Ta_2O_5 Passive Waveguide Component Fabrication Overview

Figure 4.12 gives a graphical representation of the entirety of the Si_3N_4-core or Ta_2O_5-core waveguide fabrication process. Appendix 1 provides a ‘traveler’ that includes the in-house process steps that follow this diagram. Waveguide fabrication begins with either a 500 µm or a 1 mm thick 100 mm diameter silicon substrate upon which 15 microns of silica is thermally grown by wet oxidation for the lower cladding. Next, either the Si_3N_4 or Ta_2O_5 waveguide core is deposited by either low pressure chemical vapor deposition (LPCVD) in the case of Si_3N_4 or sputter deposition in the case of Ta_2O_5. This core layer is then patterned using a photoresist mask by 248 nm stepper lithography and an optimized $CH_3/CF_4/O_2$ inductively coupled plasma etch. The etching chamber had $CH_3/CF_4/O_2$ gas flows of 35/5/10 cm^3/min, a pressure of 0.5 Pa, an RF source power of 500 W, and an RF bias of 50 W. The same etching protocol is employed for both the Si_3N_4 and Ta_2O_5 waveguide core materials. It is this lithography and etching step that will define the waveguide sidewall Bragg grating features if they exist. This step will be covered in more detail in Section 4.5.1.

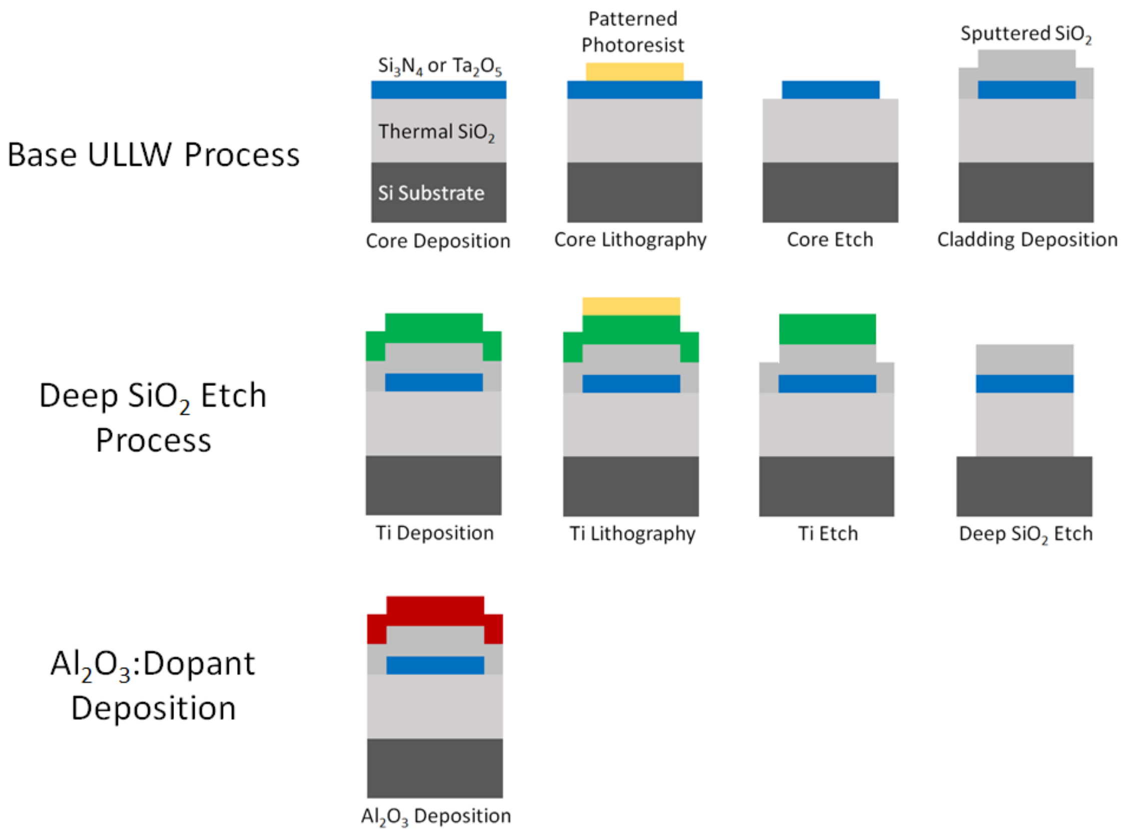

Figure 4.12: *Schematic overview of the fabrication process for each of the waveguide types discussed within this thesis. All of the processes employed within the base ultra-low loss waveguide platform process (including the deposition and etch steps of the* Si_3N_4 *and* Ta_2O_5 *materials) are CMOS compatible.*

Figure 4.13(a-c) show atomic force microscopy (AFM) measurements of a Ta_2O_5 waveguide core top and sidewalls and an optical micrograph of the bus and outermost waveguides of a 10 m long Archimedean spiral. The sidewall roughness of the etching step, a critical factor in achieving low propagation loss, in this case had R_a and R_q (average and RMS) values of 2.4 and 3.0 nm. The measured sidewall angle was 80°. The resulting surface roughness of the deposited Ta_2O_5 core after etching had R_a and R_q values of 0.31 and 0.21 nm. These roughness values, as well as the sidewall angle, are similar to within 10% of what is nominally measured for Si_3N_4-core based waveguides.

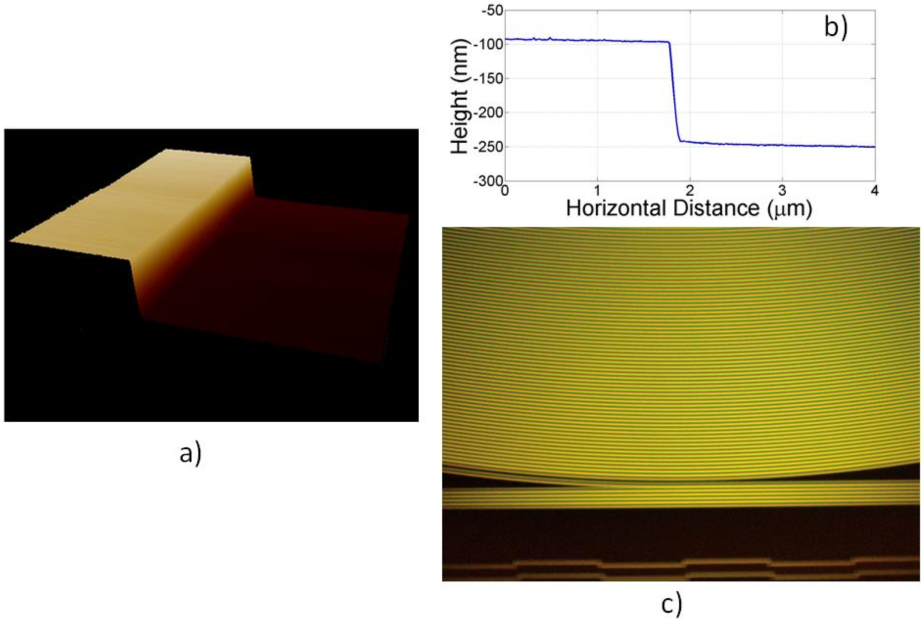

Figure 4.13: *(a) Three-dimensional AFM image of the $CH_3/CF_4/O_2$ ICP etch of a Ta_2O_5 core. (b) Lateral AFM data quantifying the depth of etch. The deposited core was 90 nm thick but over-etched into the lower thermal SiO_2 cladding for a total etch depth of 150 nm. (c) Dark field optical micrograph of the bus and outermost waveguides (yellow in color) of a 10 m long Archimedean spiral.*

The patterning and etch steps are followed by a blanket sputter deposition of the upper SiO_2 cladding. At this stage in the fabrication, the wafer will undergo an anneal protocol, with the temperature and time duration depending upon the core material used. This allows for maximum reduction in hydrogen impurity related absorption loss. For a Si_3N_4-core waveguide the anneal will be 7 hours long at 1050 ^{o}C in 3.0 SLPM N_2 atmosphere. For a Ta_2O_5-core waveguide the anneal will be 3 hours long at 300 ^{o}C in 3.0 SLPM N_2 atmosphere. The Ta_2O_5 material has a limited maximum attainable anneal temperature here, as Ta_2O_5 crystallizes and catastrophically increases in loss above 650 °C for anneals longer than 3 hours [28]. Following annealing, if deeply etched strongly guiding bend features are required the wafer will undergo a deep SiO_2 etching protocol that features a titanium (Ti) hard-mask process. This process is covered in detail in Section 4.5.2. If a rare-earth-ion dopant layer is required, the Al_2O_3 host material and the requisite dopant will next be deposited by a reactive co-sputtering process [29]. An illustration of this process is shown in Figure 4.14.

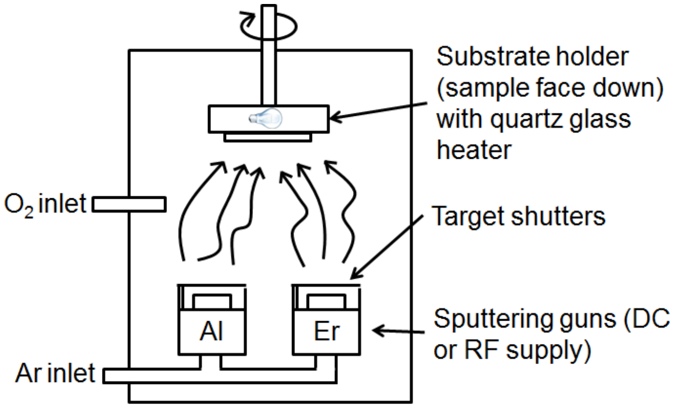

Figure 4.14: *Sputter deposition system overview. In this example, an* $Al_2O_3:Er^{3+}$ *film would be deposited, as an erbium sputtering target is placed within the chamber alongside the aluminum target.*

It is the ratio of RF powers applied to the targets that will eventually control the rare-earth-ion-dopant concentration within the final deposited Al_2O_3 host film. For samples with dopant concentrations in the 0.5-2 x 10^{20} cm^{-3} range, the Al power should be 200 W RF and the dopant power should be in the 14-22 W RF range. Any lower values than 12 W RF will cause the sputter system to lose plasma ignition and fail to carry on with a deposition. Finally, the wafer is diced into separate die and a mechanical polishing process conditions the device facets. This process is essential to ensure maximum fiber-to-chip coupling efficiency and waveguide-to-waveguide uniformity. An illustrative example is shown in Figure 4.15.

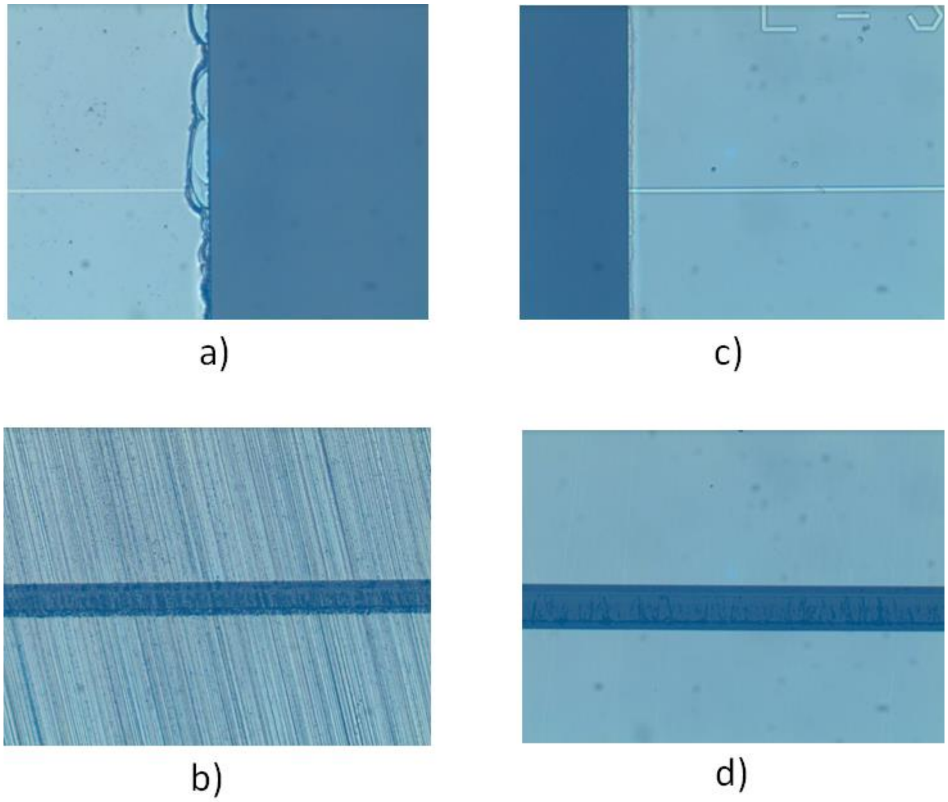

Figure 4.15: *(a-b) Top-down and side-on views of a fabricated waveguide die immediately following the dicing step. The deposited layers have delaminated significantly from the substrate, such that waveguide-to-fiber coupling would be impossible. (c-d) Top-down and side-on views after the mechanical facet polishing process has taken place. The delamination has been polished back so that only a smooth coupling surface remains. A 'dummy' Si cover sample is used to protect the top surface of the chip when polishing and is visible in (b) and (d).*

4.5.1 Sidewall Bragg Grating Lithography Optimization

With the entirety of the design of the waveguide sidewall Bragg gratings depending upon their lithographic resolution, care must be taken during this step to optimize for best performance. Figure 4.16 gives an example of common issues found when fabricating such devices.

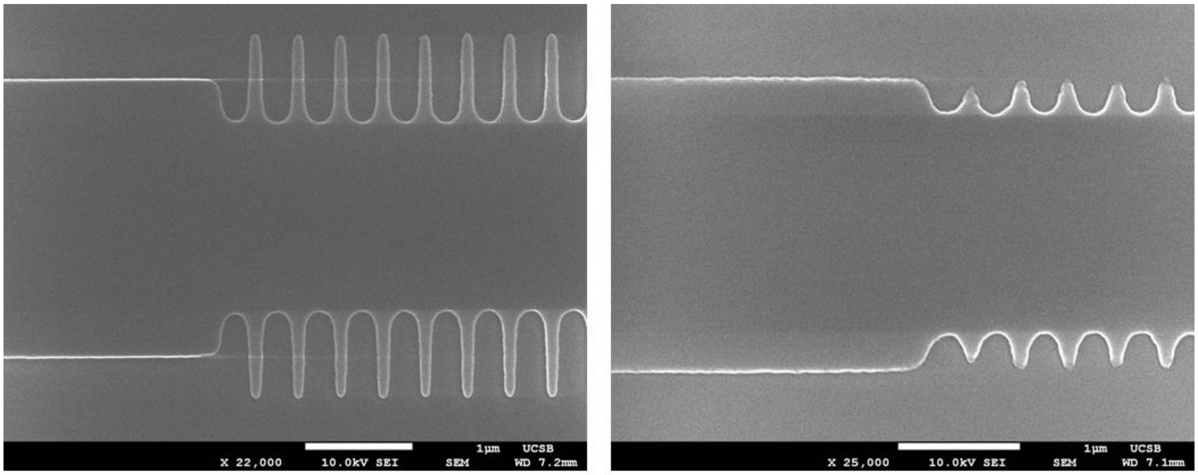

a) b)

Figure 4.16: *SEM image of an 80 nm etched Si_3N_4 core with a transition between a straight waveguide and a waveguide sidewall Bragg grating. In (a) the applied energy 'dose' of the 248 nm stepper system was too high, with the resulting overexposure causing rounding of the otherwise straight grating 'teeth'. In (b) the focus of the system was unoptimized beforehand, causing the teeth sections to be completely unresolved.*

During the lithographic exposure, both the 'dose' of the 248 nm light and the 'focus' on the sample by the system are independently controlled. Due to the small feature size of the grating 'teeth' the designs are particularly susceptible to errors when the system is out of focus. Proper calibration must be done beforehand to ensure a successful resolution of the design patterns. [30] gives an alternative technique for fabricating such sidewall gratings that allows for a greater amount of process control.

4.5.2 Deep SiO_2 Etch Optimization

To fabricate the strongly guiding waveguide structures detailed in Section 4.2, a deep SiO_2 etching protocol is required to ensure high confinement of the propagating optical mode. In this case ‘deep’ refers to any etch greater than 5 μm in depth. For such a structural requirement, two separate fabrication approaches exist: 1) Deeply etch the Si substrate then follow up with an oxidation step as in [31], or 2) deeply etch an existing SiO_2 layer. Due to the large thickness (6-15 μm) of lower SiO_2 cladding required in the ULL waveguide platform, along with the required geometry of the deeply etched tapered mode converters, approach 2) was undertaken. Throughout the literature chromium (Cr) has become a standard hard-mask material for such challenging deep etches. The drawback to Cr as a hard-mask material is that during etching it possesses an extreme loading effect, or to put differently, an etch rate that is extremely dependent upon the exposed area of the Cr. For this reason, titanium (Ti) was used instead as the hard-mask material, as a titanium deep etch (TIDE) process exists that features minimal loading effects [32].

When optimizing the process to achieve the best etched Ti sidewall profile, the Ti mask layer should be deposited through an RF sputter deposition, rather than E-beam deposition as is common for the material. Figure 4.17 illustrates the difference in etch profile that results depending upon the Ti deposition method.

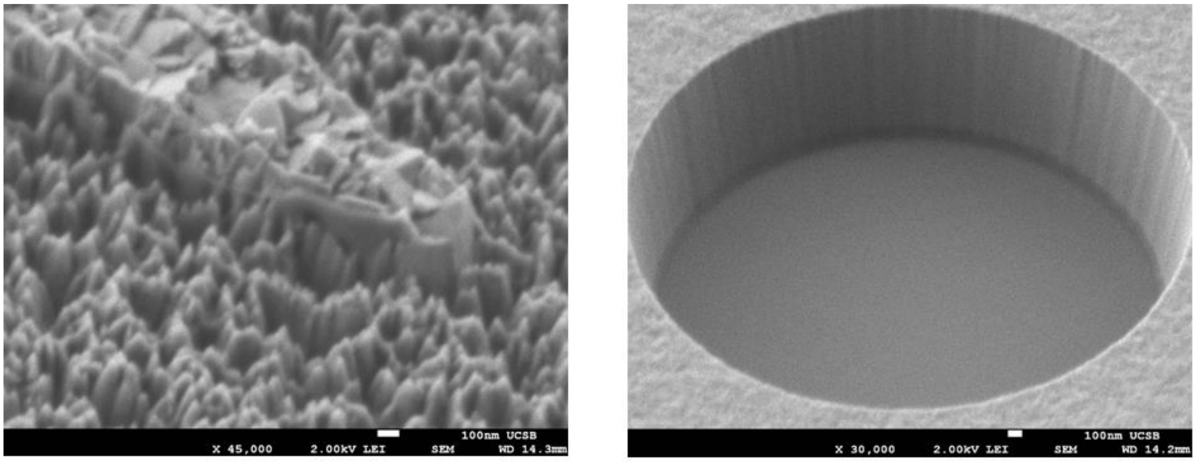

a) b)

Figure 4.17: *(a) SEM image of an E-beam deposited Ti taper feature etched through the TIDE process. (b) SEM image of an RF sputter deposited Ti hole feature etched through the TIDE process. While both features were etched for equivalent times, the resulting etch depths were widely disparate with (a) having an etch depth of less than 100 nm and (b) having an etch depth of 1.1 μm (the entirety of the film thickness). The large grain size of the E-beam deposited Ti drastically slows down the etch rate of the TIDE process.*

As can be plainly seen, the smaller grain size of the RF deposition method compared to the E-beam deposition method results in a superior etch profile. Figure 4.18 gives a collection of 6 μm deeply etched SiO_2 features that featured an RF sputtered Ti mask. The thickness of the Ti mask in this case was 1.1 μm.

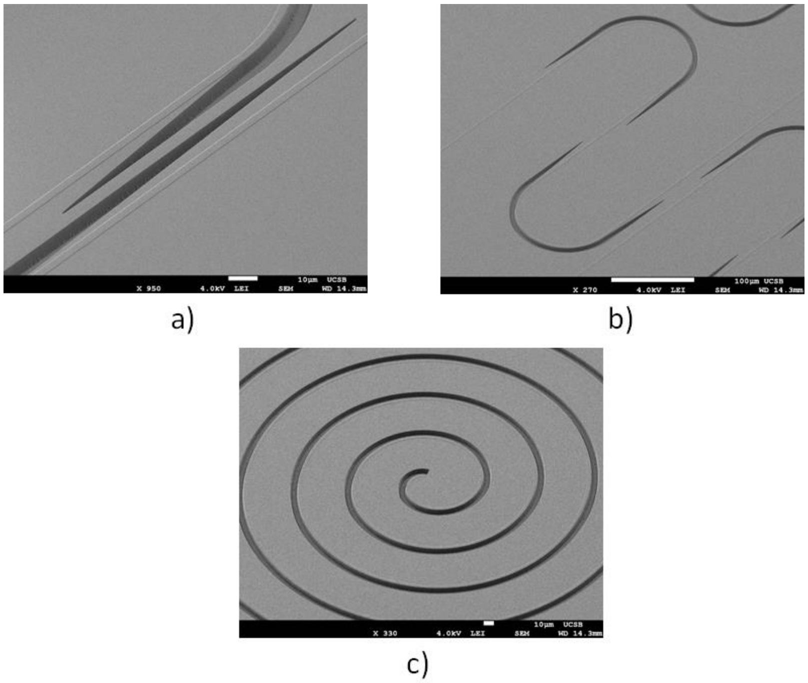

a) b)

c)

Figure 4.18: *6 μm deeply etched* SiO_2 *(a-b) adiabatic tapered mode converters and (c) spiral delay line.*

4.6 Optical Propagation Loss Characterization

4.6.1 Optical Backscattering Reflectometry

To quantify the propagation loss of the Ta_2O_5 waveguides we utilize the coherent optical frequency domain reflectometry (OFDR) technique using a commercially available system (Luna Inc. OBR 4400) [1][14][15]. In the OFDR technique a continuous wave laser source is scanned over several tens of nm in wavelength (1535-1600 nm in the C-band case, 1290-1330 nm in the O-band case), giving micron-level spatial resolution of the waveguide delay. It is important to note that the OFDR propagation loss measurement is independent of the excess loss and loss uncertainty incurred during fiber-to-chip coupling and is thus more accurate for very low losses than the commonly used cut-back technique. Additionally, over long length spans OFDR provides optical attenuation versus propagation distance that captures the loss variability caused by localized variations within the fabrication process. This loss variability can be attributed to imperfections, including those due to failed lithography sections of the waveguide core, or to flaws such as micron-sized clusters within the nominally homogenous sputter deposited upper SiO_2 cladding.

4.6.2 Characterization Results

4.6.2.1 Weekly Guiding Buried Ridge Waveguides

To test the optical loss of the 90 nm core Ta_2O_5 waveguides, 10 m long Archimedean spiral delays with an innermost minimum bend radius of 2 mm and 0.7 m long spiral delays consisting of Bézier curves having a minimum bend radius of 760 μm and a central loop mirror structure were designed and fabricated using the approach outline above in Section 4.5. Figure 4.19 below gives a schematic representation of both structures.

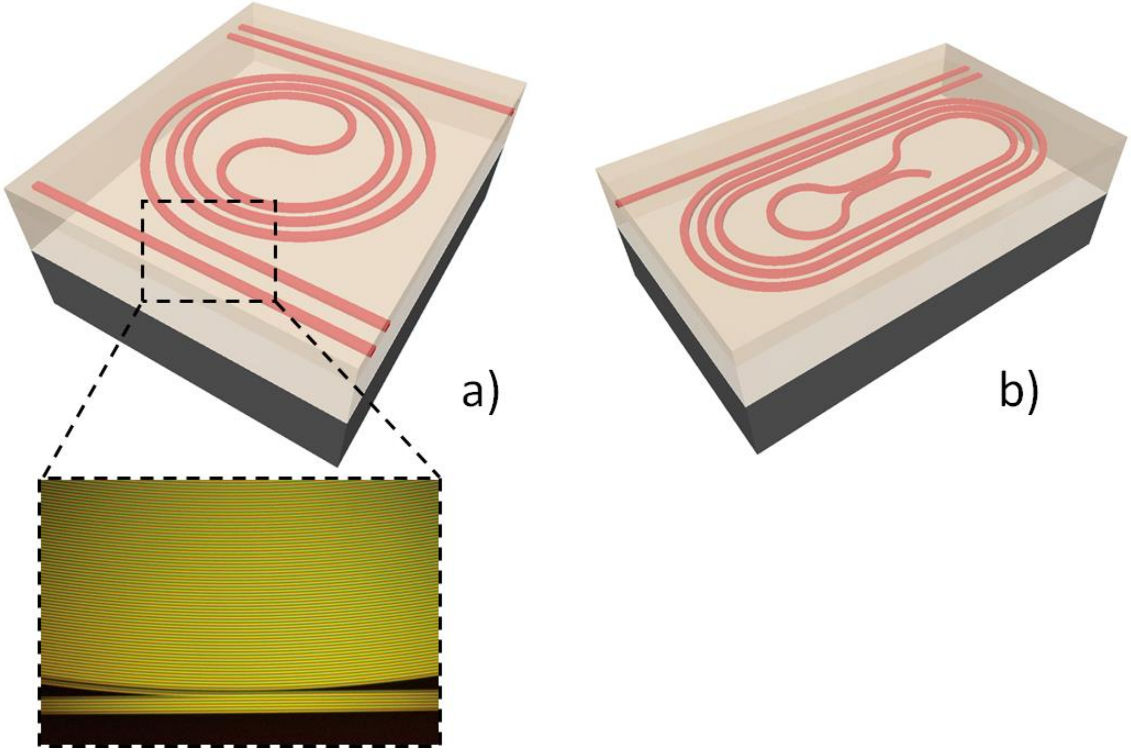

Figure 4.19: *(a) Schematic representation of a fabricated die featuring the 10 m long Archimedean spiral with 2 mm minimum bend radius (at the innermost turn-around section). The outermost bend radius was 10 mm. The inset shows a dark field optical micrograph of the bus and outermost waveguides (yellow in color) of the fabricated 10 m long Archimedean spiral. (b) Schematic representation of a fabricated die containing the 0.7 m long spiral delay with Bézier curves connecting the straight sections. The minimum bend radius of the Bézier curves was 760 µm, while the outermost radius was 1.7 mm. The loop mirror structure can be seen within the spiral center. Both designs in (a) and (b) also feature straight waveguides as auxiliary test structures.*

Figure 4.20 shows reflection amplitude data measured for one of the 0.7 m long spiral delays consisting of Bézier curves having minimum bend radii of 760 µm and a central loop mirror structure. In this structure, the Ta_2O_5 core thickness was 90 nm, the nominal waveguide width was 2.8 μm, and the upper SiO_2 cladding thickness was 1.1 μm. Before the OBR scan, the fiber-to-chip coupling and launched polarization are optimized using the OBR source laser, a 3-paddle polarizer, and an infrared camera mounted on a microscope above the sample.

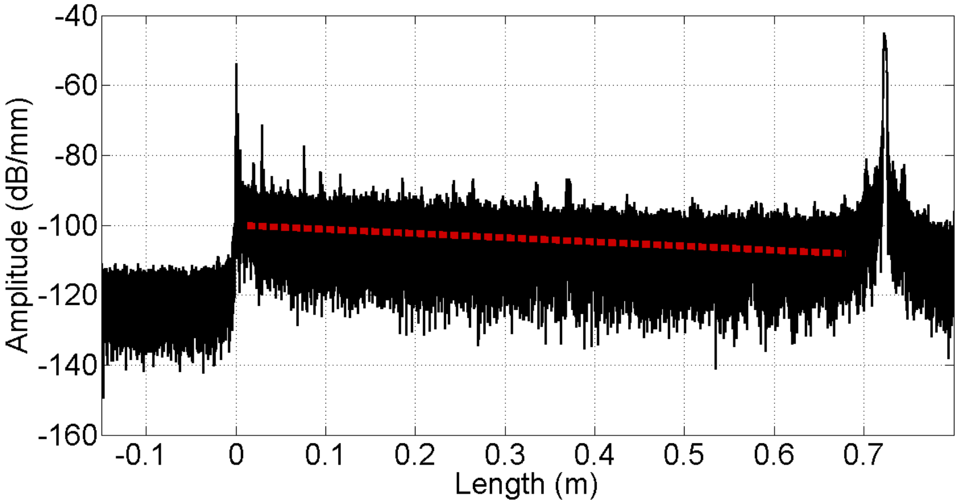

Figure 4.20: *Composite OBR wavelength scan across 1535-1600 nm for a 0.7 m long spiral delay. The inner-most portion of the delay contains a loop mirror reflector, which is clearly visible as a large reflection on the data trace. The other smaller reflection peaks throughout the propagation length are due to scattering events caused by various fabrication imperfections along the waveguide delay. The dashed red line gives a linear fit of the waveguide backscatter averaged over all measured wavelengths. The magnitude of the propagation loss can be approximated as one half of the slope of this line. Bend loss was not measurable compared to the propagation loss as experienced over the entirety of propagation through the spiral as evidenced by the constant slope of the measured backscattered power with respect to distance. Utilizing a series of straight waveguides on this same die we determined through transmission measurements that the fiber-to-chip coupling loss using cleaved SMF-28 fiber was 3 dB/facet.*

The left-most peak (near 0 m in distance) is the coupling interface between the fiber and the chip edge. The right peak (near 0.7 m in distance) is the reflection from the on-chip loop mirror structure. It is through this distance relationship that we measured the group index of the waveguide to be 1.55, which agrees with our optical mode simulations and is roughly comparable to that as measured in a Si_3N_4 core waveguide of a similar geometry [11]. Figure 4.21 shows the mean and standard deviation of the spectral dependence of the propagation loss within 3 separate die of 10 m long Archimedean spirals. As is shown, even the un-annealed samples display a lower loss across the C-band than the previously recorded lowest loss Ta_2O_5-core waveguide designs [16]. After annealing, the loss is even further reduced to lower than that demonstrated by a Si_3N_4 core waveguide of an equivalent geometry [11]. Due to various scattering events caused by the imperfect nature of the sputtered upper cladding above the entirety of the 10 m spiral, the annealed samples display an irregular standard deviation over the whole of the wavelength range. Such a yield issue is a remaining challenge of fabricating extremely long ultra-low-loss waveguides.

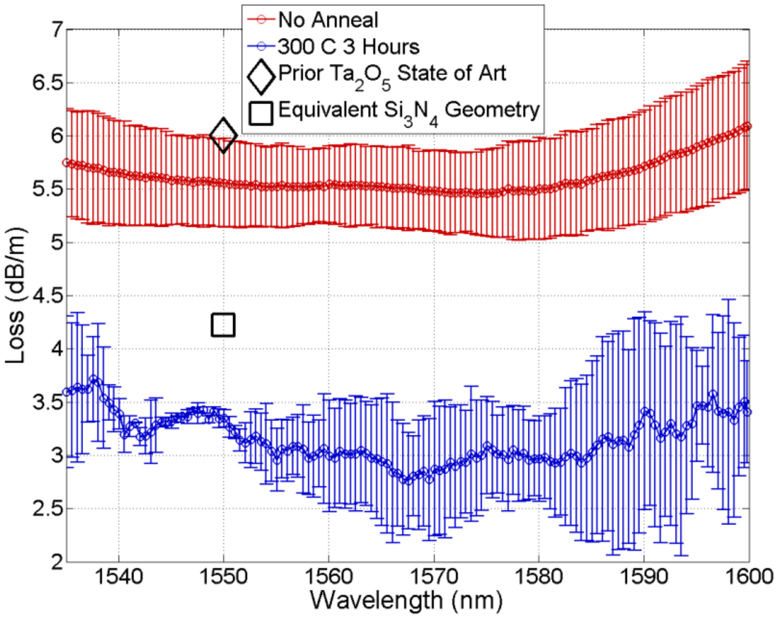

Figure 4.21: *Propagation loss (mean and standard deviation) vs. wavelength for 3 separate die of 10 m long 90 nm thick* Ta_2O_5 *core spiral delays. The lower cladding was 15 µm of thermal* SiO_2 *on a Si substrate, while the upper cladding was 1.1 µm of sputtered* SiO_2*. Due to the sputter deposition of the upper cladding, the loss is relatively flat (<2 dB/m spread) over the entirety of the C-band. The prior state of the art* Ta_2O_5 *measurement result from [16] is shown with a diamond marker. The loss measurement from [11] of an equivalent geometry with a* Si_3N_4*-core is shown with a square marker.*

4.6.2.2 Strongly Guiding Deeply Etched Waveguides

To test the optical loss of these waveguides, 30.5 cm long Archimedean spiral delays with an innermost minimum bend radius of 10 µm were fabricated. The cross section of the structure is equivalent to that shown in Figure 4.2. Figure 4.22 shows reflection amplitude data, as well as the spectral dependence of the propagation loss over the entirety of the telecommunications O-band.

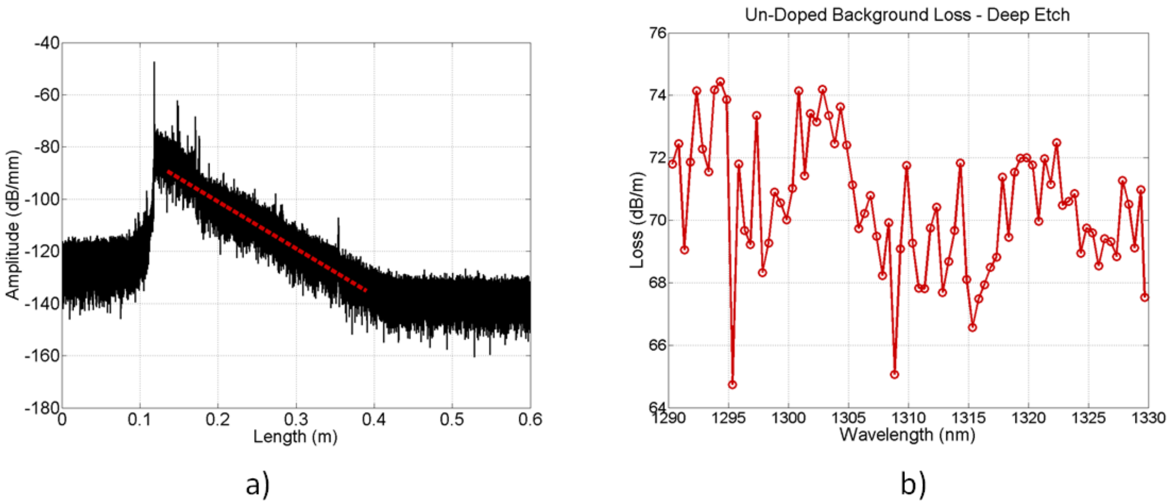

Figure 4.22: *(a) OBR data from the 30.5 cm long spiral delay, with an equivalent cross section as that shown in Figure 4.2. The dashed red line gives a linear fit of the waveguide backscatter averaged over all measured wavelengths. Bend loss was not measurable compared to the propagation loss as experienced over the entirety of propagation through the spiral as evidenced by the constant slope of the measured backscattered power with respect to distance. (b) Spectral dependence of the propagation loss. The various scatter events that the optical signal experiences throughout its propagation along the 30.5 cm waveguide delay cause the non-uniform spectral dependence as shown.*

4.6.2.3 Deep to Shallow Transition Sections

To test the optical loss of the adiabatic waveguide transitions, waveguide coupler ‘tree’ test structures with various deeply etched taper section, taper section, and bend radius were fabricated. Figure 4.23 gives the mask layout of the block of test structures, as well a diagram of the experimental setup.

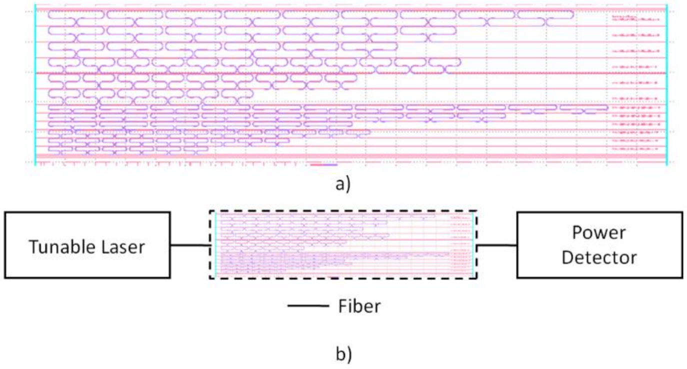

Figure 4.23: *(a) GDS mask layout of the deep-to-shallow adiabatic taper transition test structure block. Each bend radius and taper configuration has multiple repeats with an increasing number of bends and tapers. (b) Experimental measurement setup. The fiber-to-chip coupling was accomplished using 5.0 µm (1/e^2) spot-sized lensed fibers. All other fiber connections are made using Corning SMF-28 fibers.*

The layout of the test structures is such that when insertion loss is plotted against the number of tapers within a path, the slope of the resulting line will supply the loss per taper and the y-intercept of the line will give the fiber-to-chip coupling loss. Table 4.2 provides a collection of the different taper configurations fabricated along with their resulting measured insertion loss at the 1330 nm wavelength. From the measurements presented in Figure 4.22, it is concluded that the loss from the 180° bend is dominated not by the propagation through the bend itself (which for radii of 62.5 µm and 125 µm will contribute only 0.02 dB and 0.05 dB, respectively), but rather by the adiabatic transition sections.

Table 4.2: *Resulting measured loss per taper for the fabricated taper designs. The data as displayed is for the 1330 nm wavelength, but the results are similar throughout the entire collected wavelength range from 1300-1360 nm. The loss in the case of the 200 µm long taper*

section, 100 μm long straight section, and 62.5 μm bend radius was too high for the detector to detect any measurable signal.

Taper Length (um)	Straight Length (um)	Bend Radius (um)	Loss per 180^o Bend	Loss per Taper
100	0	62.5	1.68	0.84
100	0	125	1.2	0.6
200	100	62.5	x	x
200	100	125	2.44	1.22

In the case of either the 62.5 μm or 125 μm radius configurations, the design with the shortest taper length performs best (exhibits the lowest loss). These results illustrate the engineering trade-off that exists between complete adiabaticity and excess scattering loss, as from merely a mode-conversion analysis (given in Figure 4.5) the longer length design would be expected to function more efficiently.

4.7 Sidewall Bragg Grating Filter Characterization

The experimental setup used to characterize the waveguide sidewall Bragg grating spectra is shown in Figure 4.24. CW output from a tunable laser was sent through a circulator to a 3-paddle polarization controller (PC) and then subsequently coupled into the grating waveguides by way of a 5 μm spot size, 25 μm working distance lensed fiber. Index matching fluid was used to improve the coupling efficiency between the lensed fiber and the diced facet. Before grating measurements were taken, the TE/TM extinction ratio of the polarization controller was measured as 15 dB. This was done at the output of the lensed fiber using a free-space polarization splitter (PS) with 30 dB of extinction and a free-space Ge detector.

Light transmitted through the grating was collected with a microscope objective, passed through a polarization splitter, and focused onto an infrared camera by way of a Navitar modular zoom lens system. This allowed for quick and repeatable alignment of the input fiber to the grating waveguide. Light reflected by the grating was sent back through the circulator and detected by a broadband InGaAs photodetector.

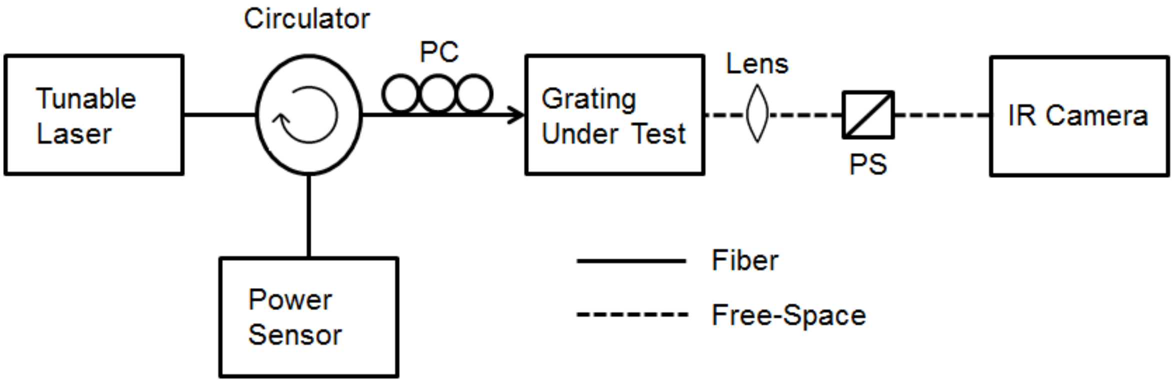

Figure 4.24: *Experimental measurement setup. All fibers connections are made using Corning SMF-28 fibers. The lens at the output of the grating under test before the PS is a standard 20x microscope objective.*

4.7.1 Reflection Characterization

Figure 4.25 shows the reflectivity spectrum of two separate gratings, each with a different value of width difference (which directly corresponds to the coupling constant). Both gratings feature an 80 nm Si_3N_4 core with a nominal waveguide width of 2.8 μm and lower thermal SiO_2 cladding and upper bonded thermal SiO_2 cladding of 15 μm thickness.

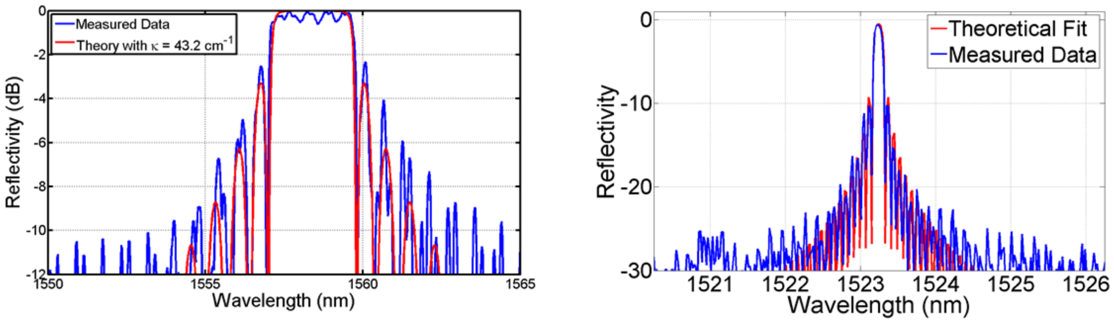

Figure 4.25: *(Left) Measured and theoretically predicted (T-matrix) spectra of a 1 mm long grating under TE excitation with a 1.2 μm width difference. The grating strength here is relatively strong (κL product = 43), which is the cause of the characteristically wide passband. (Right) Measured and theoretically predicted spectra of a 1 cm long grating under TE excitation with a 0.2 μm width difference. The grating strength here is relatively weak (κL product = 4), which is the cause of the characteristically narrow passband.*

As is shown, the coupled mode theory analysis and design approach described in Section 4.3 is able to accurately describe the behavior of the measured fabricated grating structure. All the tested grating geometries had a constant mean width ((wide section width + narrow section width)/2) of 2.8 μm. The grating reflectivity spectra exhibit the characteristic sinc function dependence that one expects for small grating perturbation values.

4.7.2 Grating Coupling Constant

The measured bandwidths for two sets of fabricated gratings are given in Figure 4.26, which also gives fitted coupling constant values for the same sets of fabricated gratings. The simulated curve here is the result of a two-dimensional finite difference method numerical mode solution from the FIMMWAVE software package.

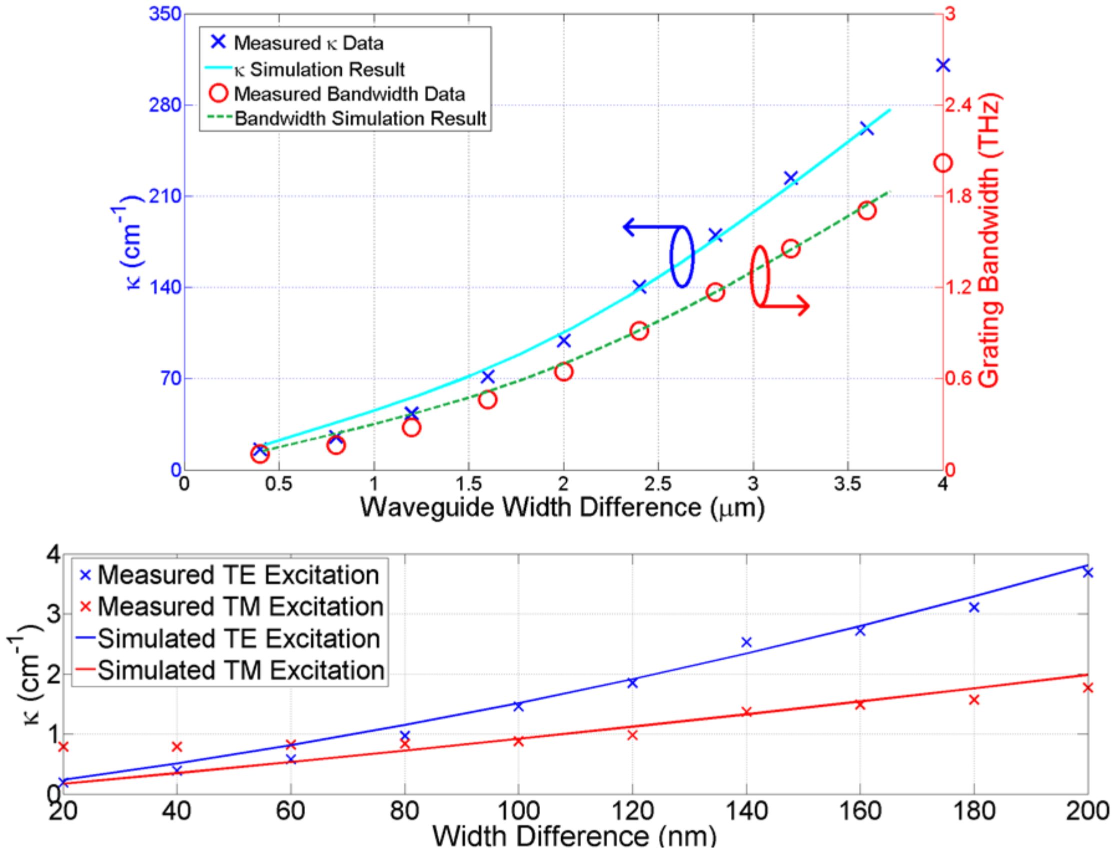

Figure 4.26: *(Top) Measured and simulated (FIMMWAVE and T-matrix) grating bandwidth for 1000 μm long gratings under TE or TM excitation. The plot also gives fitted and simulated coupling constant values for the same set of gratings. The nominal waveguide width is 2.8 μm and the waveguide core thickness is 80 nm. For an increased core thickness is it expected that these measured κ values would decrease. This is because as the core thickness increases, a changing waveguide width has less impact on an overall effective index change for the structure. (Bottom) Measured grating coupling constants for 1 cm long gratings under either TE or TM excitation. The nominal waveguide width is 2.8 μm and the waveguide core thickness is 80 nm. The plot also gives fitted coupling constant values (κ) for the same set of gratings.*

A wide range of coupling constant values, and hence grating bandwidths, can be achieved through proper waveguide width design. Such a broad range of potential κ values illustrates the wide array of applications, such as narrow linewidth mirrors, integrated pump filters, and even integrated grating-based sensors, made possible within this waveguide platform.

4.8 Racetrack Ring Resonator Characterization

The experimental setup used to characterize the racetrack ring resonator transmission spectra is shown in Figure 4.27. CW output from an O-band tunable laser was sent through a a 3-paddle polarization controller (PC) and then subsequently coupled into the ring bus waveguides by way of a 5 μm spot sized lensed fiber. Before grating measurements were taken, the TE/TM extinction ratio of the polarization controller was measured as 15 dB. This was done at the output of the lensed fiber using a free-space polarization splitter (PS) with 30 dB of extinction and a free-space Ge detector.

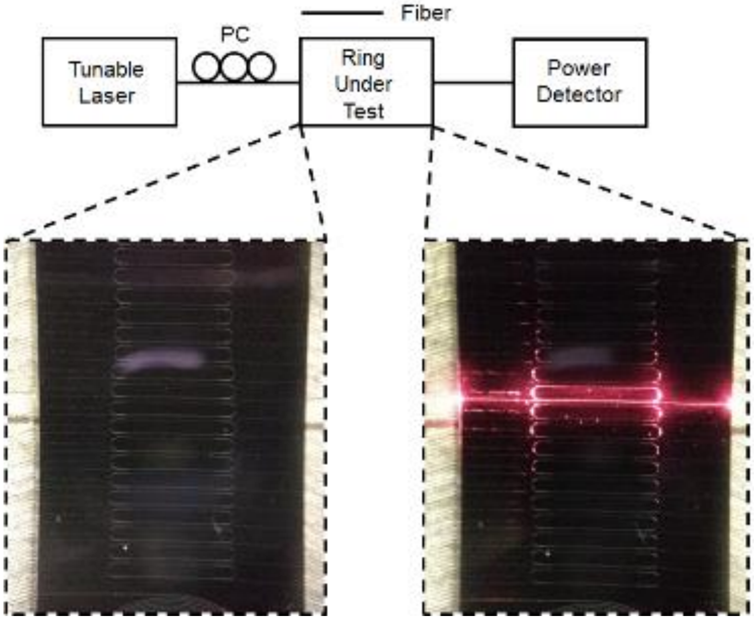

Figure 4.27: *Experimental measurement setup. All fibers connections are made using Corning SMF-28 fibers. The smaller pictures shown in the inset are optical micrograph*

images of a bar of rings before (left) and after (right) illumination from a red (635 nm) laser source.

Figure 4.28 shows the transmission spectrum of a fabricated racetrack ring resonator cavity with a cross section profile like that shown in Figure 4.2.

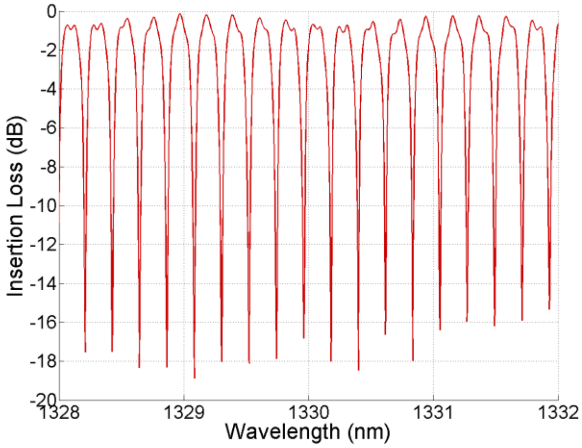

Figure 4.28: *Measured spectra of a 4.78 mm long bus-coupled ring resonator cavity under TE excitation. This particular design iteration featured deeply etched bent waveguides with a 125 μm bend radius and deep to shallow taper transition sections that were 100 μm long.*

The loaded quality factor, or Q, of the resonator, which is a figure of merit that measures the ratio of energy stored vs. lost per unit time for this resonator was measured to be 20,615. Similar loaded Q's were measured for complimentary designs that featured a 250 μm bend radius.

4.9 Summary and Conclusions

This chapter began by introducing the design and analysis framework for a collection of passive waveguide elements on an ultra-low loss Si_3N_4-based platform. Weekly guiding shallowly etched and strongly guiding deeply etched waveguides were presented, as was an adiabatic transition region that allows for coupling between the two. Next, waveguide sidewall Bragg gratings were analyzed, as were bus-coupled racetrack ring resonators that incorporate all three of the waveguide elements introduced previously. An overview of the steps required to fabricate each of these passive components and devices was provided, with a more detailed process traveler made available in Appendix 1. Finally, each structure was tested and quantified for performance. The shallowly-etched Ta_2O_5-core waveguides had losses as low as 3±1 dB/m across the entire telecommunications C-band and the deeply etched waveguides with a bend radius down to 62.5 μm exhibited losses in the 70 dB/m range across the entire telecommunications O-band. The adiabatically tapered waveguide mode converters demonstrated losses as low as 0.6 dB/transition. The measurement of the waveguide sidewall gratings in Si_3N_4-core waveguides showed a vast range of coupling constants between 0.19 and 310 cm^{-1}. Finally, a set of measurements of bus-coupled racetrack ring resonators was conducted and presented, which showed resonator loaded Q's in the 20,000 range.

4.10 References

[1] J. Bauters, “Ultra-Low Loss Waveguides with Application to Photonic Integrated Circuits,” Ph.D. Dissertation (Department of Electrical and Computer Engineering, University of California Santa Barbara, 2013).

[2] S. Gundavarapu, T. Huffman, M. Belt, R. Moreira, J. Bowers, and D. Blumenthal, “Integrated Ultra-Low-Loss Silicon Nitride Waveguide Coil for Optical Gyroscopes,” in *Optical Fiber Communication Conference*, OSA Technical Digest (online) (Optical Society of America, 2016), paper W4E.5.

[3] R. Halir, A. Maese-Novo, A. Ortega-Moñux, I. Molina-Fernández, J. G. Wangüemert-Pérez, P. Cheben, D.-X. Xu, J. H. Schmid, and S. Janz, "Colorless directional coupler with dispersion engineered sub-wavelength structure," Opt. Express 20, 13470-13477 (2012).

[4] M. Belt, J. Bovington, R. Moreira, J. F. Bauters, M. J. R. Heck, J. S. Barton, J. E. Bowers, and D. J. Blumenthal, "Sidewall gratings in ultra-low-loss Si_3N_4 planar waveguides," Opt. Express 21, 1181-1188 (2013).

[5] M. Belt, M. Heck, J. Barton, J. Bauters, J. E. Bowers, and D. J. Blumenthal, "Apodized and Un-Apodized Sidewall Grating Filters with Low Coupling Constants in Ultra-Low-Loss Si3N4 Planar Waveguides," in *Optical Fiber Communication Conference/National Fiber Optic Engineers Conference 2013*, OSA Technical Digest (online) (Optical Society of America, 2013), paper OTu3C.3.

[6] S. Ezhilvalava and T. Y. Tseng, “Preparation and properties of tantalum pentoxide (Ta_2O_5) thin films for ultra large scale integrated circuits (ULSIs) application – A review,” Journ. Mater. Science: Mater. In Electron. 10(1), 9-31 (1999).

[7] C. Chaneliere, J.L. Autran, R.A.B. Devine, and B. Ballard, “Tantalum pentoxide (Ta_2O_5) thin films for advanced dielectric applications,” Mater. Science and Eng. 22(6), 269-322 (1998).

[8] A. Subramanian, “Tantalum Pentoxide Waveguide Amplifier and Laser for Planar Lightwave Circuits,” Ph.D. dissertation (Department of Physical and Applied Sciences, Optoelectronics Research Center, University of Southampton, 2011).

[9] R. J. Deri and E. Kapon, “Low-loss III-V semiconductor optical waveguides,” IEEE Journal of Quantum Electronics, vol. 27, pp. 626–40, 1991.

[10] D. John, J. Bauters, J. Nedy, W. Li, R. Moreira, J. Bowers, D. J. Blumenthal, and J. Barton, "Fabrication and Demonstration of a Pure Silica-Core Waveguide Utilizing a Density-Based Index Contrast," in *Optical Fiber Communication Conference/National Fiber Optic Engineers Conference 2011*, OSA Technical Digest (CD) (Optical Society of America, 2011), paper OWS3.

[11] J.F. Bauters, M.J.R. Heck, D. John, D. Dai, M.-C. Tien, J.S. Barton, A. Leinse, R.G. Heideman, D.J. Blumenthal, and J.E. Bowers, “Ultra-low-loss high-aspect-ratio Si_3N_4 waveguides,” Opt. Express 19(4), 3163-3174 (2011).

[12] J.F. Bauters, M.L. Davenport, M.J.R. Heck, J.K. Doylend, A. Chen, A.W. Fang, and J.E. Bowers, "Silicon on ultra-low-loss waveguide photonic integration platform," Opt. Express 21(1), 544-555 (2013).

[13] K. Thyagrajan, M. R. Shenoy, and A. K. Ghatak, “Accurate numerical method for the calculation of bending loss in optical waveguides,” Optics Letters, vol. 12, pp. 296–8, 1987.

[14] J.F. Bauters, M.J.R. Heck, D.D. John, J.S. Barton, C.M. Bruinink, A. Leinse, R.G. Heideman, D.J. Blumenthal, and J.E. Bowers, “Planar waveguides with less than 0.1 dB/m propagation loss fabricated with wafer bonding,” Opt. Express 19(24), 24090-24101 (2011).

[15] B.J. Soller, D.K. Gifford, M.S. Wolfe, and M.E. Froggatt, "High resolution optical frequency domain reflectometry for characterization of components and assemblies," Opt. Express 13(2), 666-674 (2005).

[16] M. Itoh, T. Kominato, M. Abe, M. Itoh, and T. Hashimoto, "Low-Loss Silica-Based SiO_2-Ta_2O_5 Waveguides With Extremely High Δ Fabricated Using Sputtered Thin Films," J. Lightwave Technol. 33, 318-323 (2015).

[17] V. V. Wong, W. Y. Choi, J. M. Carter, C. G. Fonstad, H. I. Smith, Y. Chung, and N. Dagli, “Ridge-waveguide sidewall-grating distributed feedback structures fabricated by x-ray lithography,” J. Vac. Sci. Technol. B 11(6), 2621–2624 (1993).

[18] J. T. Hastings, M. H. Lim, J. G. Goodberlet, and H. I. Smith, “Optical waveguides with apodized sidewall gratings via spatial-phase-locked electron-beam lithography,” J. Vac. Sci. Technol. B 20(6), 2753–2757 (2002).

[19] T. E. Murphy, J. T. Hastings, and H. I. Smith, “Fabrication and characterization of narrow-band Bragg-refection filters in silicon-on-insulator ridge waveguides,” J. Lightwave Technol. 19(12), 1938–1942 (2001).

[20] L. A. Coldren, S. W. Corzine, and M. L. Mašanović, Diode Lasers and Photonic Integrated Circuits (Wiley, 2012), Chap. 6.

[21] L. A. Coldren, S. W. Corzine, and M. L. Mašanović, Diode Lasers and Photonic Integrated Circuits (Wiley, 2012), Chap. 3.

[22] M. Yamada and K. Sakuda, “Analysis of almost-periodic distributed feedback slab waveguides via a fundamental matrix approach”, Applied Optics 26, 3474 (1987).

[23] A. Fang, “Silicon Evanescent Lasers,” Ph.D. Dissertation (Department of Electrical and Computer Engineering, University of California Santa Barbara, 2008).

[24] E. H. Bernhardi, H. A.G.M. van Wolferen, L. Agazzi, M. R.H. Khan, C. G.H. Roeloffzen, K. Wörhoff, M. Pollnau, and R. M. de Ridder, "Ultra-narrow-linewidth, single-frequency distributed feedback waveguide laser in Al_2O_3:Er^{3+}on silicon," Opt. Lett. 35, 2394-2396 (2010).

[25] T. E. Murphy, “Design, Fabrication and Measurement of Integrated Bragg Grating Optical Filters,” Ph.D. Dissertation (Department of Electrical and Computer Engineering, Massachusetts Institute of Technology, 2001).

[26] D. Pastor, J. Capmany, D. Ortega, V. Tatay, and J. Martí, “Design of apodized linearly chirped fiber gratings for dispersion compensation,” J. Lightw. Technol. 14(11), 2581-2588 (1996).

[27] D. G. Rabus, Integrated Ring Resonators: The Compendium (Springer, 2007), Chap. 1.

[28] M. Zhu, Z. Zhang, and W. Miao, “Intense photoluminescence from amorphous tantalum oxide films,” Appl. Phys. Lett. 89, 021915-1–021915-3 (2006).

[29] K. Wörhoff, J. D. B. Bradley, F. Ay, D. Geskus, T. P. Blauwendraat, and M. Pollnau, “Reliable low-cost fabrication of low-loss Al2O3:Er3+ waveguides with 5.4-dB optical gain,” IEEE J. Quantum Electron. 45(5), 454– 461 (2009).

[30] D. T. Spencer, M. Davenport, S. Srinivasan, J. Khurgin, P. A. Morton, and J. E. Bowers, "Low kappa, narrow bandwidth Si_3N_4 Bragg gratings," Opt. Express 23, 30329-30336 (2015).

[31] K. Hosomi, T. Kikawa, S. Goto, H. Yamada, T. Katsuyama, and Y. Arakawa, "Ultrahigh-aspect-ratio SiO_2 deeply etched periodic structures with smooth surfaces for photonics applications," Journ. of Vac. Sci. and Tech. B 24, 1226 (2006).

[32] E. R. Parker, B. J. Thibeault, M. F. Aimi, M. P. Rao, and N. C. MacDonald, "Inductively Coupled Plasma Etching of Bulk Titanium for MEMS Applications," J. Electrochem. Soc. 152(10), C675-C683 (2005).

Chapter 5

Rare-Earth-Ion-Doped Waveguide Amplifiers

In this thesis, amorphous Al_2O_3 (as opposed to its crystalline counterpart α-Al_2O_3, also known as sapphire) is exploited as a host material for the rare-earth ions that impart optical gain. Waveguides containing either neodymium (Nd^{3+}) or erbium (Er^{3+}) as a dopant are explored, as these elements, when excited, have luminescence output in either the telecommunications O-band (13xx nm, Nd^{3+}) or C-band (15xx nm, Er^{3+}). Due to its extremely broadband low loss nature, Al_2O_3 has additionally been considered and demonstrated as a suitable host material for a variety of other active ions emitting across wide wavelengths of interest. This includes ytterbium (Yb^{3+}) operating at 1020 nm [1][2] and thulium (Th^{3+}) operating near 1900 nm [3].

As discussed in Section 2, optically pumped monolithic rare-earth-ion-doped waveguides leveraging an Al_2O_3 host material on oxidized silicon substrates demonstrate significant market potential due to their wide gain bandwidths [4], high degree of thermal stability [5], low-cost highly repeatable back-end deposition method [6], and capability of handling high bit rate optical communication data streams [7]. The issue of such a gain material requiring an external optical pump laser has been reduced to merely a pump source / on-chip coupling issue as a consequence of recent cost reductions in the mass production of laser diode components. One such high power GaAs-based laser source could potentially pump many active devices in a PIC through a single fiber-to-chip connection.

Exceptional quality optical amplifiers capable of handling high optical signal powers are key components of any telecommunications and integrated optical system. While on the surface it may seem a straightforward endeavor to translate the concepts of rare-earth-ion-doped fiber amplifiers into a waveguide configuration, scaling down the amplifier's dimension from a few meters of fiber to a few centimeters or less of waveguide requires a proportional magnitude concentration increase of dopant ion to achieve the same optical gain. When doing so, many of the physical processes that were unimportant in fiber amplifiers play a significant role in determining the net optical gain in such waveguide amplifiers.

5.0 Chapter Synopsis

This chapter details the complete analysis, design, fabrication, and characterization of neodymium- and erbium-doped waveguide amplifiers operating in either the O-band or C-band. Sections 5.1 and 5.2 discuss the ion population dynamics under optical pumping and the considerations taken when implementing a proper waveguide cross section. Section 5.3 gives an outline of the fabrication of these active waveguide amplifiers, with characterization measurements presented in Section 5.4. Optical gain of less than 0.5 dB/cm for the Al_2O_3:Nd^{3+} O-band waveguide amplifier under 808 nm pump excitation and optical gain greater than 1.5 dB/cm for the Al_2O_3:Er^{3+} C-band waveguide amplifier under 980 nm pump excitation is demonstrated.

5.1 Population Dynamics

5.1.1 Energy Transitions in Er^{3+} and Nd^{3+} Ions

First, the relevant energy transitions in the erbium (Er^{3+}) ion are given [8]. The lower-lying energy levels of Er^{3+}, starting from the ground state and continuing up to the $^4F_{7/2}$ level are shown in Figure 5.1. The levels are represented by Russell-Saunders notation $^{2S+1}L_J$, where 2S+1 represents the spin angular momentum, L represents the orbital angular momentum, and

J represents the total angular momentum. In rare earth ions, the eigenstates of the electronic system are usually a linear combination of $^{2S+1}L_J$ states. However, to simplify the notation each level is represented by the leading term of the Russell-Saunders coupled states.

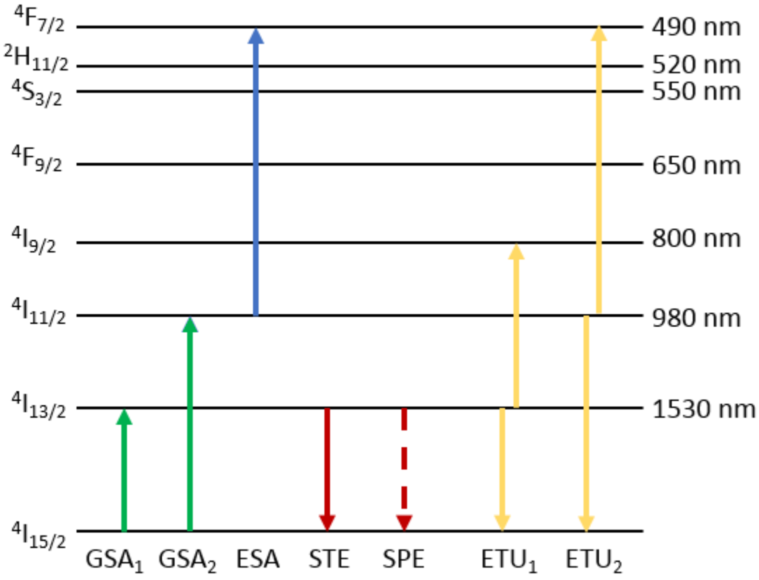

Figure 5.1: *Schematic of the energy levels in the* Er^{3+} *ion. The wavelength corresponding to a photon at each specific energy level also indicated. GSA*$_1$*: Ground State Absorption at 1480 nm. GSA*$_2$*: Ground State Absorption at 980 nm. ESA: Excited State Absorption at 980 nm. STE: Stimulated Emission centered at 1530 nm. SPE: Spontaneous Emission centered at 1530 nm. ETU*$_1$*: Energy Transfer Upconversion between two neighboring ions in the* $^4I_{13/2}$ *manifold. ETU*$_2$*: Energy Transfer Upconversion between two neighboring ions in the* $^4I_{11/2}$ *manifold.*

The metastable $^4I_{13/2}$ level has a long lifetime of several milliseconds, which can be used to create a population inversion with respect to the ground state. Pump light at a wavelength of 980 nm or 1480 nm can be used to populate the $^4I_{13/2}$ level. Pumping at 1480 nm will excite ions from the $^4I_{15/2}$ ground state to the upper Stark levels of the $^4I_{13/2}$ first excited state. Alternatively, an indirect pumping of the $^4I_{13/2}$ level can be achieved with a 980 nm pump, where the ions are first pumped from the ground state to the $^4I_{11/2}$ level, followed by rapid non-radiative decay to the $^4I_{13/2}$ level [9].

Figure 5.2 shows a schematic representation of a selection of possible energy transitions of neodymium (Nd^{3+}) ions [10][11].

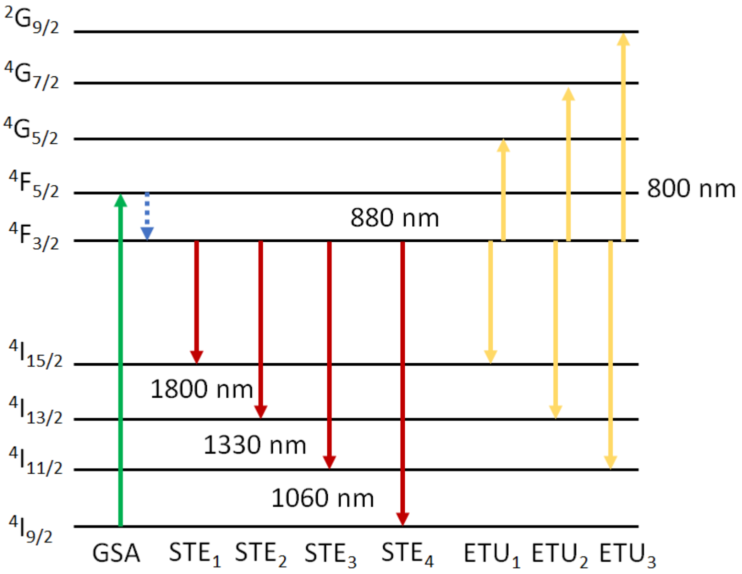

Figure 5.2: *Schematic of the energy levels in the* Nd^{3+} *ion. The wavelength corresponding to a photon at each specific energy level also indicated. GSA: Ground State Absorption at 800 nm.* STE_1*: Stimulated Emission centered at 1800 nm.* STE_2*: Stimulated Emission centered at 1330 nm.* STE_3*: Stimulated Emission centered at 1060 nm.* STE_4*: Stimulated Emission centered at 880 nm.* $ETU_{1\text{-}3}$*: Energy Transfer Upconversion between two neighboring ions in the* $^4F_{3/2}$ *manifold.*

In Figure 5.2, the absorption of 800 nm pump photons causes excitation of the Nd^{3+} to the $^4F_{5/2}$ level. After a fast relaxation, the ion remains in the metastable $^4F_{3/2}$ level with a lifetime that is typically in the order of hundreds of microseconds in case of low concentrations in different hosts. The corresponding pump levels ($^4F_{5/2}$, $^4F_{7/2}$, $^4G_{5/2}$, and $^4G_{7/2}$) as well as the lower laser levels are depleted by fast multi-phonon relaxation leading to significant excitation solely in the $^4F_{3/2}$ level [10][11]. After relaxation to the $^4F_{3/2}$ level, several radiative decays to the $^4I_{9/2}$, $^4I_{11/2}$, $^4I_{13/2}$, and $^4I_{15/2}$ levels, corresponding to the wavelength bands centered at 880 nm, 1060 nm, 1330 nm and 1800 nm, respectively, can take place [12].

5.1.2 Rate Equations

In the previous section, the various transition processes within the energy band diagrams of the Er^{3+} and Nd^{3+} ions were considered. Here, a rate equation model is developed that describes these transitions mathematically. For the Er^{3+} ion the approach in [9] is taken, while for the Nd^{3+} ion the approach taken in [12] is followed.

5.1.2.1 Rate Equations for Er^{3+} Ions

For the rate equation model, the Er^{3+} ions will be pumped at a wavelength of 980 nm, which is described using three energy levels (the $^4I_{15/2}$ ground state (N_0), the $^4I_{13/2}$ first excited level (N_1), the $^4I_{11/2}$ pump excitation level (N_2), and a total doping concentration N_T. With the population density of the $^4I_{11/2}$ level being small due to a relatively short lifetime and rapid non-radiative relaxation to the $^4I_{13/2}$ level, as well as the fact that energy migration was observed to be significantly slower in the $^4I_{11/2}$ second excited state as compared to the $^4I_{13/2}$ first excited state [13], the influence of ETU from this second excited level into the higher-lying $^4F_{7/2}$ level is excluded from the model. Further it is assumed that ESA from the $^4I_{11/2}$ level only contributes to the reduction of pump power but does not affect the population dynamics in any other way, since excitation to higher lying levels will result in rapid non-radiative relaxation back to the $^4I_{11/2}$ level. The rate equations describing the population densities of the first two energy manifolds shown in Figure 5.1 are given by:

$$\frac{dN_2}{dt} = R_{02}N_0 - R_{20}N_2 - R_{21}N_2 + W_{ETU}N_1^2 \tag{5.1}$$

$$\frac{dN_1}{dt} = R_{01}N_0 - R_{10}N_2 + R_{21}N_2 - 2W_{ETU}N_1^2 \tag{5.2}$$

W_{ETU} is the macroscopic material-dependent ETU parameter, which represents the probability of the ETU process occurring from the first excited $^4I_{13/2}$ level. R_{02} and R_{01} are the rates at which ions are transferred from the ground state to the first and second excited states, respectively, by means of the absorption of radiation. In the case of R_{02} it concerns the absorption of 980 nm pump radiation, while R_{01} describes the absorption of 15xx nm laser radiation. R_{20} is the rate at which ions are de-excited from the second excited state back to the ground state via stimulated emission of 980 nm pump radiation, while R_{10} is the rate at which ions are de-excited from the first excited state back to the ground state via stimulated and spontaneous emission. R_{21} is the rate at which ions are transferred from the second to the first excited state by means of a rapid non-radiative transition. Note that the population densities and respective transition rates in Equations 5.1 and 5.2 are spatially dependent, however here the spatial coordinates are omitted for the sake of readability. The respective rates for the energy levels given in Figure 5.1 are defined by:

$$\boldsymbol{R_{02}} = \frac{\boldsymbol{P_P(z)\phi_p(x,y)}}{\boldsymbol{h\nu_P}}\boldsymbol{\sigma_p^{abs}} \tag{5.3}$$

$$\boldsymbol{R_{20}} = \frac{\boldsymbol{P_P(z)\phi_p(x,y)}}{\boldsymbol{h\nu_P}}\boldsymbol{\sigma_p^{em}} \tag{5.4}$$

$$\boldsymbol{R_{21}} = \frac{\boldsymbol{1}}{\boldsymbol{\tau_2}} \tag{5.5}$$

$$\boldsymbol{R_{01}} = \frac{\boldsymbol{P_L(z)\phi_L(x,y)}}{\boldsymbol{h\nu_L}}\boldsymbol{\sigma_L^{abs}} \tag{5.6}$$

$$\boldsymbol{R_{20}} = \frac{\boldsymbol{P_L(z)\phi_L(x,y)}}{\boldsymbol{h\nu_L}}\boldsymbol{\sigma_L^{em}} + \frac{\boldsymbol{1}}{\boldsymbol{\tau_1}} \tag{5.7}$$

where τ_1 and τ_2 represent the luminescence lifetime of the first and second excited states, respectively, and P is the total optical power at position z along the cavity. The subscripts P and L denote pump and laser, respectively. $\phi(x,y)$ is a normalized transverse intensity distribution, such that:

$$\iint_{-\infty}^{\infty} \boldsymbol{\phi(x,y)dxdy = 1} \tag{5.8}$$

h is Planck's constant, ν is the optical frequency, and σ_{abs} and σ_{em} represent the effective absorption and emission cross sections, respectively. These cross sections will be described in greater detail in Section 5.1.3. It is assumed that the following boundary condition is true:

$$\boldsymbol{N_0 = N_T - (N_1 + N_2)} \tag{5.9}$$

In the case of a continuous-wave laser, the population densities of the respective energy levels are in a steady state, so that Equations 5.1 and 5.2 are equal to zero. From this assumption, it follows that:

$$N_2 = \frac{R_{02}(N_T - N_1) + W_{ETU}N_1^2}{R_{02} + R_{20} + R_{21}} \tag{5.10}$$

$$N_1 = \frac{\sqrt{B^2 - 4AC} - B}{2A} \tag{5.11}$$

where A, B, and C are given by:

$$A = W_{EUT}\left(2 + \frac{R_{01} - R_{21}}{R_{02} + R_{20} + R_{21}}\right) \tag{5.12}$$

$$B = R_{01} + R_{10} + \frac{R_{02}(R_{21} - R_{01})}{R_{02} + R_{20} + R_{21}} \tag{5.13}$$

$$C = -\left(R_{01}N_T + \frac{R_{02}N_T(R_{21} - R_{01})}{R_{02} + R_{20} + R_{21}}\right) \tag{5.14}$$

In Chapter 6 this rate equation model is combined with the T-matrix model presented in Chapter 4 to describe the lasing behavior of the devices presented.

5.1.2.2 Rate Equations for Nd^{3+} Ions

For the rate equation model of the Nd^{3+} ions, the equations describing the population densities of the energy manifolds shown in Figure 5.2 are given by:

$$\frac{dN_8}{dt} = W_3 N_4^2 - \frac{N_8}{\tau_8} \tag{5.15}$$

$$\frac{dN_7}{dt} = W_2 N_4^2 + \frac{N_8}{\tau_8} - \frac{N_7}{\tau_7} \tag{5.16}$$

$$\frac{dN_6}{dt} = W_1 N_4^2 + \frac{N_7}{\tau_7} - \frac{N_6}{\tau_6} \tag{5.17}$$

$$\frac{dN_5}{dt} = R_{05} + \frac{N_6}{\tau_6} - \frac{N_5}{\tau_5} \tag{5.18}$$

$$\frac{dN_4}{dt} = \frac{N_5}{\tau_5} - \frac{N_4}{\tau_4} - 2(W_1 + W_2 + W_3) N_4^2 \tag{5.19}$$

$$\frac{dN_3}{dt} = \beta_{43} \frac{N_4}{\tau_4} - \frac{N_3}{\tau_3} + W_1 N_4^2 \tag{5.20}$$

$$\frac{dN_2}{dt} = \beta_{42} \frac{N_4}{\tau_4} + \frac{N_3}{\tau_3} - \frac{N_2}{\tau_2} + W_2 N_2^2 \tag{5.21}$$

$$\frac{dN_1}{dt} = \beta_{41} \frac{N_4}{\tau_4} + \frac{N_2}{\tau_2} - \frac{N_1}{\tau_1} + W_3 N_4^2 \tag{5.22}$$

$$\frac{dN_0}{dt} = -R_{05} + \beta_{40} \frac{N_4}{\tau_4} + \frac{N_1}{\tau_1} \tag{5.23}$$

where N_i and τ_i ($i = 0\text{-}8$) are the population density and lifetime of each of the Nd^{3+} energy levels, respectively. β_{4i} ($i = 0\text{-}3$) are the branching ratios of the transitions from $^4F_{3/2}$. W_1, W_2, and W_3 are the ETU parameters, and R_{05} is the rate of 800 nm pump absorption. When simulating optical gain in the 13xx nm region, these equations can be simplified. Since the terminating states $^4I_{13/2}$ of the transition at 13xx nm exhibit a very short lifetime on the order of a few ns, this transition constitutes a four-level system. The re-absorption at the signal wavelength can be neglected, and the rate equations can be simplified as follows:

$$\frac{dN_4}{dt} = R_{05} - R_{4i} - \frac{N_4}{\tau_4} - W_{ETU}N_4^2 \qquad (5.24)$$

$$N_0 = N_d - N_4 \qquad (5.25)$$

$$R_{4i} = \sigma_S^{em}\frac{\lambda_S}{hc}I_S N_4 \qquad (5.26)$$

$$R_{05} = \sigma_P^{abs}\frac{\lambda_P}{hc}I_P N_0 \qquad (5.27)$$

where N_d is the dopant concentration, N_0 is the ground state population density, and i = 1,2. σ_s^{em} is the stimulated emission cross section, σ_p^{abs} is the pump absorption cross section, λ_P and λ_S are the pump and signal wavelengths, and I_P and I_S the intensities of pump and signal light, respectively, launched into the waveguide in propagation direction z. h is Planck's constant. This rate equation model allows for the description of the Nd^{3+} doped amplifiers presented later in this chapter.

5.1.3 Absorption and Emission Cross Sections

In the previous two sections, various transition processes within the Er^{3+} and Nd^{3+} ions were considered and modeled. Here, the concept of emission and absorption cross sections of the different transitions is introduced. The cross sections describe the probability of an excited ion emitting a photon of equal phase and frequency to a photon incident upon it (stimulated emission) or an ion being excited to a higher energy state by absorbing an incident photon (stimulated absorption). The amount of emitted or absorbed optical power is proportional to the cross section of the ion and the incident optical intensity:

$$\boldsymbol{P_{abs/em}}\,(\boldsymbol{\lambda}) = \boldsymbol{\sigma_{abs/em}}(\boldsymbol{\lambda})\boldsymbol{I}(\boldsymbol{\lambda}) \tag{5.28}$$

where $\boldsymbol{P_{abs/em}}\,(\lambda)$ is the absorbed or emitted optical power, $\sigma_{abs}(\lambda)$ and $\sigma_{em}(\lambda)$ are the absorption and emission cross sections at a given wavelength λ, respectively, and I(λ) is the optical intensity [17]. Emission and absorption cross sections for Er^{3+} and Nd^{3+} within an Al_2O_3 host material have been thoroughly characterized and are given in [17] and [12]. Such ions suffer from stimulated emission cross sections whose values are typically four to five orders of magnitude smaller than semiconductors, namely several x 10^{-21} cm^2.

5.1.4 Energy Transfer Upconversion and Clustering

Due to the limited length of erbium-doped waveguides as compared to fibers, a high rare-earth-ion concentration is required to have sufficiently short pump absorption lengths to obtain the desired performance. However, as the doping concentration is increased, the average distance between Er^{3+} or Nd^{3+} ions is decreased. Energy transfer upconversion (ETU) is a dipole-dipole interaction between two Er^{3+} or Nd^{3+} ions and can have a significant impact on the performance of rare-earth-ion-doped lasers and amplifiers. Since ETU has a R^{-6} dependence on the inter-ionic radius R, the effect of ETU becomes more pronounced at high rare-earth-ion concentrations. For an erbium-doped waveguide amplifier, a fast quenching process occurs at the $^4I_{13/2}$ level (see Figure 5.1) in $Al_2O_3:Er^{3+}$ which limits the optimum Er^{3+} concentration to 1-2 × 10^{20} cm^{-3} [14][15][16]. In Nd^{3+}-doped materials, the three ETU processes originating in the metastable $^4F_{3/2}$ level (see Figure 5.2) have a significant impact on the performance of waveguide-based amplifiers and lasers. Since all terminating levels of ETU processes in the Nd^{3+} system exhibit fast multi-phonon decays into the $^4F_{3/2}$ and $^4I_{9/2}$ levels, they lead to comparable results concerning the population dynamics [10][11].

5.2 Waveguide Cross Section

The net modal gain (g_{mod}) of a rare-earth-doped amplifier is dependent upon the fractional overlap (Γ) of the signal with the gain structure (material) through the following relationship [19]:

$$\boldsymbol{g_{mod} = \Gamma g_{mat} - \alpha_i = \Gamma(\sigma_{em}(\lambda)N_2 - \sigma_{abs}(\lambda)N_1) - \alpha_i} \quad (5.29)$$

where $\sigma_{abs}(\lambda)$ and $\sigma_{em}(\lambda)$ are the stimulated absorption and emission cross-sections (described in Section 5.1.3), $N_2 - N_1$ is the difference between the population densities of the excited state and the ground state, and α_i is the optical propagation loss to extraneous scattering and absorption events. Using this equation as a guide, it is clear that for a high gain on-chip rare-earth-ion-doped waveguide amplifier the following four properties are preferred: 1) a high degree of overlap of the signal with the excited gain structure (high signal/pump overlap factor) to maximize Γ, 2) low optical propagation loss to minimize α_i, 3) a high stimulated emission cross section, and finally 4) a large density of excited ions. The optimization of both properties 3) and 4) is mainly a material engineering challenge, and the proper guidelines for maximizing amplifier performance through these parameters were covered in Section 5.1. The optimization of both properties 1) and 2) requires an appropriately engineered waveguide structure, which will be covered now.

Figure 5.3a and Figure 5.3b give a schematic representation of the cross section of a shallowly etched waveguide amplifier, while Figure 5.3c shows the simulated (FIMMWAVE by Photon Design) transverse electric (TE) polarized optical mode profile for the 1550 nm wavelength. Here the high aspect ratio Si_3N_4-core design featured in the ULL waveguide acts as a lateral guide for the optical mode.

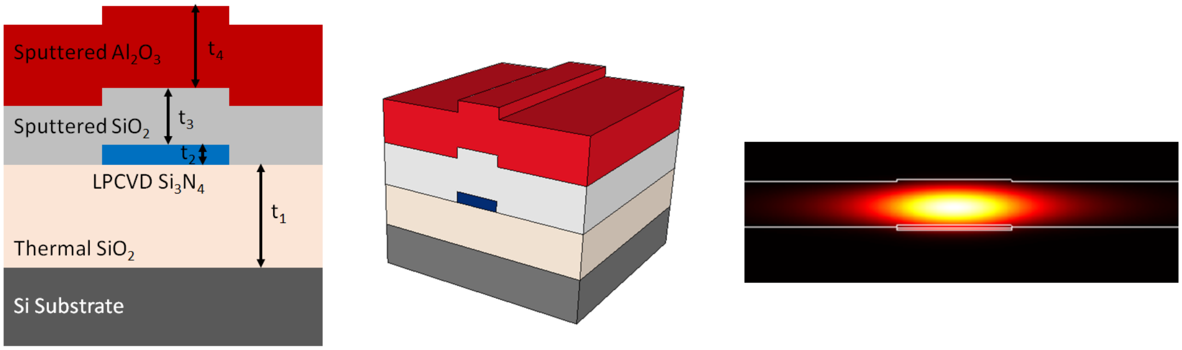

a) b) c)

Figure 5.3: *(a) Cross-sectional geometry of an on-chip* Si_3N_4*-core/*SiO_2*/*Al_2O_3*-clad rare-earth-ion-doped waveguide amplifier. The* Al_2O_3 *layer will act as a host for any dopant ions incorporated during the deposition process. The respective layer thicknesses are as follows:* $t_1 = 15.0\ \mu m$, $t_2 = 0.08\ \mu m$, $t_3 = 0.1\ \mu m$, $t_4 = 1.5\ \mu m$. *The width of the* Si_3N_4*-core is 2.8* μm. *It is this* Si_3N_4*-core that provides the majority of the lateral guiding of the optical mode. (b) Three-dimensional schematic image of the geometry. (c) Simulated (FIMMWAVE) optical mode profile of the fundamental TE waveguide mode at the 1.55* μm *wavelength. Here the effective index of the mode is 1.60.*

Such a waveguide design as presented obtains >85% confinement factor for all wavelengths longer than 800 nm and >90% intensity overlap factor with either an 808 nm or 980 nm optical pump over the entire near-infrared wavelength range, demonstrating insensitivity of mode profiles at various wavelengths. This design also ensures single transverse-mode operation at the pump (including 800 nm, 980 nm, and 1480 nm) and signal wavelengths (1330 nm and 1550 nm) and a strong interaction between the pump and signal light fields and the rare-earth ions. The drawback of this design is that the minimum bend radius is greater than 10 mm. Section 4.2.2 details a deeply etched waveguide design that alleviates this constraint, while keeping optical confinement in the Al_2O_3 rare-earth-ion-doped layer >85%.

5.3 Component Fabrication Overview

Figure 5.4 gives a graphical representation of the entirety of the waveguide fabrication process, as was similarly presented in Section 4.5. As noted previously, Appendix 1 provides a ‘traveler’ that includes the in-house process steps that follow this diagram. This section will outline the fabrication steps required, with additional details already presented in Section 4.5.

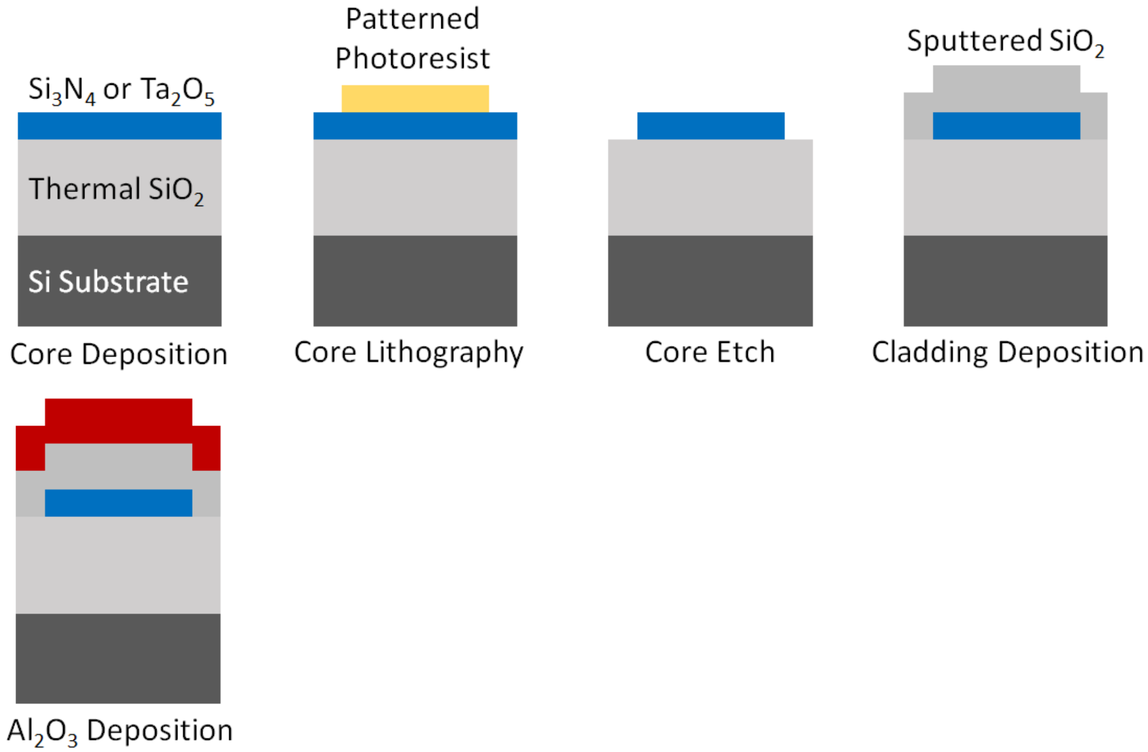

Figure 5.4: *Schematic overview of the fabrication process for the rare-earth-ion-doped waveguided amplifier.*

Waveguide fabrication begins with either a 500 μm or a 1 mm thick 100 mm diameter silicon substrate upon which 15 microns of silica is thermally grown by wet oxidation for the lower cladding. Next, either the Si_3N_4 waveguide core is deposited by low pressure chemical vapor deposition (LPCVD). This core layer is then patterned using a photoresist mask by 248 nm stepper lithography and an optimized $CH_3/CF_4/O_2$ inductively coupled plasma etch. The etching chamber had $CH_3/CF_4/O_2$ gas flows of 35/5/10 cm^3/min, a pressure of 0.5 Pa, an RF source power of 500 W, and an RF bias of 50 W. The patterning and etch steps are followed by a blanket sputter deposition of the upper SiO_2 cladding. At this stage in the fabrication, the wafer will undergo an anneal protocol of 7 hours long at 1050 ^oC in 3.0 SLPM N_2 atmosphere. Following annealing, the rare-earth-ion dopant layer within the Al_2O_3 host material will next be deposited by a reactive co-sputtering process [6]. Finally, the wafer is diced into separate die and a mechanical polishing process conditions the device facets. This process is essential to ensure maximum fiber-to-chip coupling efficiency and waveguide-to-waveguide uniformity.

5.4 Measurement of Rare-Earth-Ion-Doped Waveguide Amplifiers

The experimental setup used to characterize the on-chip rare-earth-ion-doped waveguide amplifiers is shown in Figure 5.5. CW output from a tunable laser (covering the C-band in the case of Er^{3+} doping or covering the O-band in the case of Nd^{3+} doping) was sent through a 3-paddle polarization controller (PC) and then through a fiber pump/signal multiplexer (980/1550 in the case of Er^{3+} doping or 800/1340 nm in the case of Nd^{3+} doping). The signal light was then subsequently coupled into the amplifier waveguides by way of a 5 μm spot size, 25 μm working distance lensed fiber. Before amplifier measurements were taken, the TE/TM extinction ratio of the polarization controller was measured as 15 dB. This was done at the output of the lensed fiber using a free-space polarization splitter (PS) with 30 dB of extinction and a free-space Ge detector. Pump light from 800 nm or 980 nm diodes was transferred onto the sample through these same multiplexers as the O-band or C-band signal light. The amplified signal light was collected at the chip output and measured through either a rack-mounted optical power meter or an optical spectrum analyzer (OSA).

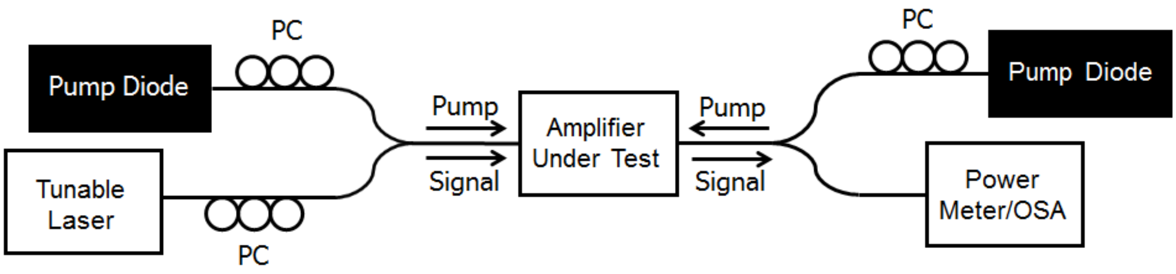

Figure 5.5: *Experimental measurement setup. In the case of an* Er^{3+}*-doped waveguide, the pump diodes output light in the 980 nm wavelength range. In the case of an* Nd^{3+}*-doped waveguide the pump diodes output light in the 800 nm wavelength range. The pump/signal multiplexers are also interchanged depending upon the dopant used, with a 980/1550 nm configuration in place for* Er^{3+} *doping and an 800/1340 nm configuration in place for* Nd^{3+} *doping.*

In the case of either amplifier configuration, approximately 1 μW of signal power was launched into the waveguide to ensure that the measured gain was in the small signal limit.

5.4.1 C-Band Measurements: Er-Doped Waveguide Amplifiers

Figure 5.6 shows measured C-band optical gain for an Al_2O_3:Er^{3+} waveguide amplifier under excitation from a pair of 980 nm pump diodes.

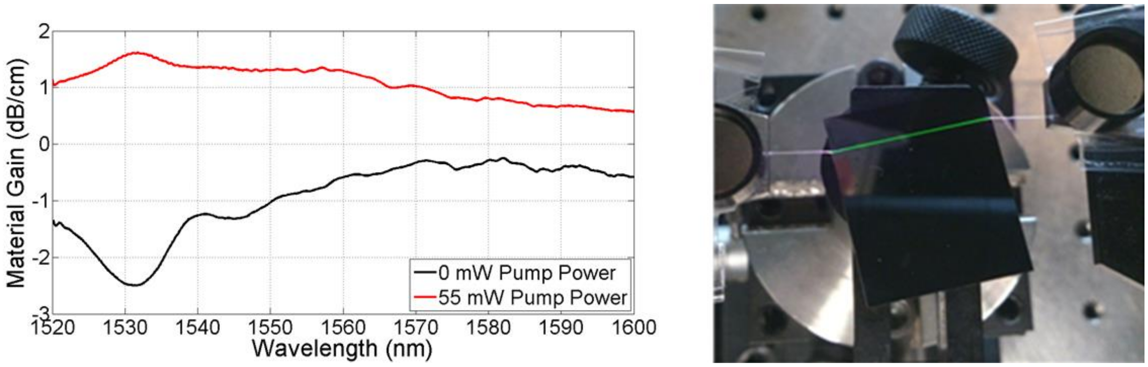

Figure 5.6: *(Left)Gain and un-pumped loss of a 2.1 cm long waveguide amplifier with an Er concentration of 1.3 x* 10^{20} cm^{-3}. *The background loss* (α_i) *measured through optical backscattering reflectometry of an un-doped waveguide with an equivalent cross-section configuration was 0.2 dB/cm across this wavelength range. (Right) Top-down view of the amplifier under test showing detrimental energy transfer upconversion (green emission).*

The gain peak centered at 1530 nm is characteristic of the luminescence spectrum of the Er^{3+} ion. Under 1480 nm pumping, lower population inversion is expected theoretically due to stimulated emission at the pump wavelength from the highly populated $^4I_{13/2}$ level, thus reducing the maximum net gain that can be achieved. The same effect is much less pronounced when pumping at 980 nm due to the fast nonradiative quenching and, hence, lower population density of the $^4I_{11/2}$ pump level [4][20].

5.4.2 O-Band Measurements: Nd-Doped Waveguide Amplifiers

Figure 5.7 shows measured O-band optical gain for an $Al_2O_3{:}Nd^{3+}$ waveguide amplifier under excitation from a pair of 808 nm pump diodes.

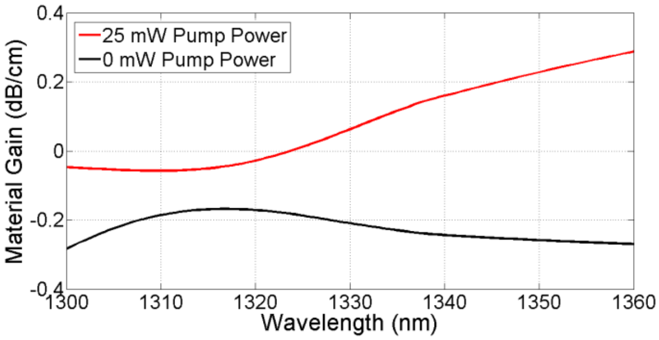

Figure 5.7: *Gain and un-pumped loss of a 2.1 cm long waveguide amplifier with an Nd concentration of 2.0 x* 10^{20} cm^{-3}*. The background loss (*α_i*) measured through optical backscattering reflectometry of an un-doped waveguide with an equivalent cross-section configuration was 0.3-0.4 dB/cm across this wavelength range. Peak gain in a neodymium-doped amplifier is expected to occur near 1340 nm [12], but this design instead measures a peak near 1360 nm. This is due to the decreased background loss present at longer wavelengths, in accordance with Equation 5.2. 1360 nm was the limit of the tunable laser in the setup, so further measurement of the gain out past 1360 nm was not possible. According to theory a higher pump power of 45 mW is expected to produce 1 dB/cm of gain across the same measured wavelength range.*

Despite low (1-2 dB/m) measured O-band propagation loss for the ULLW platform [21], the achieved O-band gain from such an $Al_2O_3:Nd^{3+}$-based waveguide amplifier configuration is still too low for the majority of desired on-chip applications, such as signal regeneration or even laser signal generation. Purchasing a stronger pair of single spatial mode fiber coupled pump diodes (the measurement setup was limited to 2 x 125 mW butterfly packaged units due cost constraints) would be the easiest first step required to achieve higher on-chip gain values. In [12] a net gain of 2.0 dB/cm was demonstrated for an amplifier of similar cross-section, an Nd concentration of 2.0 x 10^{20} cm^{-3}, and a background loss of 0.35 dB/cm. The on-chip pump power was almost twice as much as that shown in Figure 5.7 though (45 mW in 115 vs. 25 mW in this work).

5.5 Summary and Conclusions

This chapter opened by introducing the conceptual framework for the design and cross-sectional implementation of novel optically-pumped gain blocks within both the telecommunications O- and C-bands that leverage previous work within an ultra-low loss Si_3N_4-core waveguide platform for lateral mode confinement. An overview of the fabrication process for such on-chip rare-earth-ion-doped waveguide amplifiers was then presented, with a more detailed process traveler made available in Appendix 1. Finally, each structure was tested and quantified for performance. Optical gain of less than 0.5 dB/cm for the $Al_2O_3:Nd^{3+}$ O-band waveguide amplifier under 808 nm pump excitation and optical gain greater than 1.5 dB/cm for the $Al_2O_3:Er^{3+}$ C-band waveguide amplifier under 980 nm pump excitation was demonstrated.

5.6 References

[1] E. H. Bernhardi, H. A. G. M. van Wolferen, K. Wörhoff, R. M. de Ridder, and M. Pollnau, "Highly efficient, low-threshold monolithic distributed-Bragg-reflector channel waveguide laser in Al_2O_3:Yb^{3+}," Opt. Lett.36, 603-605 (2011).

[2] D. Ding, L. M. C. Pereira, J. F. Bauters, M. J. R. Heck, G. Welker, A. Vantomme, J. E. Bowers, M. J. A. de Dood, and D. Bouwmeester, "Multidimensional Purcell effect in an ytterbium-doped ring resonator," Nat. Photon. 10, 385-388 (2016).

[3] N. Li, Purnawirman, Z. Su, E. S. Magden, P. T. Callahan, K. Shtyrkova, M. Xin, A. Ruocco, C. Baiocco, E. P. Ippen, F. X. Kärtner, J. D. B. Bradley, D. Vermeulen, and M. R. Watts, "High-power thulium lasers on a silicon photonics platform," Opt. Lett. 42, 1181-1184 (2017).

[4] J. Bradley, L. Agazzi, D. Geskus, F. Ay, K. Wörhoff, and M. Pollnau, "Gain bandwidth of 80 nm and 2 dB/cm peak gain in Al_2O_3:Er^{3+} optical amplifiers on silicon," J. Opt. Soc. Am. B **27**(2), 187-196 (2010).

[5] M. Belt and D. J. Blumenthal, "High Temperature Operation of an Integrated Erbium-Doped DBR Laser on an Ultra-Low-Loss Si_3N_4 Platform," in *Optical Fiber Communication Conference*, OSA Technical Digest (online) (Optical Society of America, 2015), paper Tu2C.7.

[6] K. Wörhoff, J. D. B. Bradley, F. Ay, D. Geskus, T. P. Blauwendraat, and M. Pollnau, "Reliable low-cost fabrication of low-loss Al_2O_3:Er^{3+} waveguides with 5.4-dB optical gain," IEEE J. Quantum Electron. 45(5), 454-461 (2009).

[7] J. D. B. Bradley, M. C. Silva, M. Gay, L. Bramerie, A. Driessen, K. Wörhoff, J.-C. Simon, and M. Pollnau, "170 Gbit/s transmission in an erbium-doped waveguide amplifier on silicon," Opt. Express 17, 22201-22208 (2009).

[8] X. Zou and T. Izumitani, “Spectroscopic properties and mechanisms of excited state absorption and energy transfer upconversion for Er3+-doped glasses”, Journal of Non-Crystalline Solids 162, 68 (1993).

[9] E. H. Bernhardi, “Bragg-Grating-Based Rare-Earth-Ion-Doped Channel Waveguide Lasers and Their Applications,” Ph.D. Dissertation (Department of Electrical Engineering, Mathematics, and Computer Science, University of Twente, 2012).

[10] M. Pollnau, P. J. Hardman, W. A. Clarkson, and D. C. Hanna, “Upconversion, lifetime quenching, and ground-state bleaching in Nd3+:LiYF4”, Opt. Commun., vol. 147, pp. 203-211, 1998.

[11] M. Pollnau, P. J. Hardman, M. A. Kern, W. A. Clarkson, and D. C. Hanna, “Upconversion-induced heat generation and thermal lensing in Nd:YLF and Nd:YAG”, Phys. Rev. B, vol. 58, pp. 16076-16092, 1998.

[12] J. Yang, “Neodymium-doped Waveguide Amplifiers and Lasers for Integrated Optical Applications,” Ph.D. Dissertation (Department of Electrical Engineering, Mathematics, and Computer Science, University of Twente, 2010).

[13] L. Agazzi, “Spectroscopic Excitation and Quenching Processes in Rare-Earth-Ion-Doped Al_2O_3 and Their Impact on Amplifier and Laser Performance, Ph.D. Dissertation (Department of Electrical Engineering, Mathematics, and Computer Science, University of Twente, 2012).

[14] L. Agazzi, K. Wörhoff, and M. Pollnau, “Energy-transfer-upconversion models, their applicability and breakdown in the presence of spectroscopically distinct ion classes: A case study in amorphous Al2O3:Er3+,” J. Phys. Chem. C 117(13), 6759–6776 (2013).

[15] S. A. Vázquez-Córdova, M. Dijkstra, E. H. Bernhardi, F. Ay, K. Wörhoff, J. L. Herek, S. M. García-Blanco, and M. Pollnau, "Erbium-doped spiral amplifiers with 20 dB of net gain on silicon," Opt. Express 22, 25993-26004 (2014).

[16] L. Agazzi, K. Wörhoff, A. Kahn, M. Fechner, G. Huber, and M. Pollnau, "Spectroscopy of upper energy levels in an Er^{3+}-doped amorphous oxide," J. Opt. Soc. Am. B 30, 663-677 (2013).

[17] J. Bradley, “$Al_2O_3:Er^{3+}$ as a Gain Platform for Integrated Optics,” Ph.D. Dissertation (Department of Electrical Engineering, Mathematics, and Computer Science, University of Twente, 2010).

[18] C. Strohhofer and A. Polman, “Absorption and emission spectroscopy in Er^{3+}-Yb^{3+} doped aluminum oxide waveguides,” Optical Materials, 21 705-712 (2003).

[19] D. Geskus, S. Aravazhi, S. M. García-Blanco, and M. Pollnau, “Giant Optical Gain in a Rare-Earth-Ion-Doped Microstructure,” Adv. Mater. 24, OP19–OP22 (2012).

[20] S. F. Li, C. L. Song, Q. J. Xiong, and B. Ran, “A numerical analysis of gain characteristics of Er-doped Al2O3 waveguide amplifiers,” Opt. Quantum Electron. 34, 859–866 (2002).

[21] J. F. Bauters, M. J. R. Heck, D. D. John, J. S. Barton, C. M. Bruinink, A. Leinse, R. G. Heideman, D. J. Blumenthal, and J. E. Bowers, "Planar waveguides with less than 0.1 dB/m propagation loss fabricated with wafer bonding," Opt. Express 19, 24090-24101 (2011).

Chapter 6

Rare-Earth-Ion-Doped Dielectric Lasers

Low cost, high performance laser integration technologies that establish power efficient, temperature stable, and large scale multiwavelength on-chip arrays are critical for a variety of important applications including coherent optical communications, integrated analog photonics, microwave signal generation, and high spectral resolution light detection and ranging (LIDAR). Integrated waveguide lasers are of particular importance for the realization of compact, rigid, and robust optical devices, since the entire laser cavity along with the optical feedback elements can be fabricated on the same substrate.

When compared to rare-earth-ion-doped dielectric materials, semiconductor gain media exhibit relatively wide lasing linewidths, high amplifier noise figures, and low temperature stability. Since rare-earth-ion-doped dielectric materials do not exhibit an amplitude-phase coupling mechanism as large as that observed in semiconductor lasers, these materials can be used to realize linewidth values that would otherwise be unobtainable with standard semiconductor designs. Furthermore, the high gain in semiconductor lasers makes it difficult to maintain single-longitudinal-mode operation for Bragg-grating-based cavities with relatively strong gratings, since the achievable gain in the cavity also supports the operation of higher order longitudinal modes. In rare-earth-ion-doped lasers, however, single longitudinal-mode operation is typically possible even for cavities with strong gratings, which allows high-quality cavities to be demonstrated due to the high grating reflectivity [1].

From an integration perspective, the rare-earth-ion-doped gain layer can be added by way of only a single additional fabrication step on top of the few already required for the entirety of the ULL waveguide platform, as shown in Section 5.3. Overall, this greatly reduces the complexity of the fabrication process when compared to those necessitated by utilizing a semiconductor-based alternative.

6.0 Chapter Synopsis

In this chapter, the waveguide sidewall Bragg gratings detailed in Chapter 4 are integrated together with the rare-earth-ion-doped waveguide amplifiers discussed and characterized in Chapter 5 to create a novel set of high performance distributed feedback and distributed Bragg reflector lasers. The distributed Bragg reflector laser designs exhibit pump-to-signal conversion efficiencies up to 5.2%, lasing thresholds as low as 11 mW of on-chip pump power, and stable output operation even at elevated cavity temperatures of 400 ^{o}C when excited with 980 nm pump light [2][3]. The distributed feedback laser designs exhibit pump-to-signal conversion efficiencies up to 0.77% and lasing thresholds as low as 21 mW of on-chip pump power again when excited with 980 nm pump light [2]. Appendix 2 includes the full MATLAB code block used to design the DBR abd DFB structures presented in this thesis.

6.1 Standard Cavity Configurations

6.1.1 Active Mirror Distributed Bragg Reflector (DBR) Cavities

A distributed Bragg reflector (DBR) cavity can be considered analogous to a standard traditional Fabry-Pérot cavity. However, instead of forming the cavity using two discrete laser mirrors as the passive reflectors, two Bragg gratings, or Bragg reflectors, which are monolithically integrated with the cavity waveguide are used to reflect the light over many grating periods instead. Figure 6.1 gives a schematic overview of such a cavity, with sidewall

Bragg grating mirror features defined using the design and fabrication approach outlined in Chapter 4.

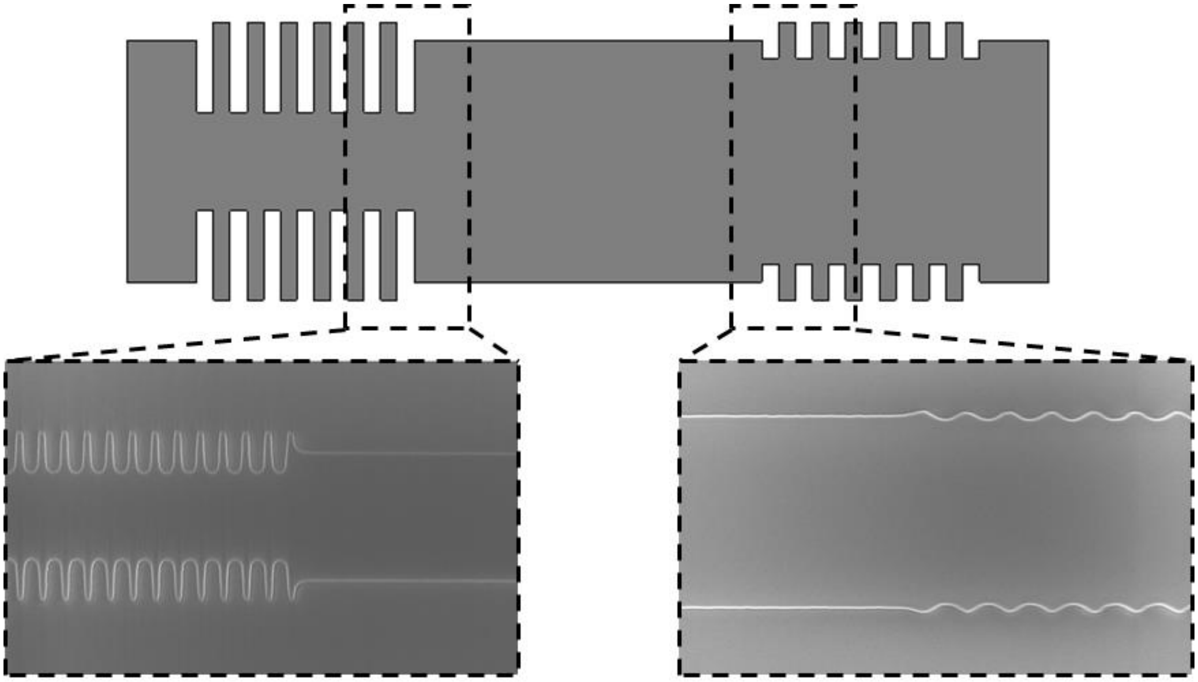

Figure 6.1: *(Top) Distributed Bragg reflector-type laser cavity schematic. The left mirror is of higher grating strength (features higher coupling constant) than the right mirror. Consequently, the majority of light emission will be biased towards the right output. (Bottom Left) SEM micrograph of the transition between high reflectivity sidewall grating section and cavity waveguide. (Bottom Right) SEM micrograph of the transition between cavity waveguide and low reflectivity sidewall grating section. In this work the active material is deposited over the mirror sections as well as the central waveguiding region.*

Consequently, the light in a DBR cavity is reflected in a distributed manner along the length of the Bragg reflectors. A key advantage of such a monolithic DBR structure over a Fabry-Pérot cavity formed by dielectric coatings is that the Bragg gratings in a monolithic DBR cavity provide a much narrower reflection bandwidth as compared to the strong Bragg gratings which are used in dielectric coatings. This makes it more favorable for single-longitudinal-mode lasing operation [1][4]. Such a cavity design also allows for asymmetric reflector strengths on each axial output (as is shown in Figure 6.1), which grants an additional degree of freedom towards overall structural optimization for lasing.

6.1.2 Distributed Feedback (DFB) Cavities

A distributed feedback (DFB) cavity facilitates single frequency lasing of a uniform Bragg grating by introducing a quarter-wavelength phase shift region to the structure [5][6]. Figure 6.2 gives a schematic overview of such a cavity, with sidewall Bragg grating mirror features defined using the design and fabrication approach outlined in Chapter 4.

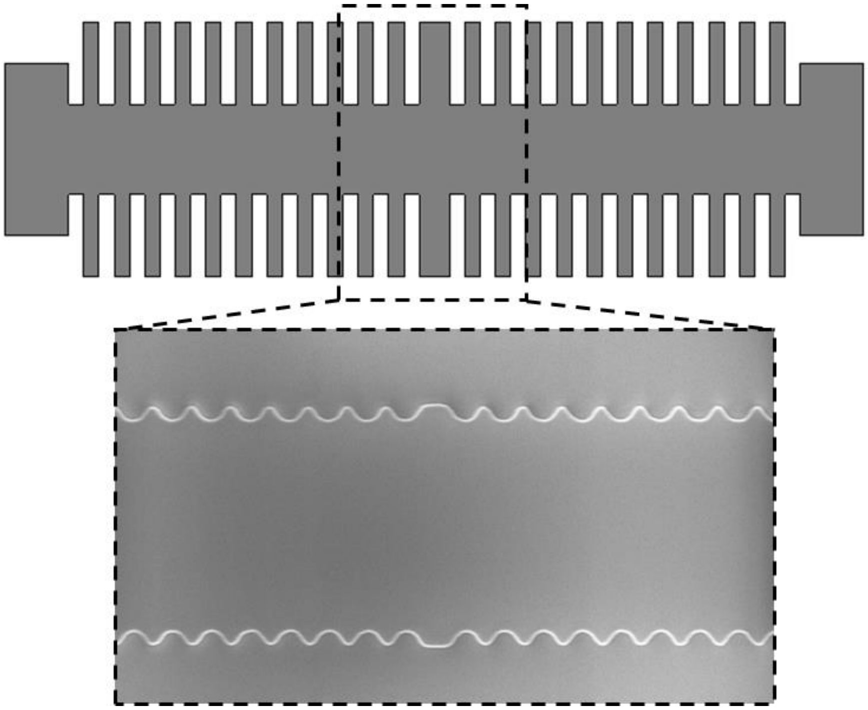

Figure 6.2: *(Top) Distributed feedback-type laser cavity schematic. The central region features an extra grating period that forms the quarter wavelength phase shift section. (Bottom) SEM micrograph of the quarter wavelength phase shift section.*

Throughout the literature there are two different standard methods to realize a quarter-wavelength-shifted Bragg grating. The first is to change the phase of the grating corrugation itself. This requires that half a period of the grating is added or removed somewhere in the center region of the cavity to induce the quarter-wavelength phase shift (as is shown in Figure 6.2). The second method is to induce the phase shift by locally changing the waveguide dimensions, particularly the waveguide width, while the corrugation of the grating remains unaltered [6][7].

6.1.3 Racetrack Ring Resonators

Integrated ring resonators do not require facets or gratings for optical feedback and are thus particularly suited for monolithic integration with other components. The response from coupled ring resonators can be custom designed through leveraging different coupling configurations. In this way, the response from ring resonator cavity filters can be designed to have a flat top and steep roll off [8]. The design of such a structure incorporating a directional coupler and deeply etched tight bend radius sections was described in Section 4.4.

6.2 Device Fabrication Overview

Figure 6.3 gives a graphical representation of the entirety of the waveguide fabrication process, as was similarly presented in Section 4.5. As noted previously, Appendix 1 provides a ‘traveler’ that includes the in-house process steps that follow this diagram. This section will outline the fabrication steps required, with additional details already presented in Section 4.

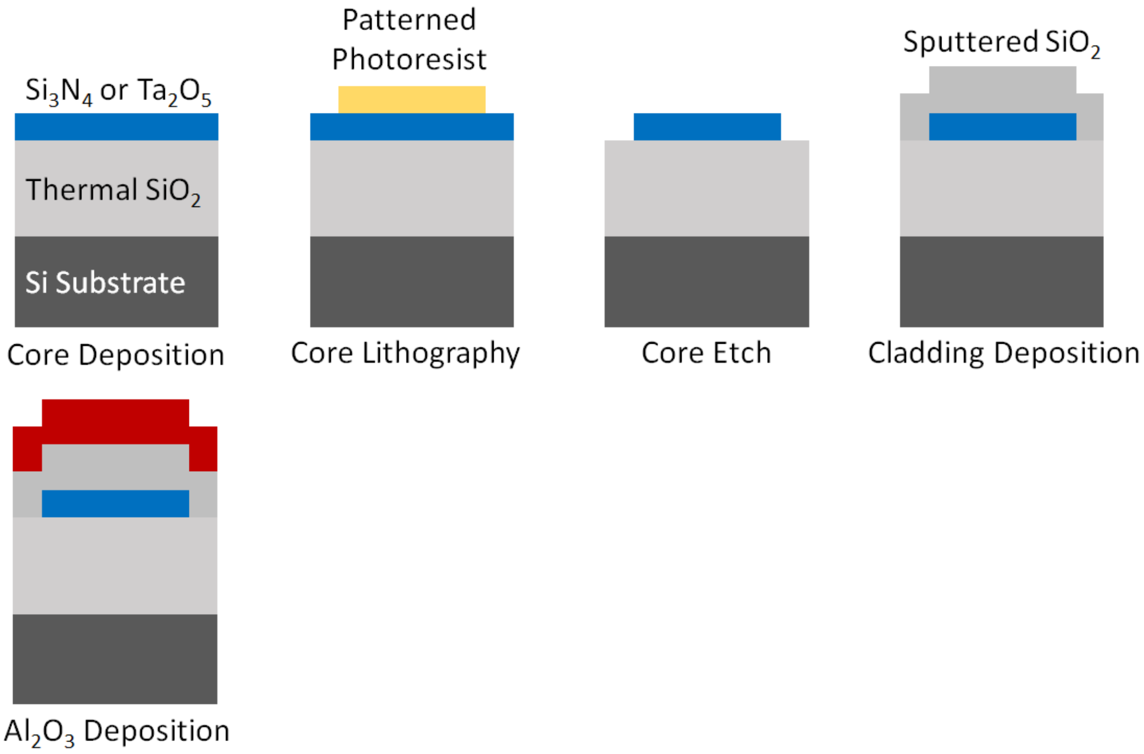

Figure 6.3: *Schematic overview of the fabrication process for the rare-earth-ion-doped waveguided laser designs discussed in Section 6.1. The fabrication process is the same for either DBR or DFB cavities, as the structure is wholly defined by the lithography step.*

Waveguide fabrication begins with either a 500 µm or a 1 mm thick 100 mm diameter silicon substrate upon which 15 microns of silica is thermally grown by wet oxidation for the lower cladding. Next, either the Si_3N_4 waveguide core is deposited by low pressure chemical vapor deposition (LPCVD). This core and grating layer is then patterned using a photoresist mask by 248 nm stepper lithography and an optimized $CH_3/CF_4/O_2$ inductively coupled plasma etch. The etching chamber had $CH_3/CF_4/O_2$ gas flows of 35/5/10 cm^3/min, a pressure of 0.5 Pa, an RF source power of 500 W, and an RF bias of 50 W. The patterning and etch steps are followed by a blanket sputter deposition of the upper SiO_2 cladding. At this stage in the fabrication, the wafer will undergo an anneal protocol of 7 hours long at 1050 ^{o}C in 3.0 SLPM N_2 atmosphere. Following annealing, the rare-earth-ion dopant layer within the Al_2O_3 host material will next be deposited by a reactive co-sputtering process [9]. Finally, the wafer is diced into separate die and a mechanical polishing process conditions the device facets. This process is essential to ensure maximum fiber-to-chip coupling efficiency and waveguide-to-waveguide uniformity.

6.3 Laser Characterization

The experimental setup used to characterize the light/light performance of the on-chip rare-earth-ion-doped waveguide lasers is shown in Figure 6.4. Diode pump light was sent through a 3-paddle polarization controller (PC) and then through a fiber pump/signal multiplexer (980/1550 in the case of Er^{3+} doping). The pump light was then subsequently coupled into the amplifier waveguides by way of a 5 μm spot size, 25 μm working distance lensed fiber. The lasing signal was collected at the chip output and measured through either a rack-mounted optical power meter or an optical spectrum analyzer (OSA).

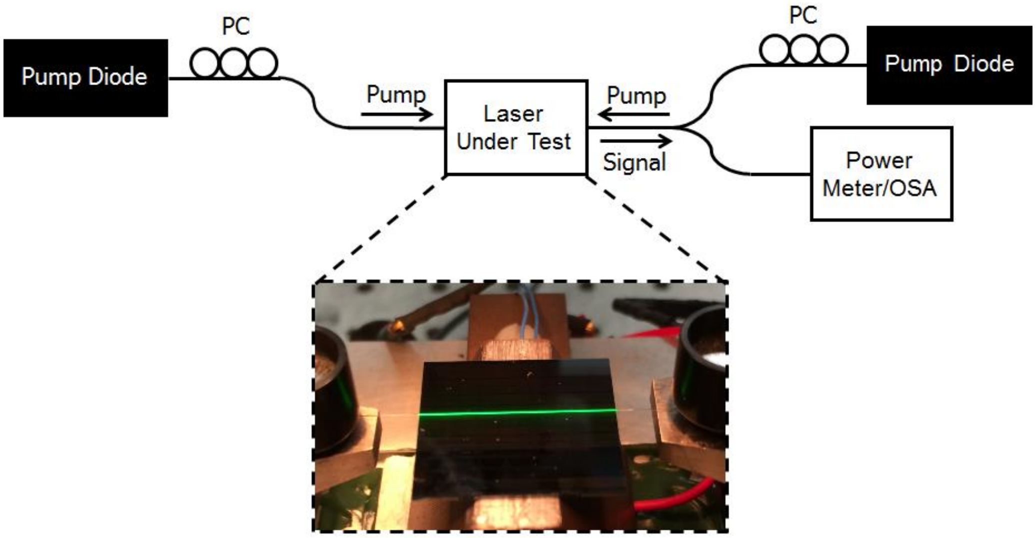

Figure 6.4: *Experimental measurement setup. For these Er*$^{3+}$*-doped lasers the pump diodes output light in the 980 nm wavelength range. The inset shows a top-down view of a laser under test showing detrimental energy transfer upconversion (green emission).*

Elevated temperature measurements were performed by placing the entire laser chip onto a laboratory hot-plate then coupling to the laser waveguides through this same setup configuration.

The experimental setup used to characterize the lasing linewidth performance of the on-chip rare-earth-ion-doped waveguide lasers is shown in Figure 6.5. This setup is based on the well-known self-heterodyne measurement technique [10].

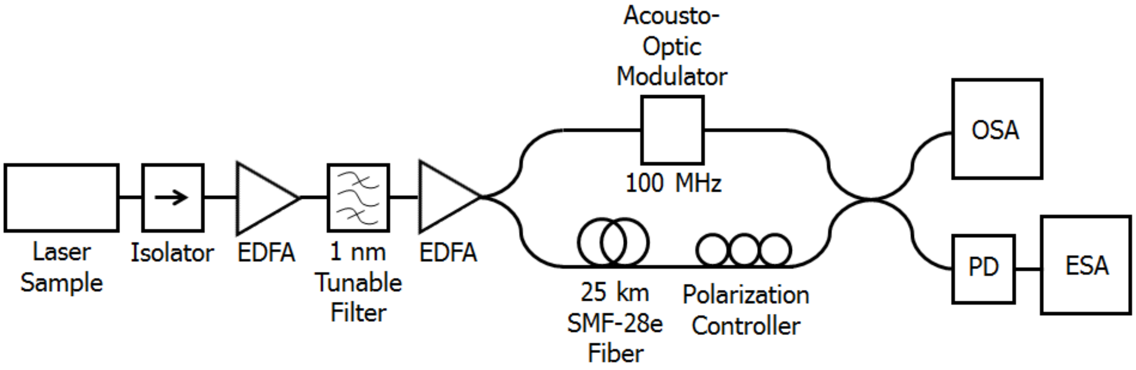

Figure 6.5: *Lasing linewidth self-heterodyne experimental measurement setup. Both erbium-doped fiber amplifiers (EDFAs) are only used in the case of extremely low measured output power. The electrical bandwidth of the photodiode (PD) connected to the electrical spectrum analyzer (ESA) was 5 GHz. The 25 km fiber delay gives a minimum measurable lasing linewidth of 8.5 kHz.*

In a self-heterodyne detection system, the differential delay Δt is an important parameter. If the differential delay is much longer than the coherence time of the optical signal ($\Delta t >> t_{coh}$), the Mach-zehnder interferometer is said to operate in the incoherent regime. Otherwise, if $\Delta t << t_{coh}$, the interferometer will be in the coherent regime. Specifically, the self-heterodyne linewidth measurement technique operates in the incoherent regime. In the incoherent interference regime, optical signals pass through the two interferometer branches and then combine incoherently at the second directional coupler. In this case, the two terms are not correlated with each other because the differential phase term is not deterministic, which resembles the mixing between lights from two independent laser sources with identical spectral linewidth. The acousto-optic modulator in the non-delayed arm is used to shift the resulting center frequency of the beat note between the two arms away from the noisy baseband on the electrical spectrum analyzer (ESA). Because the resulting electrical output tone contains the noise of the frequency shifted and delayed versions of the optical lasing signal, the measured resulting electrical full-width at half-max (FWHM) (3 dB down from the peak) is twice as wide as the original laser linewidth.

6.3.1 Active Mirror Distributed Bragg Reflector (DBR) Lasers

The fabricated DBR resonators consist of straight waveguide sections measuring 17 mm long and 2.8 μm wide, with high and low reflectivity mirrors on either end that each measure 1.5 mm long [2]. Figure 6.1 gives a top-down schematic representation of the Si_3N_4 core of the DBR cavity. 250 μm and 1.75 mm long x 2.8 μm wide active straight waveguide sections adjacent to the high and low reflectivity mirrors assured adequate space was available between the sidewall grating and the die facet for the mechanical polishing process. For the DBR designs, the high reflectivity mirrors had alternating widths of 1.8 and 3.8 μm, giving a κ value of 100 cm^{-1}. The set with the best performance had low reflectivity mirrors with alternating widths of 2.4 and 3.2 μm, delivering a κ value of 30 cm^{-1}. The total period length of the sidewall gratings Λ, which sets the lasing wavelength of the devices, was stepped between 478 and 490 nm. This design information, along with measured performance, is tabulated below in Table 6.1. The differences in output power seen between the devices can be attributed to differences in the gain threshold and the maximum small signal gain spectrum of the erbium-doped active layer, as well as the decreasing magnitude of background scattering loss over increasing wavelengths from 1535-1560 nm.

Table 6.1: *Design breakdown for the set of active mirror DBR lasers tested within this section. The cavity length (L) for all designs was 17 mm with the mirror lengths set at 1.5 mm. The κL products for the input and output mirrors were 11.25 and 3.75. The nominal waveguide width*

was 2.8 μm. All devices had polished, uncoated facets. The conversion efficiency specified is the pump (980 nm) to signal conversion efficiency.

Bragg Period (nm)	Lasing Wavelength (nm)	Threshold Power (mW)	Conversion Efficiency (%)
478	1535	38	0.96
480	1541	28	1.4
482	1547	25	2.2
484	1554	23	2.6
486	1560	11	5.2

6.3.1.1 Light/Light and Spectral Performance

Figure 6.6 shows the single-sided lasing output power as a function of pump laser input power for a DBR operating at 1560 nm (grating period of 486 nm). No saturation of the output power is observed, indicating that thermal effects do not yet limit the performance of the laser.

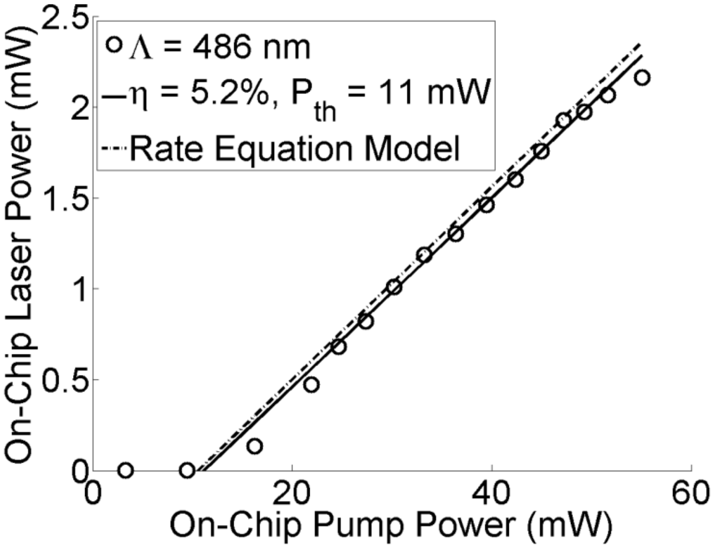

Figure 6.6: *DBR laser power as a function of launched pump power for the device operating at 1546 nm. This measurement was taken at room temperature. The device featured an erbium dopant concentration at 1.3 x 10^{20} cm^{-3}, a nominal waveguide width of 2.8 μm, a cavity length of 17 mm, mirror lengths of 1.5 mm, an input mirror κL product of 11.25 cm^{-1}*, and an output

mirror κL product of 3.75 cm^{-1}. The rate equation model is based on the amplifier dynamics described in Chapter 5 and the T-matrix model developed in Chapter 4. The measured data agrees well with the theoretical performance for the given dopant density and cavity parameters.

The lasing threshold is observed at 11 mW of launched pump power, and a maximum on-chip pump power of 55 mW generates an on-chip laser power of 2.1 mW. This corresponds to a pump-to-signal conversion efficiency (η) of 5.2%. Such a low operating threshold and high slope efficiency is a consequence of the strongly reflecting cavity design, as well as the low propagation loss of the LPCVD Si_3N_4. Figure 6.7 gives the spectra of five different DBR lasers as recorded by the OSA.

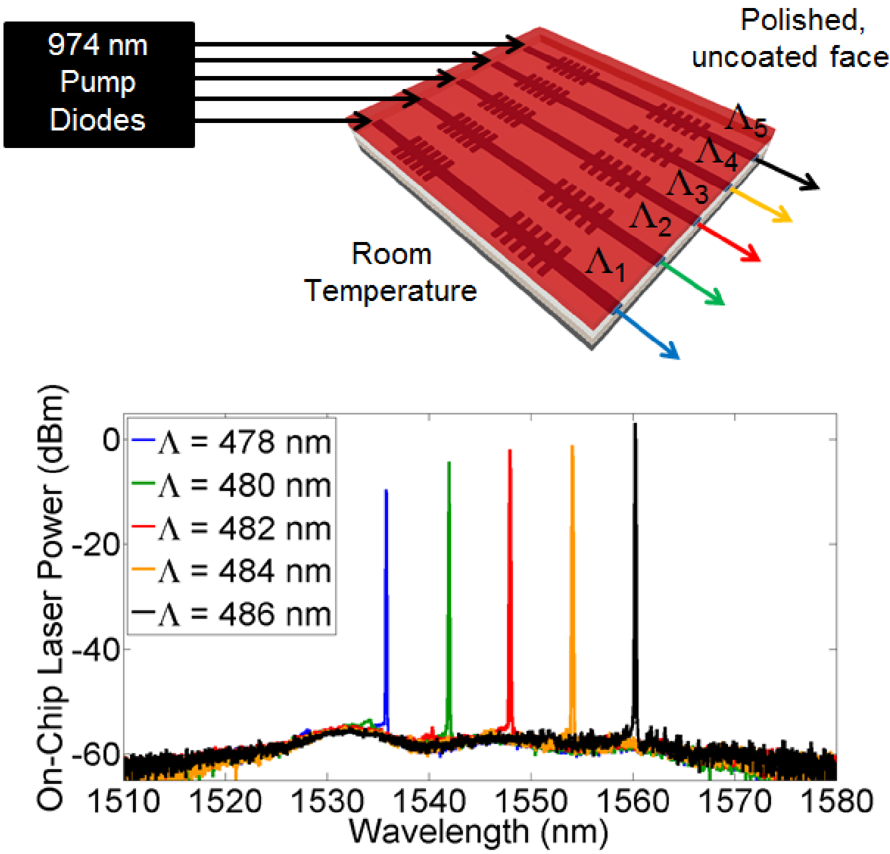

Figure 6.7: *(Top) Schematic testing setup of the active mirror DBR array under test. The nominal waveguide width was 2.8 µm for all devices. The lasers had cavity lengths of 17 mm, mirror lengths of 1.5 mm, input mirror κL products of 11.25 cm^{-1}, and output mirror κL products of 3.75 cm^{-1}. The erbium dopant concentration for all devices was measured as 1.3 x 10^{20} cm^{-3}. (Bot) Superimposed DBR output laser spectra as captured by the OSA.*

A simple modification of the grating period within the Si_3N_4 core layer from 478 to 486 nm causes the lasers to output light at 1535, 1541, 1547, 1554, and 1560 nm wavelengths. As is shown, the side-mode suppression ratio (SMSR) for all devices exceeds 50 dB.

6.3.1.2 Lasing Linewidth

Figure 6.8 gives a series of 100 integrated electrical spectrum analyzer traces for an active mirror DBR operating at 1560 nm (grating period of 486 nm), through use of the experimental setup described in Figure 6.5.

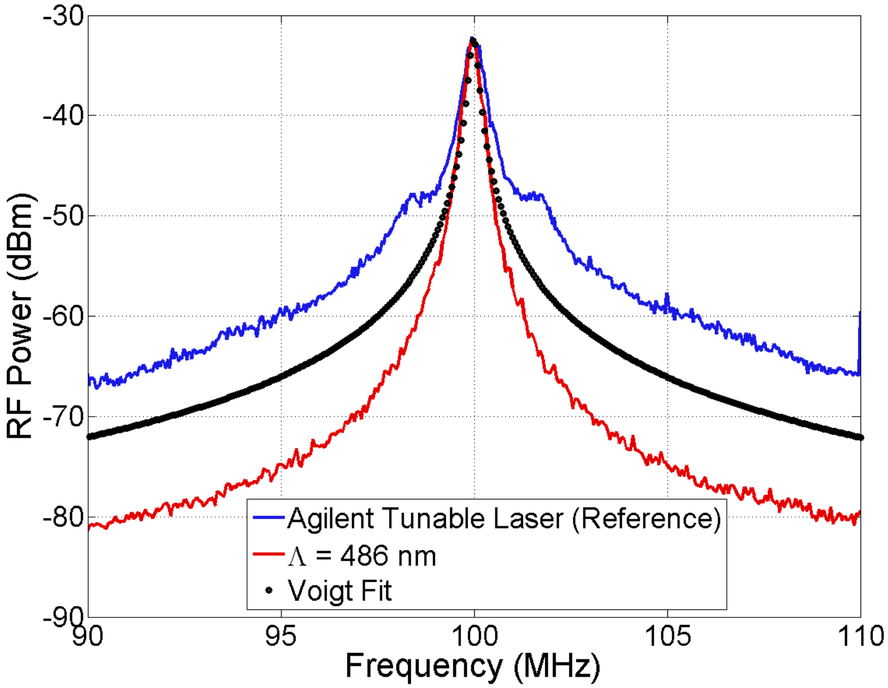

Figure 6.8: *Measured RF power spectrum for the laser operating at 1560 nm. For the measurement, the resolution bandwidth of the ESA was set at 1 kHz and 100 scans were integrated. A commercial external cavity tunable laser purchased from Agilent Technologies (81680A, specified linewidth of 100 kHz) is included for a reference comparison. The resulting Voigt fitting of the linewidth of this device gives a value of 150 kHz.*

The measured resulting full FWHM (3 dB down from the peak) linewidth for this device was 150 kHz. The Voigt fitting shown in Figure 6.8 for the device implies that both Lorentzian (white frequency noise) and Gaussian (1/f noise) components are present within the spectrum [11][12]. Fiber-based versions of similar DBR cavity designs have shown single-digit kHz linewidths [13]. In such fiber-based designs though, the Bragg reflectors that form the cavity mirrors are of a passive material construction, as compared to the active mirrors demonstrated within this thesis. The refractive index change of the mirrors under pump excitation, while small in nature due to the low enhancement factor of the erbium-doped Al_2O_3 material [14], is nonetheless detrimentally affecting the resulting linewidth of the demonstrated device. Development of a low loss (<0.5 dB/transition) and low reflection on-chip active-passive transition section as described in Section 7.4 would alleviate this issue and allow for single-digit lasing linewidths to be realized.

6.3.1.3 Temperature Dependent Performance

Meeting currently forecasted demands for future telecommunications and environmental sensor system design requires optical sources that are not only able to successfully operate at elevated temperatures, but at the same time retain a high degree of wavelength stability while doing so. Figure 6.9 gives a comparison of the light/light performance of a DBR laser from the previous section operating at room temperature and an extreme temperature elevation of 400 ^{o}C.

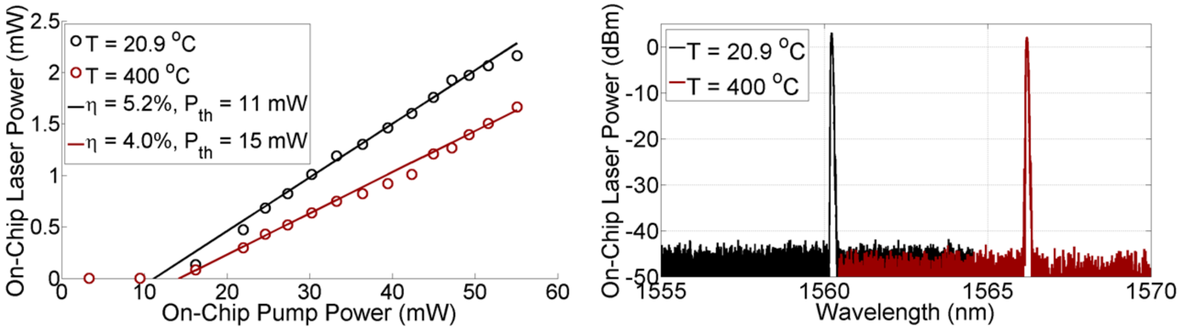

(a) (b)

Figure 6.9: *(a) DBR laser power as a function of launched pump power for the laser operating at two different temperatures. This device is the same as that shown in Figure 6.6. (b) Optical spectrum of the device at the same two previous temperatures.*

With the hotplate adjusted to its maximum operating point of 400 °C the laser emission has decreased by less than 2 dB, and the device is still able to achieve more than 1.5 mW of output power. Here the threshold pump power has increased to 15 mW and the pump-to-signal conversion efficiency (η) has decreased to 4.0%. This minor change in output power over such a wide temperature range is attributed to the choice of pumping the device with 980 nm light, as opposed to 1480 nm light [15]. A finer measurement of the lasing wavelength shift as a function of temperature is shown in Figure 6.10.

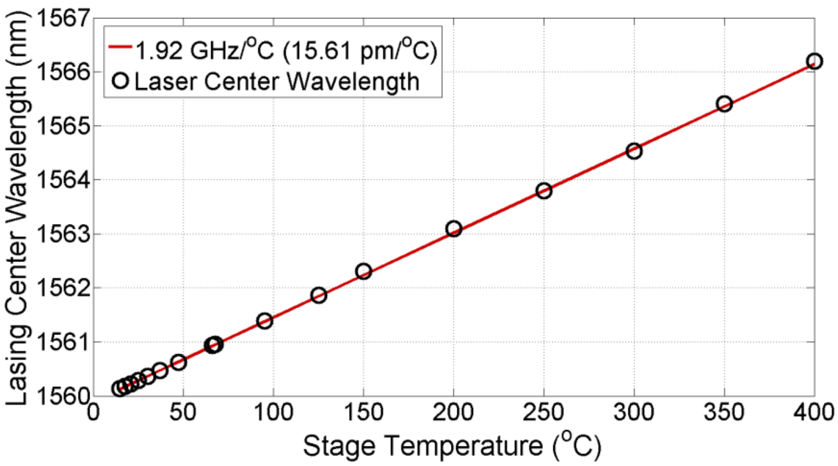

Figure 6.10: *Characterization of the frequency shift of the device across the operating temperature range. This device is the same as that shown in Figure 6.6.*

Here a linear lasing wavelength shift with temperature of 1.92 GHz/°C (15.61 pm/°C) is achieved. This linear shift of operating wavelength with shift in temperature is expected due to the thermal properties of the glass host Al_2O_3 gain medium [16]. The 400 °C result was the limit of the hotplate used in the experimental setup. Typical Bragg grating-based fiber temperature sensors have shown operation in 750+ °C environments, with temperature slopes in the 3.5 GHz/°C range [17][18].

6.3.2 Distributed Feedback (DFB) Lasers

The DFB cavities measure 20.5 mm long with 250 μm long x 2.8 μm wide active input waveguides on either end between the lasing cavity and the die facet [2]. Again, the 250 μm long active waveguides ensure that sufficient distance between the sidewall grating and the facet is available for polishing. Figure 6.2 gives a top-down schematic representation of the Si_3N_4 core of the DFB cavity. For the DFB designs, the set with the best performance had alternating widths of 2.55 and 3.05 μm, which in turn produces a κ value of 16 cm^{-1}. The total period length of the sidewall gratings Λ, which sets the lasing wavelength of the devices, was stepped between 478 and 490 nm. This design information, along with measured performance, is tabulated below in Table 6.2. The differences in output power seen between the devices can be attributed to differences in the gain threshold and the maximum small signal gain spectrum of the erbium-doped active layer.

Table 6.2: *Design breakdown for the set of active mirror DFB lasers tested within this section. The cavity length (L) for all designs was 21.5 mm. The κL products for the cavities were 34.4. The nominal waveguide width was 2.8 μm. All devices had polished, uncoated facets. The conversion efficiency specified is the pump (980 nm) to signal conversion efficiency.*

Bragg Period (nm)	Lasing Wavelength (nm)	Threshold Power (mW)	Conversion Efficiency (%)
478	1534	25	0.67
482	1546	21	0.77
486	1558	20	0.41
490	1570	26	0.53

6.3.2.1 Light/Light and Spectral Performance

Figure 6.11 shows the single-sided lasing output power as a function of pump laser input power for a DFB operating at 1546 nm (grating period of 482 nm). No saturation of the output power is observed, indicating that thermal effects do not yet limit the performance of the laser.

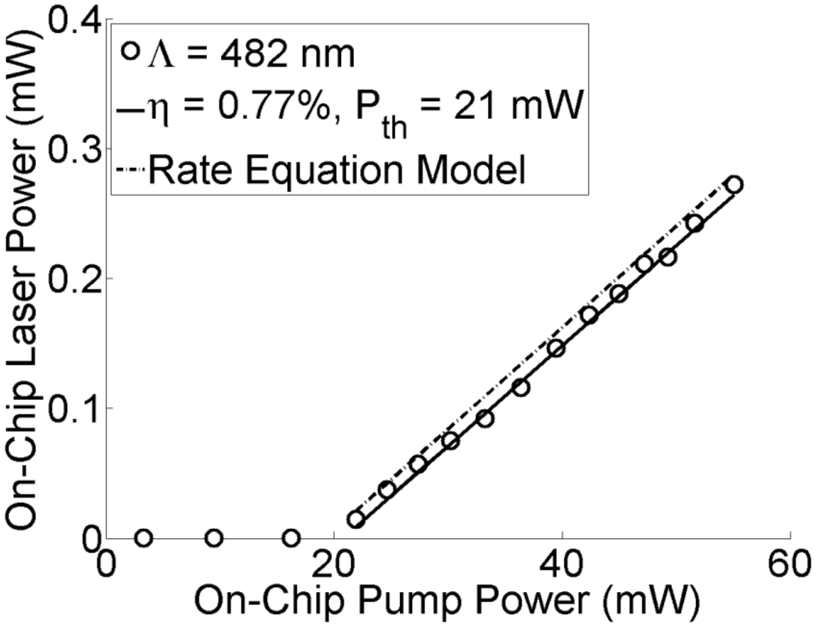

Figure 6.11: *DFB laser power as a function of launched pump power for the device operating at 1560 nm. This measurement was taken at room temperature. The device featured an erbium dopant concentration at 1.3 x* 10^{20} *cm*$^{-3}$*, a nominal waveguide width of 2.8 μm, a cavity length of 21.5 mm, a κL product of 34.4 cm*$^{-1}$*, and a λ/4 section within the center of the cavity length. The rate equation model is based on the amplifier dynamics described in Chapter 5 and the T-matrix model developed in Chapter 4. As was the case for the active mirror DBR, the DFB data measured here agrees well with the theoretical performance for the given dopant density and cavity parameters.*

Here, the lasing threshold is observed at 21 mW of launched pump power, and for a maximum on-chip pump power of 55 mW an on-chip laser power of 0.27 mW is obtained. This corresponds to a pump-to-signal conversion efficiency of 0.77%, which compares favorably to similar designs measured in the literature when pumped by 980 nm light [1]. This is less than that demonstrated by the active mirror DBR design in the previous section due to the extremely high κL product of the device of 34.4. Additionally, the κ of 16 cm^{-1} for the device does induce extraneous scattering loss to the cavity, further degrading the pump-to-signal conversion efficiency. It is also instructive to use the rate equation model shown in Figure 6.11 to plot the optical signal power along the DFB cavity length. This is done in Figure 6.12.

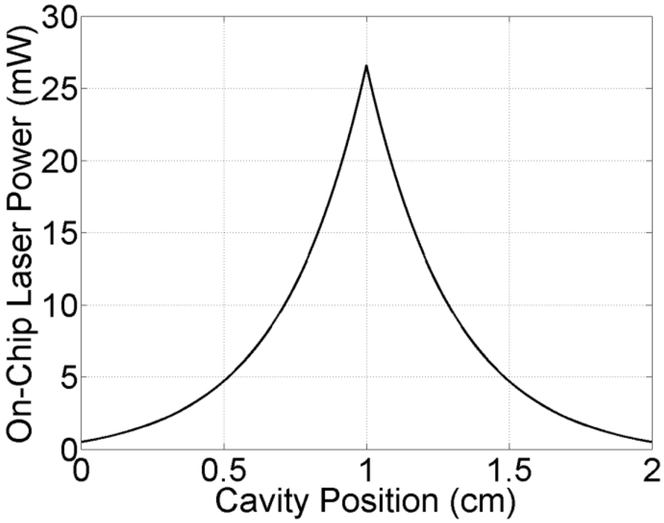

Figure 6.12: *DFB laser power as a function of cavity position for the device operating at 1560 nm with 50 mW of input 980 nm pump power. The peak power is strongly confined within the central λ/4 section, which in turn causes a strong degree of localized spatial hole burning that eventually contributes to broadening of the resulting laser linewidth.*

As is shown, the laser power is strongly confined to the λ/4 phase shift region in the center of the cavity. This will greatly affect the resulting measured linewidth value through spatial hole burning. Figure 6.13 gives the spectra of four different DFB lasers as recorded by the OSA.

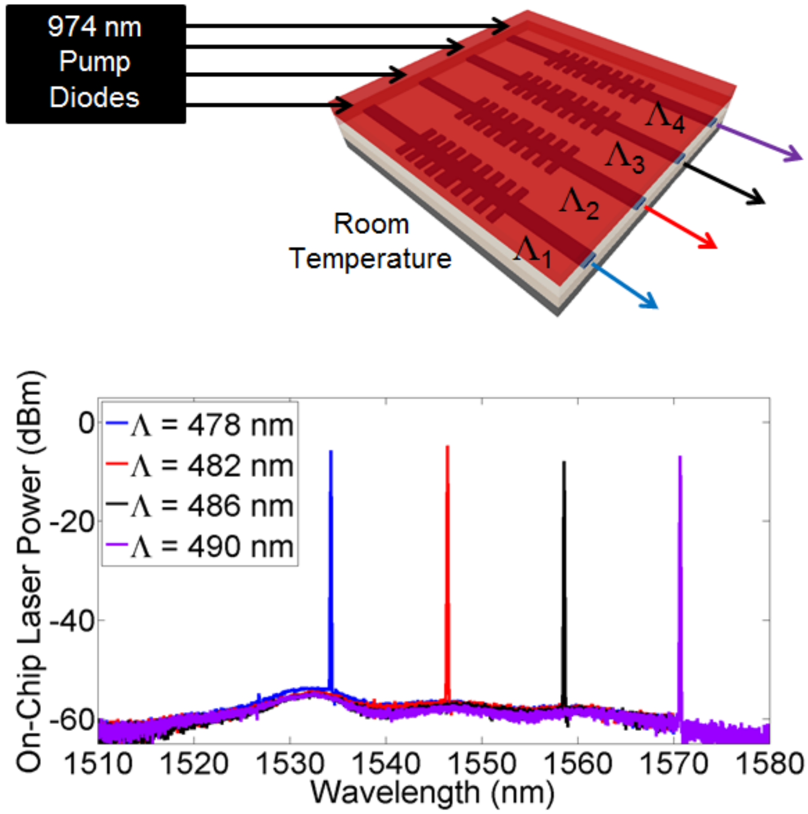

Figure 6.13: *(Top) Schematic testing setup of the DBR array under test. The nominal waveguide width was 2.8 μm for all devices. The lasers had λ/4 sections within the center of the cavity length, physical cavity lengths of 21.5 mm, and κL products of 34.4* cm^{-1}*. The erbium dopant concentration for all devices was measured as* 1.3×10^{20} cm^{-3}*. (Bot) Superimposed DFB output laser spectra as captured by the OSA.*

Here, devices with grating periods between 478 and 490 nm operate at 1534, 1546, 1558, and 1570 nm wavelengths. As was the case for the DBR designs, the SMSR for each of these DFB structures is greater than 50 dB.

6.3.2.2 Lasing Linewidth

Figure 6.14 gives a series of 100 integrated electrical spectrum analyzer traces for a DFB operating at 1546 nm (grating period of 482 nm), through use of the experimental setup described in Figure 6.5.

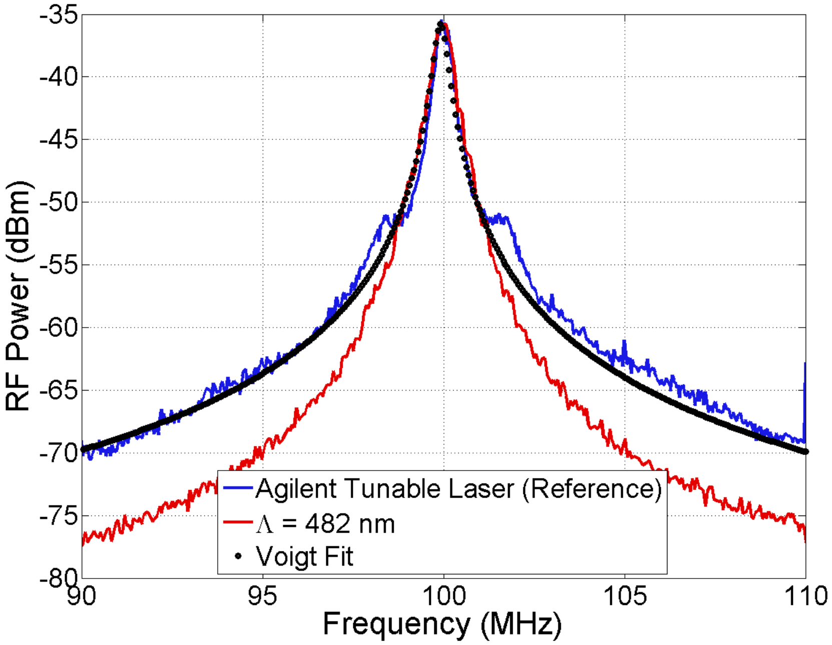

Figure 6.14: *Measured RF power spectrum for the laser operating at 1560 nm. For the measurement, the resolution bandwidth of the ESA was set at 1 kHz and 100 scans were integrated. A commercial external cavity tunable laser purchased from Agilent Technologies (81680A, specified linewidth of 100 kHz) is included for a reference comparison. The resulting Voigt fitting of the linewidth of this device gives a value of 300 kHz.*

The measured resulting full FWHM (3 dB down from the peak) linewidth for this device was 300 kHz. The Voigt fitting shown in Figure 6.8 for the device implies that both Lorentzian (white frequency noise) and Gaussian (1/f noise) components are present within the spectrum [11][12]. Standard semiconductor DFB lasers typically have linewidths that are a few orders of magnitude larger owing to longitudinal spatial hole burning when carriers are depleted by the nonuniform photon distribution [19].

6.4 Summary and Conclusions

This chapter detailed the design, fabrication, and measurement of a series of distributed Bragg reflector and distributed feedback lasers that utilized the sidewall Bragg gratings detailed in Chapter 4 integrated together with the rare-earth-ion-doped waveguide amplifiers discussed and characterized in Chapter 5. The distributed Bragg reflector laser designs exhibit lasing thresholds as low as 11 mW of on-chip pump power, pump-to-signal conversion efficiencies up to 5.2%, and stable output operation even at elevated cavity temperatures of 400 ^{o}C. The distributed feedback laser designs exhibit lasing thresholds as low as 21 mW of on-chip pump power and pump-to-signal conversion efficiencies up to 0.77%, all when excited with 980 nm pump light.

In the future, pumping the devices with 1480 nm instead of 980 nm light would be the best avenue to show immediate improvements in device performance. This would come with an increase in total cost though, as the price per watt is less for 980 nm laser diodes than for 1480 nm diodes. It is this cost constraint that drove the use of a 980 nm pump laser for this work. Another potential avenue for advancement would be to incorporate ytterbium (Yb) atoms within the Al_2O_3 host material as a sensitizing agent. Such a technique may only make a small improvement though, as efficient energy transfer between the Yb and Er atoms in analogous devices has thus far been limited to host glasses with high phosphorus content [20].

6.5 References

[1] E. H. Bernhardi, “Bragg-Grating-Based Rare-Earth-Ion-Doped Channel Waveguide Lasers and Their Applications,” Ph.D. Dissertation (Department of Electrical Engineering, Mathematics, and Computer Science, University of Twente, 2012).

[2] M. Belt and D. J. Blumenthal, "Erbium-doped waveguide DBR and DFB laser arrays integrated within an ultra-low-loss Si_3N_4 platform," Opt. Express 22, 10655-10660 (2014).

[3] M. Belt and D. J. Blumenthal. "High temperature operation of an integrated erbium-doped DBR laser on an ultra-low-loss Si3 N4 platform." *Optical Fiber Communications Conference and Exhibition (OFC), 2015*. IEEE, 2015.

[4] L. A. Coldren, S. W. Corzine, and M. L. Mašanović, Diode Lasers and Photonic Integrated Circuits (Wiley, 2012), Chap. 3.

[5] H. A. Haus and C. V. Shank, “Antisymmetric taper of distributed feedback lasers”, IEEE Journal of Quantum Electronics QE-12, 532 (1976).

[6] K. Tada, “Proposal of a distributed feedback laser with nonuniform stripe width for complete single-mode oscillation”, Microelectronic Engineering 2, 157 (1984).

[7] E. H. Bernhardi, H. A.G.M. van Wolferen, L. Agazzi, M. R.H. Khan, C. G.H. Roeloffzen, K. Wörhoff, M. Pollnau, and R. M. de Ridder, "Ultra-narrow-linewidth, single-frequency distributed feedback waveguide laser in $Al_2O_3:Er^{3+}$on silicon," Opt. Lett. 35, 2394-2396 (2010).

[8] D. G. Rabus, Integrated Ring Resonators: The Compendium (Springer, 2007), Chap. 1.

[9] K. Wörhoff, J. D. B. Bradley, F. Ay, D. Geskus, T. P. Blauwendraat, and M. Pollnau, "Reliable low-cost fabrication of low-loss $Al_2O_3:Er^{3+}$ waveguides with 5.4-dB optical gain," IEEE J. Quantum Electron. 45(5), 454-461 (2009).

[10] R. Hui and M. O'Sullivan, Fiber Optic Measurement Techniques (Elsevier, 2009), Chap. 3.

[11] L. B. Mercer, "1/f frequency noise effects on self-heterodyne linewidth measurements," J. Lightwave Technol. 9, 485-493 (1991).

[12] X. Chen, M. Han, Y. Zhu, B. Dong, and A. Wong, "Implementation of a loss-compensated recirculating delayed self-heterodyne interferometer for ultranarrow laser linewidth measurement," Appl. Opt. 45, 7712-7717 (2006).

[13] J. Geng, C. Spiegelberg, Y. Hu, Y. Kaneda, S. Jiang, and N. Peyghambarian, "Low noise narrow linewidth fiber laser at 1550 nm," J. Lightwave Technol. 22, 57– 62 (2004).

[14] C. Henry, "Theory of the linewidth of semiconductor lasers," IEEE J. Quantum Electron., vol. 18, no. 2, pp. 259–264, Feb. 1982.

[15] N. Kagi, A. Oyobe, and K. Nakamura, "Temperature Dependence of the Gain in Erbium-Doped Fibers," J. of Lightwave Tech. **9**(2), 261-265 (1991).

[16] S. Wiechman and J. Müller, "Thermo-optic properties of TiO2, Ta2O5, and Al2O3 thin films for integrated optics on silicon," Thin Solid Films 517, 6847-6849 (2009).

[17] B. Zhang and M. Kahrizi, "High-Temperature Resistance Fiber Bragg Grating Temperature Sensor Fabrication," IEEE Sens. Journ. 7(4), 586-591 (2007).

[18] D. Grobnic, S. J. Mihailov, C. W. Smelser, and H. Ding, "Sapphire Fiber Bragg Grating Sensor Made Using Femtosecond Laser Radiation for Ultrahigh Temperature Applications," IEEE Photon. Tech. Lett. 16(11), 2505-2507 (2004).

[19] T. Kunii and Y. Matsui, “Narrow spectral linewidth semiconductor lasers”, Optical and Quantum Electronics 24, 719 (1992).

[20] J. Hoyo, V. Berdejo, T. Toney Fernandez, A. Ferrer, A. Ruiz, J. A. Valles, M. A. Rebolledo, I. Ortega-Feliu, and J. Solis, “Femtosecond laser written 16.5 mm long glass-waveguide amplifier and laser with 5.2 dB cm−1 internal gain at 1534 nm,” Laser Phys. Lett. 10(10), 105802 (2013).

Chapter 7

Summary and Future Directions

7.1 Summary

The purpose of this thesis was to explore the possibilities of monolithic integration and on-chip component development to create optically pumped laser light sources on an ultra-low loss glass-based waveguide platform. The result of this endeavor is a new class of on-chip rare-earth-ion-doped laser that when compared to semiconductor-based alternative shows lower output noise within standard cavity configurations (as demonstrated by the lasing linewidth), operation over extreme temperature ranges (up to a measurement setup limited 400 ^{o}C), and a straightforward fabrication procedure that is amenable to high volume modern CMOS processes. On route to this final goal, the separate constituent parts required for the completed lasing cavities were designed, fabricated, and demonstrated to have outstanding properties of their own. This includes passive record low propagation loss Ta_2O_5-core based weekly guiding buried ridge waveguides, strongly guiding deeply etched ridge waveguides that exploit a Ti-based hard-mask process for reduction in etch roughness, waveguide sidewall grating filters that allow for a design-by-lithography approach, and active on-chip rare-earth-ion-doped waveguide amplifiers to impart optical gain to a signal in either the telecommunications O-band or C-band.

In Chapter 1, the motivation for and conceptual overview of the integration platform was presented, including notes on how the need for high speed optical interconnects is driving further integration and how ultra-low loss waveguides can increase performance in this and other applications. Chapters 2 and 3 provide background research related to the material and structural considerations of designing and fabricating modern integration platforms and the active and passive building blocks developed within this thesis, respectively. Chapter 4 covers the full analysis, design, fabrication, and characterization of a variety of passive Si_3N_4-core and Ta_2O_5-core waveguide components. Chapters 5 and 6 continue by extending this fully encompassing accounting to active waveguide amplifiers and laser cavities based on a rare-earth-ion-doped dielectric host material. Finally, in this chapter, a discussion of some of the future directions for related work closes out this thesis.

7.2 Future Work

Future work related to the components and devices within this thesis can lead in two major different directions, with the first being towards improving the existing demonstrated device performance and the second leading towards more advanced photonic integration allowing for even higher level functionality.

7.2.1 Linear Cavity Laser Performance - Linewidth Narrowing: Distributed Phase Shift Cavity

Further optimization of the output noise properties of the linear distributed feedback lasing cavities demonstrated in Chapter 6 can be undertaken through a distributed, rather discrete, phase shift region as in [1]. Here the phase shift region, rather than being a discrete λ/4 distance long, was implemented by means of an adiabatic sinusoidal tapering of the waveguide width in the center region of the cavity. The same can be accomplished within the design paradigm described within this thesis by apodizing the waveguide sidewall Bragg gratings that define the lasing cavities. A series of 20.5 mm long lasing cavities with 2 mm long centrally located distributed phase shift sections of various sinh profile apodization strengths was fabricated and tested, with their device geometry, transmission, reflection, and output power characteristics shown in Figure 7.1, Figure 7.2, and Figure 7.3.

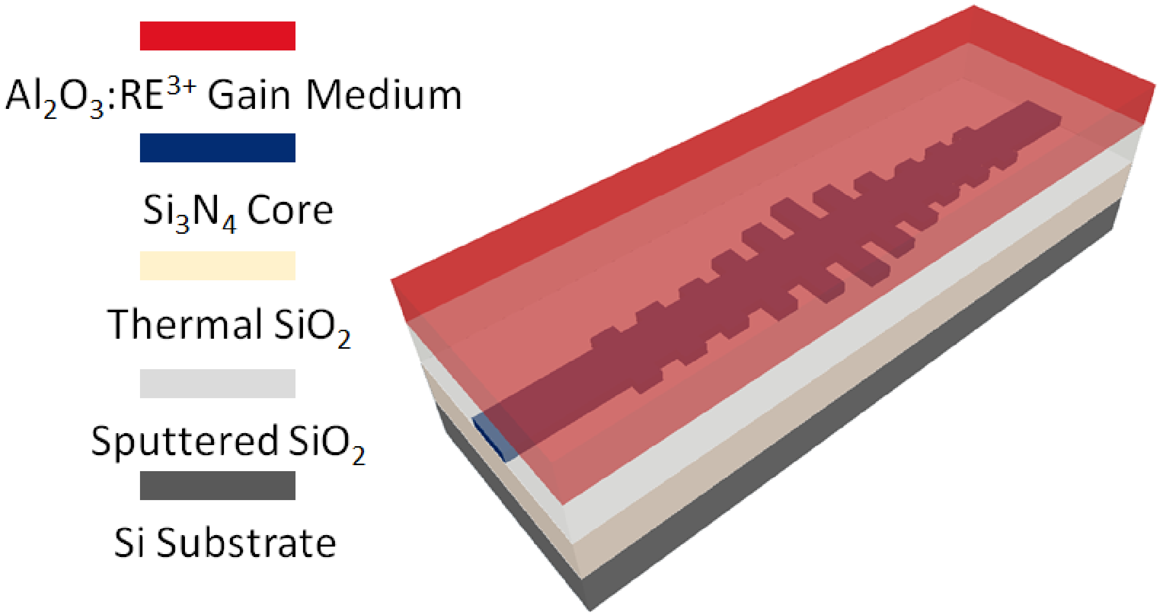

Figure 7.1: *Three-dimensional graphic of a waveguide-based rare-earth-ion-doped distributed feedback reflector laser cavity. The device featured an erbium dopant concentration at 1.3 x* 10^{20} *cm*$^{-3}$*, a nominal waveguide width of 2.8 µm, a cavity length of 21.5 mm, and a κL product of 34.4 cm*$^{-1}$*. The 2 mm long distributed phase shift section is visible in the central region of the device.*

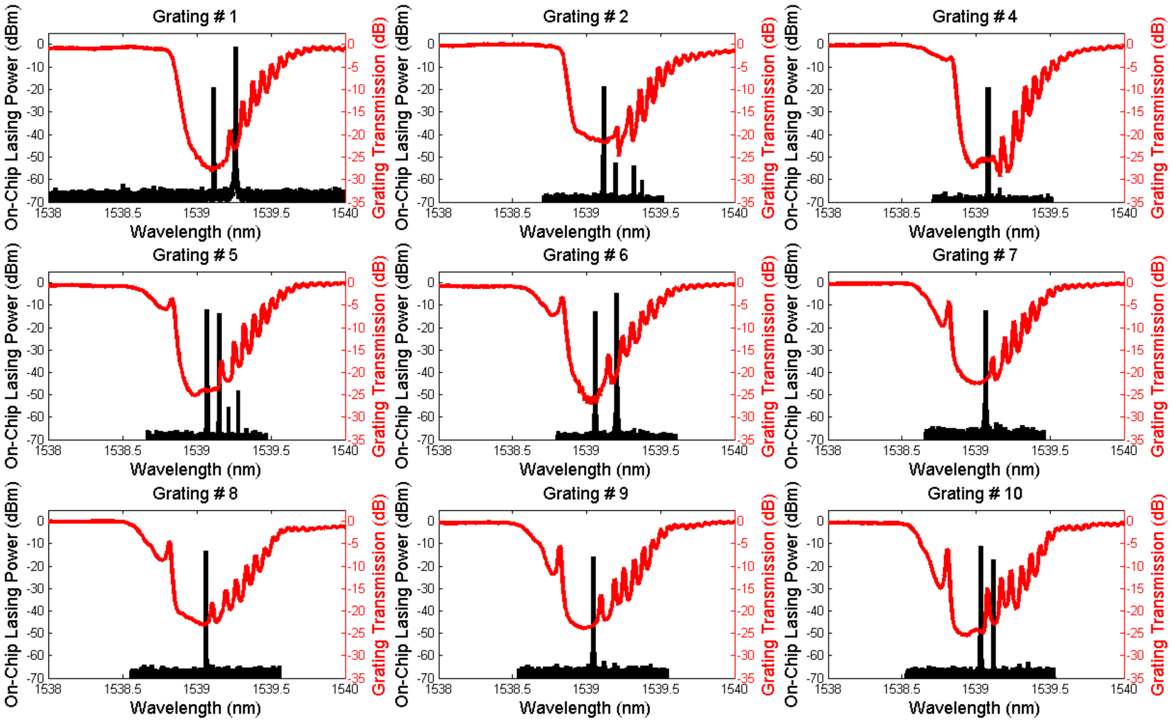

Figure 7.2: *Cold-cavity transmission response (red) and on-chip lasing spectra (black) for a variety of tested distributed phase shift distributed feedback laser cavities. The lasing spectra were measured with a high resolution OSA with a 20 MHz resolution.*

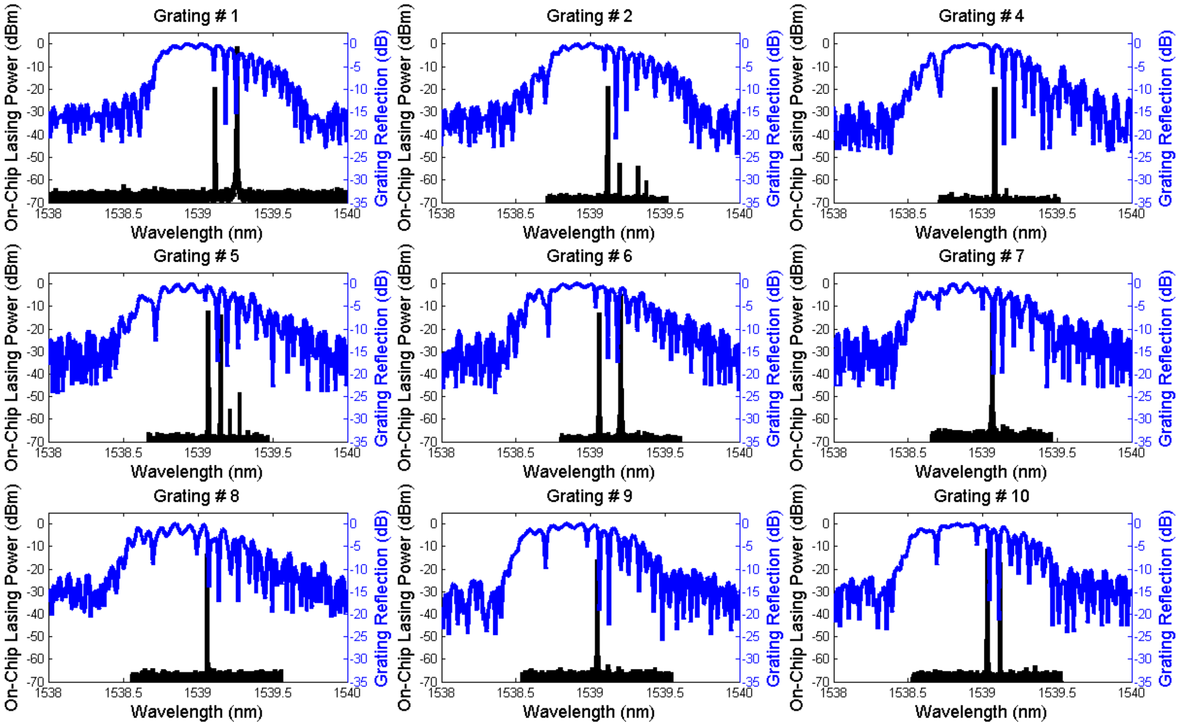

Figure 7.3: *Cold-cavity reflection response (blue) and on-chip lasing spectra (black) for a variety of tested distributed phase shift distributed feedback laser cavities. The lasing spectra were measured with a high resolution OSA with a 20 MHz resolution.*

As is shown, some designs exhibit multi-mode output while others stay strictly single mode due to the disparity of the induced phase shift of their central apodized region. Further testing and design in this area is required, but through this approach single-digit kHz lasing linewidths are absolutely feasible.

7.2.2 Linear Cavity Laser Performance - Power Efficiency

Such linear lasing cavities as demonstrated within Chapter 6 still have a significant amount of optical pump light that passes through the cavity un-absorbed. There exist two main design solutions that would harness this ‘lost’ optical pump power and, in the process, improve overall pump-to-signal lasing efficiency. They involve either incorporating a third reflector into the cavity design to make use of more pump light from a single-sided pumping configuration or increasing the cavity length to allow for more total pump absorption.

7.2.2.1 Optical Pump Reflector

As is shown schematically in Figure 7.4, an integrated sidewall grating filter for the pump light can be integrated with the lasing cavity along the output waveguide.

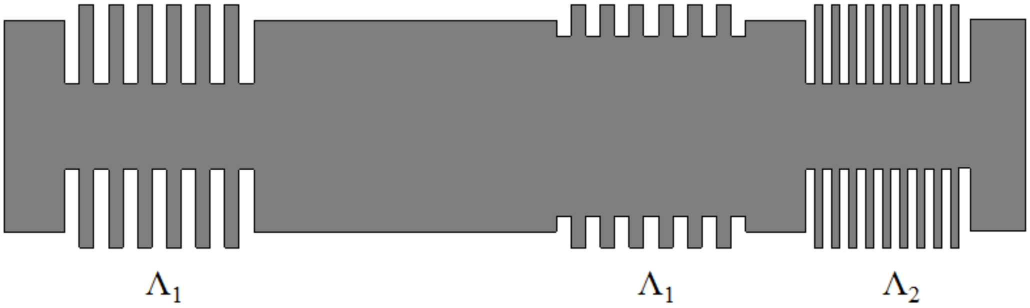

Figure 7.4: *Top-down schematic of a possible double-pass optical gain DBR structure.* Λ_1 *and* Λ_2 *denote the Bragg period for the signal and pump light, respectively.*

Such a filter would not only allow for double-pass optical gain, but also stop the unabsorbed pump light from interfering with subsequent system components down the line. Initial fabrication experiments targeting this design showed an in-house lithography limitation though, as the grating period for the pump light (labeled Λ_2 in Figure 7.4) is near the absolute minimum realizable by UCSB's ASML 248 nm stepper system. Figure 7.5 gives an SEM image of a device exhibiting a standard failure mode for such lithography.

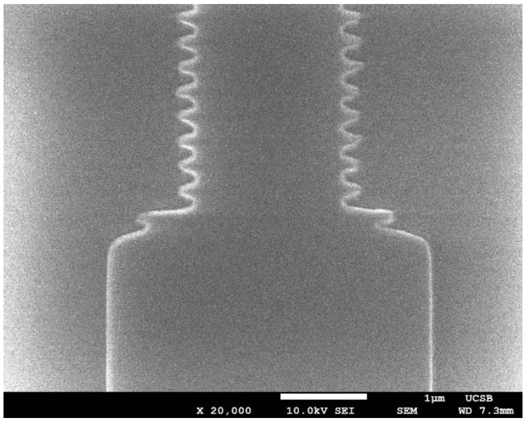

Figure 7.5: *SEM image of an 80 nm etched* Si_3N_4 *core with a transition between a straight waveguide and a waveguide sidewall Bragg grating designed to reflect 980 nm pump light. Due to the resolution limit of the in-house 248 nm stepper system, the teeth sections are completely unresolved.*

Modern CMOS foundries, which feature 193 nm immersion lithography steppers, would not encounter issues such as that demonstrated due to their lower operating wavelength, and hence higher achievable resolution. This technique was recently demonstrated within the literature showing favorable results [2].

7.2.2.2 Waveguide Spiral Cavity

As was detailed in Chapter 5, the relatively low absorption cross section of a rare-earth-ion dopant-based gain medium compared to a semiconductor gain medium is significantly reduced. This leads to a large disparity in overall device lengths (take a standard millimeter-long semiconductor optical amplifier vs. a meter-long erbium-doped fiber as an illustrative example). Therefore, increasing the 2.1 cm long amplifiers and lasers demonstrated in Chapters 5 and 6 to the meter length scales by way of leveraging the low background propagation loss of the ultra-low-loss waveguide platform is a natural next step. Fabricating the waveguides into a spiral shape when doing so will minimize the overall device footprint to save area. A waveguide amplifier in this configuration was recently demonstrated within the literature showing 20 dB net small-signal gain [3]. Utilizing a coordinate transformation as in [4] would allow for the waveguide sidewall gratings demonstrated in Chapter 4 to be adapted for the curved propagation of such a spiral waveguide, and thus allow such a long cavity structure to be fabricated into a distributed feedback or distributed Bragg reflector laser. Care would need to be taken here in designing the structure to alleviate potential catastrophic bend loss, as the standard linear cavity designs featured in Chapter 6 have extremely high minimum bend radii (greater than 5 mm).

7.3 O-Band Linear and Ring Lasers

As was presented in Chapter 5, the neodymium (Nd^{3+}) dopant ion can be utilized to impart optical gain within the telecommunications O-band (13xx nm) when pumped with a source in the 808 nm wavelength range. With the center wavelength of the waveguide sidewall Bragg gratings discussed in Chapter 4 controlled by the repeating period of the structure, a simple reduction of this period should shift the wavelength of operation of the distributed feedback and distributed Bragg reflector lasers discussed in Chapter 6 from the C-band to the O-band. This shift, coupled with a substitution of the Er dopant for an Nd dopant, in theory should allow for an O-band optical source that leverages the same techniques developed for the C-band devices. With these considerations in mind, this exact experiment was carried out, with representative results from a series of distributed feedback lasers with cavity lengths of 21.5 mm and repeating Bragg periods of 420 nm shown in Figure 7.6.

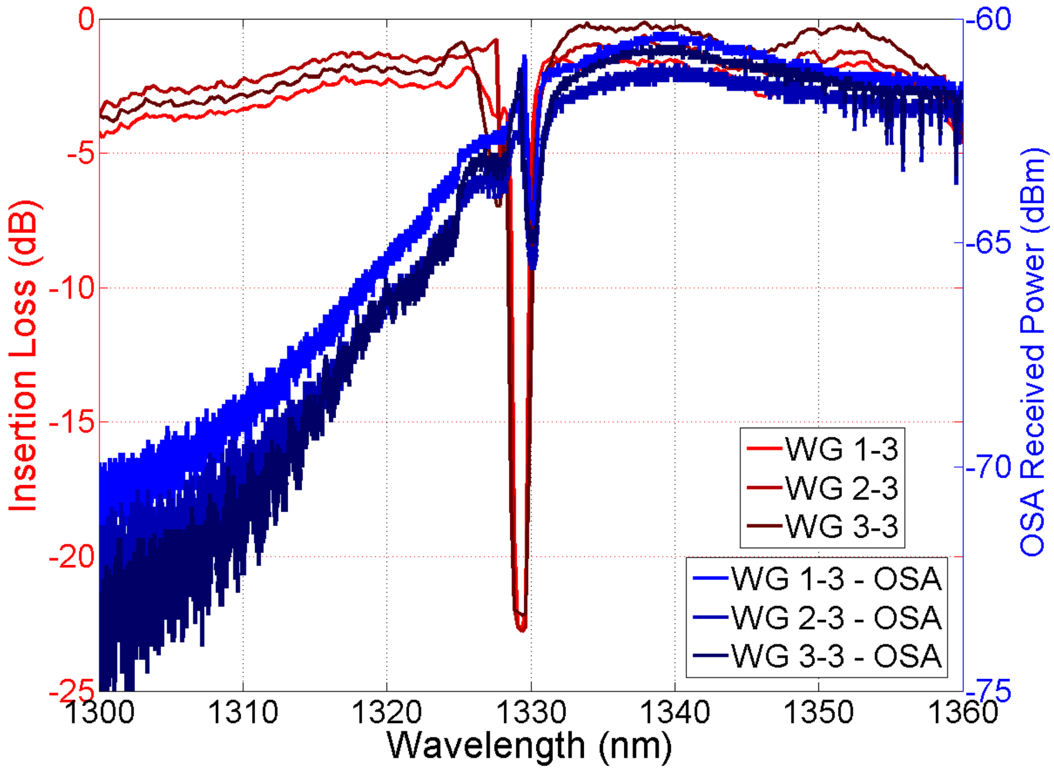

Figure 7.6: *Cold-cavity transmission response (red) and off-chip spontaneous emission spectra (blue) for a variety of tested distributed feedback laser cavities. The insertion loss (IL) for the devices includes the fiber-to-chip coupling losses, which for this case was near 1-2 dB/facet. The devices featured a neodymium dopant concentration at 2.0 x* 10^{20} *cm*$^{-3}$*, a nominal waveguide width of 2.8 μm, a cavity length of 21.5 mm, a κL product of 34.4 cm*$^{-1}$*, and a λ/4 section within the center of the cavity length. The designs in this case (label WG 1-3, WG 2-3, and WG3-3) were identical repeats created to track lithography uniformity.*

As can be seen, when optically pumped the devices do indeed emit spontaneous emission over a bandwidth greater than 40 nm, with a 'notch' present in the output spectra corresponding to the Bragg reflector. Due to the limited pump power though, the devices were never able to reach threshold and achieve stimulated (lasing) emission, even when excited from both ends simultaneously by a pair of 250 mW 808 nm pump diodes.

Following the results of this experiment, a series of deeply etched strongly guiding racetrack ring resonator cavities, as detailed in Chapter 4, was fabricated and tested. The racetrack coupler allowed for the coupling of the signal and pump light into the ring to be controlled independently, ensuring that the 13xx nm signal light experienced a 'high reflectivity mirror' ideal for low lasing thresholds and the 808 nm pump light was able to be maximally coupled into the ring cavity. Representative results are shown in Figure 7.7 for a racetrack ring design with a 125 μm bend radius.

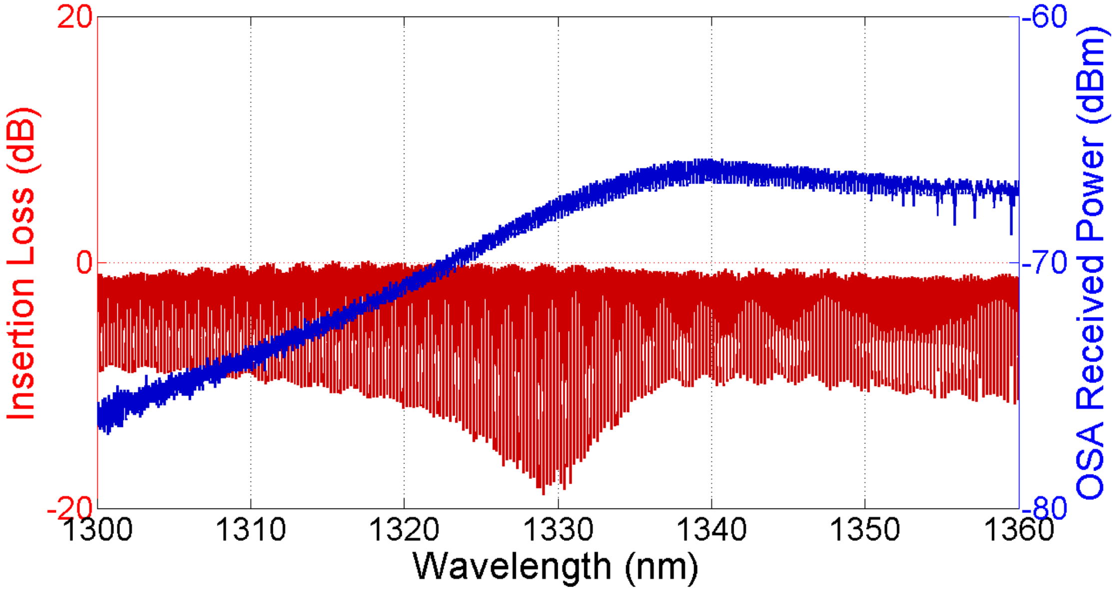

Figure 7.7: *Cold-cavity transmission response (red) and off-chip spontaneous emission spectra (blue) for a 4.78 mm long bus-coupled ring resonator cavity. The insertion loss (IL) for the devices does not include the fiber-to-chip coupling losses. This particular design iteration featured deeply etched bent waveguides with a 125 μm bend radius and deep to*

shallow taper transition sections that were 100 μm long, similar to the design show in Figure 4.28.

As was the same case for the linear cavity design, when optically pumped the device does indeed emit spontaneous emission over a bandwidth greater than 40 nm, with multiple ‘notches’ present in the output spectra corresponding to the ring resonator’s transmission response. Again, the devices were never able to reach threshold and achieve stimulated (lasing) emission, even when excited from both ends simultaneously by a pair of 250 mW 808 nm pump diodes. Further exploration in this area should start by considering an alternative dopant source to neodymium, such as praseodymium, which is common in datacom fiber amplifiers operation in the O-band [5].

7.4 High-Level Platform Integration

More advanced functional applications, such as a fully integrated interferometric optical gyroscope system, require both an active media section (or light generating/amplifying section) to a fully passive media section (no generation of photons) that are optically linked on chip. This can be accomplished through the use of a tapered mode converter in the same way the bend-to-straight transition sections detailed in Chapter 4 operate. Figure 7.8 shows a schematic view of what such a transition would look like in the context of the work presented in this thesis.

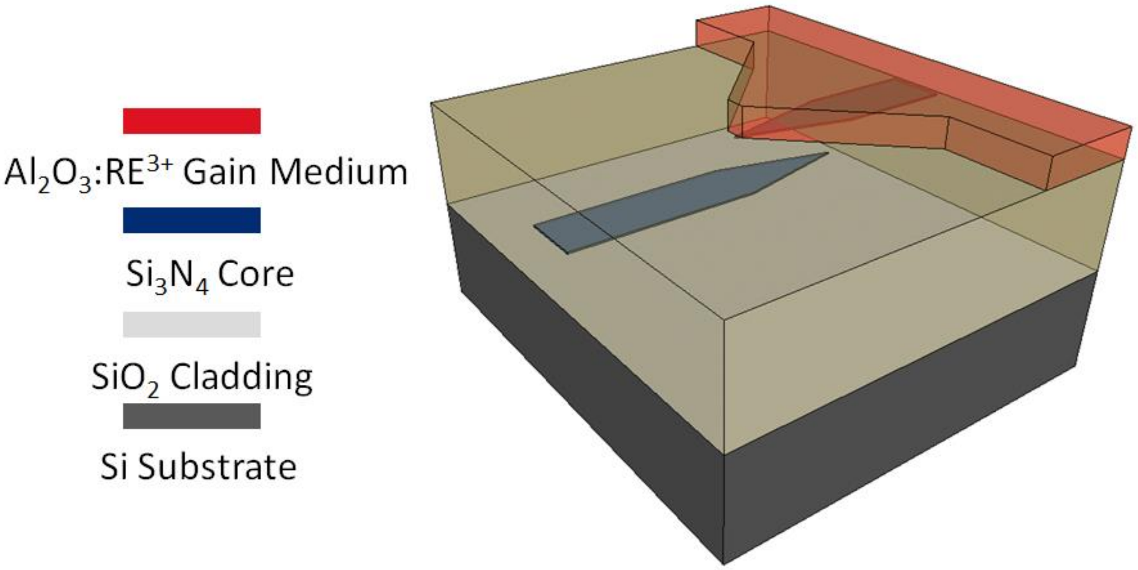

Figure 7.8: *Three-dimensional diagram of an adiabatic waveguide active/passive transition section. Both the Si_3N_4 waveguide and the Al_2O_3 host material are etched in this case to give the highest coupling efficiency and lowest possible reflection.*

The main issue with fabricating such a transition section is the etching of the Al_2O_3 host material that contains the rare-earth-ion dopant atoms, as it is highly chemically stable and resistant to most $CHF_3/CF_4/O_2$-based etches [6]. So not only will etching entirely the host medium require additional fabrication development to ensure low optical loss over the passive waveguide sections, but the 'tip' of the taper sections, which must be sharp to achieve maximal coupling, will require careful lithography optimization. This is quantified in Figure 7.9 through a series of FIMMPROP FDTD calculations on a structure such as that shown in Figure 7.8.

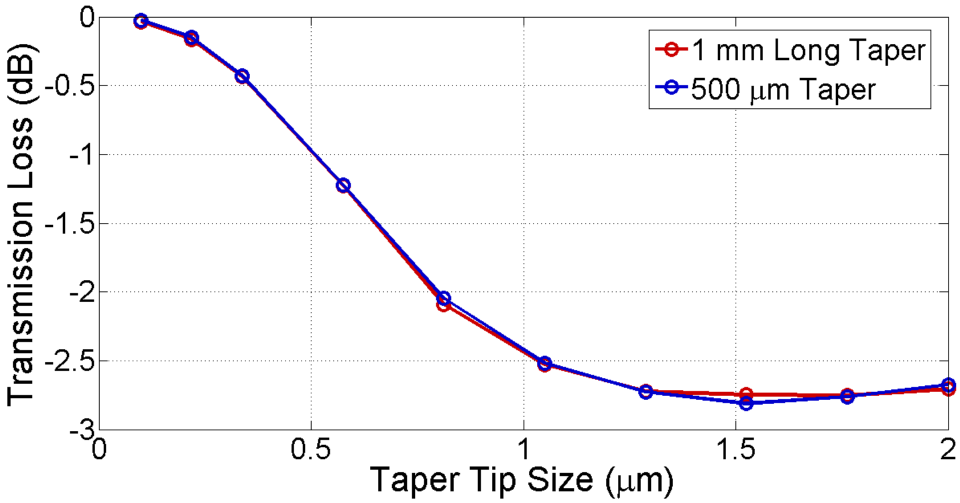

Figure 7.9: *FDTD simulation (FIMMPROP) results for the structure shown in Figure 7.8. The transmitted power lost (uncoupled) by the adiabatic transition section relative to the input power is given vs. size of the taper tip for two different total lengths of taper section.*

The size of the taper tip can influence the transmission efficiency by up to 3 dB depending upon its resolution. Figure 7.10 shows an SEM image of a fabrication development effort for such a structure.

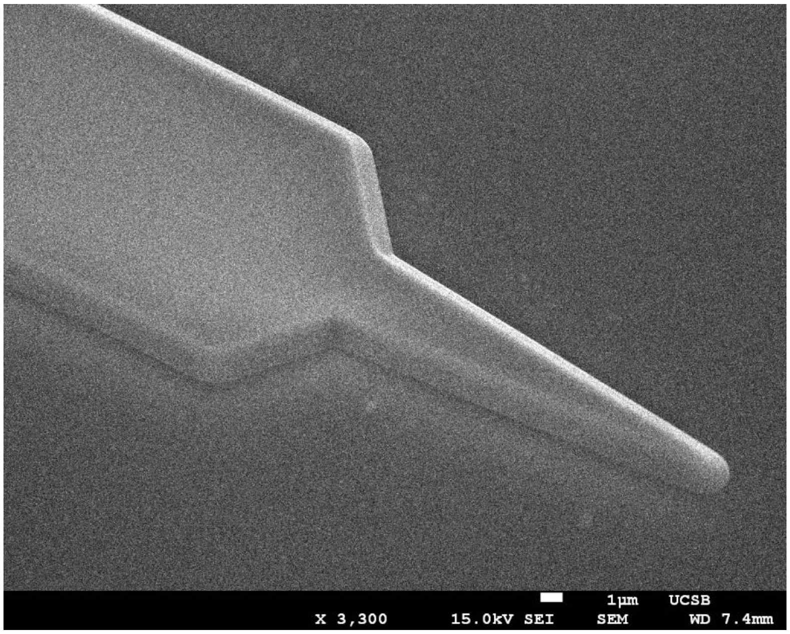

Figure 7.10: *SEM micrograph of an etched 1.5 µm thick* Al_2O_3 *taper tip section displaying significant sidewall angle with respect to vertical.*

Due to the poor sidewall angle of the etch, the tip section has been significantly rounded. Such a geometry would be expected to induce a high degree of loss when coupling. Additional fabrication development in this area is needed before further advanced integrated designs can be realized.

7.5 References

[1] E. H. Bernhardi, H. A.G.M. van Wolferen, L. Agazzi, M. R.H. Khan, C. G.H. Roeloffzen, K. Wörhoff, M. Pollnau, and R. M. de Ridder, "Ultra-narrow-linewidth, single-frequency distributed feedback waveguide laser in Al_2O_3:Er^{3+}on silicon," Opt. Lett. 35, 2394-2396 (2010).

[2] G. Singh, Purnawirman, J. D. B. Bradley, N. Li, E. S. Magden, M. Moresco, T. N. Adam, G. Leake, D. Coolbaugh, and M. R. Watts, “Resonant pumped erbium-doped waveguide lasers using distributed Bragg reflector cavities,” Opt. Lett. 41, 1189-1192 (2016).

[3] S. A. Vázquez-Córdova, M. Dijkstra, E. H. Bernhardi, F. Ay, K. Wörhoff, J. L. Herek, S. M. García-Blanco, and M. Pollnau, "Erbium-doped spiral amplifiers with 20 dB of net gain on silicon," Opt. Express 22, 25993-26004 (2014).

[4] C. Lin, E. W. Jacobs, J. S. Rodgers, “Spiral planar-waveguide Bragg gratings,” Proc. SPIE 7218, Integrated Optics: Devices, Materials, and Technologies XIII, 72180E (2009).

[5] Y. Nishida *et al.*, "Development of an efficient praseodymium-doped fiber amplifier," in *IEEE Journal of Quantum Electronics* 34 (8), 1332-1339 (1998).

[6] J. D. Bradley, F. Ay, K. Wörhoff, and M. Pollnau, “Fabrication of low-loss channel waveguides in Al_2O_3 and Y_2O_3 layers by inductively coupled plasma reactive ion etching,” Appl. Phys. B 89(2), 311-318 (2007).

Appendix 1: Complete Process Traveler

A.1 Si_3N_4 Waveguide Lithography and Etch

Step	Details (Current Process)	Time
Inspect/clean	Iso swab, DI rinse if things looking bad	
Si3N4 Waveguide Litho	Dehydration bake at 135 C	5 min
	Dispense AR2-600 (Recipe 6)	
	Bake AR2 at 220 C, rest on metal for 1 min afterwards	3 min
	Dispense UV6 0.8 (Recipe 8)	
	Bake UV6 at 135 C, rest on metal for 1 min afterwards	1 min
	Expose in ASML (14.5 mJ 0F)	
	Post-exposure bake at 135 C, rest on metal	90 s
	Develop in AZ 300 MIF, no agitation	15 s
	Inspect - Optical microscope	
AR2-600 Etch - RIE #5	Chamber O2 prep - 45 sccm, 50 mT, 300 W	5 min
	AR2-600 O2 etch - 20 sccm, 10 mT, 100 W	30 s
	Inspect - Optical microscope	
Si3N4 Etch - ICP #2	#100 - O2 Clean + CHF3 Coat : Chamber Only	5 min + 1 min
	#104 - NanoEtch - CHF3/CF4/O2 : Insert Wafer	xx min
	#103 - O2 Clean : Chamber Only	5 min
Post-Etch Clean	ICP #1 O2 ash, Recipe 306: O2 Ash	20 min
	Strip PR in NMP at 80 C in ultrasonic	10 min / 10 min
	Isopropanol 2x dunk and ultrasonic, DI spray rinse	1 min / 1 min
	H2SO4 + H2O2 (piranha clean), DI rinse	15 min / 15 min
	Inspect - Optical microscope	10 min
	Inspect - AFM	
	Inspect - SEM	
	Measure - Dektak	
Cladding Deposition - PECVD #2	Chamber Coat : Mike Std. Oxide (25 nm/min) : Chamber Only	10 min

	Deposition : Mike Std. Oxide (25 nm/min) : Insert Wafer	xx min
	Wet Clean	
	Std. Plasma Clean	xx min
	Measure - Ellipsometer	

A.2 Ti Hard Mask Deposition

Step	Details (Current Process)	Time
Ti Mask Deposition - Sputter #3	Ti RF Pre-Clean	5 min
	Deposition : Michael Ti_RF Dep (require 1.2 um)	xx min
	Tape on test sample to Dektak	
	Measure - Dektak	

A.3 Deep SiO_2 Etch and Anneal

Step	Details (Current Process)	Time
Deep Etch Litho	Dehydration bake at 135 C	5 min
	Dispense AR2-600 (Recipe 6)	
	Bake AR2 at 220 C, rest on metal for 1 min afterwards	3 min
	Dispense UV6 0.8 (Recipe 8)	
	Bake UV6 at 135 C, rest on metal for 1 min afterwards	1 min
	Expose in ASML (14.5 mJ 0F)	
	Post-exposure bake at 135 C, rest on metal	90 s
	Develop in AZ 300 MIF, no agitation	15 s
	Inspect - Optical microscope	
AR2-600 Etch - RIE #5	Chamber O2 prep - 45 sccm, 50 mT, 300 W	5 min
	AR2-600 O2 etch - 20 sccm, 10 mT, 100 W	30 s
	Inspect - Optical microscope	
Ti Etch - ICP #1	#121 - O2 Clean - Chamber Only	5 min
	#130 - TIDE Etch - Cl2/Ar : Insert Wafer	xx min

	Watch etch monitor -> should be ~1150 nm/1.25 min	
	RF stop when etched through	
	#306 - O2 Ash	20 min
	#121 - CF4/O2 Clean - Chamber Only	10 min
Inspect Ti Mask	Strip PR in NMP at 80 C in ultrasonic	10 min / 10 min
	Isopropanol 2x dunk and ultrasonic, DI spray rinse	1 min / 1 min
	Inspect - Optical microscope	
	Inspect - SEM	
	Measure - Dektak	
Deep SiO2 Etch - ICP #1	#121 - O2 Clean - Chamber Only	5 min
	#107 - Deep SiO2 Etch - CHF3/CF4/O2/He : Insert Wafer	xx min
	Watch etch monitor -> should be ~6 um/18.1 min	
	RF stop when etched through	
	#121 - O2 Clean - Chamber Only	30 min
Post-Etch Clean	ICP #1 O2 ash, Recipe 306: O2 Ash	20 min
	H2SO4 + H2O2 (piranha clean), DI rinse	1 min / 5 min / 15 min
	Isopropanol 2x dunk and ultrasonic, DI spray rinse	1 min / 1 min
	H2SO4 + H2O2 (piranha clean), DI rinse	15 min / 15 min
	Inspect - Optical microscope	
	Inspect - SEM	
	Measure - Dektak	
	Isopropanol 2x dunk and ultrasonic, DI spray rinse	1 min / 1 min
	H2SO4 + H2O2 (piranha clean), DI rinse	5 min
Anneal - Tystar #1	1050 C; 3.0 SLPM N2	7 hour
	Inspect - Ellipsometer	

A.4 Dicing and $Al_2O_3:RE^{3+}$ Deposition

Step	Details (Current Process)	Time
Dicing Resist Protect	Double layer spinner sheet	
	Dispense HMDS, let rest on wafer	1 min

	Spin (Recipe 5)	
	Remove and dispose outer spinner sheet	
	Dispense SPR 220-3 (Recipe 4)	
	Bake 220-7 at 115 C, rest on metal	5 min
Dice	G1440 hubbed blade, 0.09 mm cut height (from bottom)	
Post-Dice Clean	Strip PR in NMP at 80 C in ultrasonic	10 min / 10 min
	Isopropanol 2x dunk and ultrasonic, DI spray rinse	1 min / 1 min
	H2SO4 + H2O2 (piranha clean), DI rinse	15 min / 15 min
	Inspect - Optical microscope	10 min
Al2O3:Nd3+ Deposition - Sputter #3	H2SO4 + H2O2 (piranha clean), DI rinse	5 min
	Deposition : Michael RF_Al2O3 (desire 1.5 um)	xx min
	Measure - Ellipsometer	
Dicing Resist Protect	Double layer spinner sheet	
	Dispense HMDS, let rest on wafer	1 min
	Spin (Recipe 5)	
	Remove and dispose outer spinner sheet	
	Dispense SPR 220-3 (Recipe 4)	
	Bake 220-7 at 115 C, rest on metal	5 min
Dice	G1440 hubbed blade, 0.09 mm cut height (from bottom)	

Appendix 2: Sidewall Bragg Grating, Distributed Feedback, and Distributed Bragg Reflector T-Matrix MATLAB Code

```
%Michael Belt
%7-15-15
%Grating T-Matrix Code
%Calculate transmission and reflection spectra of an apodized grating using T-matrix formalism
%All units in m unless otherwise noted

tic

clear all
close all
```

```
clc

%Coupling constants
% Kloop = [0.66 0.5 0.31 0.24]; %coupling constant in cm-1 for mirror 1
% Kloop = [2 1.8 1.6 1.4 1.2]; %coupling constant in cm-1 for mirror 1
Kloop = [4.0 3.8 3.6 3.4 3.2 3.0 2.8 2.6 2.4 2.2]; %coupling constant in
cm-1 for mirror 1

for kappaloop = 1:length(Kloop)

%Simulation Design Parameters
%Center wavelength and physical period
Bragglambda = 1575*(1e-9); %Bragg wavelength
SimWaveWindow = 5*(1e-9); %Simulation wavelength range
L1 = 268*(1e-9); %half period length (notch section)
L2 = 268*(1e-9); %half period length (wider section)
biglambda = L1 + L2; %full period length

%Effective indices and loss
neff = Bragglambda./(2.*biglambda); %effective index of the grating
nlaser = 3.27; %effective index of hybrid active section
alphadBm = 10; %assumed grating loss in dB/m
alpha = alphadBm/(10*log10(exp(1))); %assumed grating loss in 1/m
alphalaserdBm = 0; %assumed hybrid loss in dB/m
alphalaser = alphalaserdBm/(10*log10(exp(1))); %assumed hybrid loss in 1/m

%Overall lengths
totallength1 = 18e-3; %total grating length for mirror 1 = Lgf
totallength2 = 1e-3; %total grating length for mirror 2 = Lgb
laserlength = 2.4e-3; %total cavity length of hybrid active section
% cavitylength = 1e-3; %total cavity length between mirrors 1 and 2 = Lc
% samplelength1 = 1e-3; %length of sampled section for mirror 1 = L1
% samplelength2 = 1e-3; %length of sampled section for mirror 1 = L1
% phaseshiftlength = L1.*1.0; %phase shift length
% inputlength = 0.25e-3; %length of input waveguide;
% outputlength = 0.25e-3; %length of output waveguide;
m1 = floor(totallength1/biglambda); %number of periods in mirror 1
% m2 = floor(totallength2/biglambda); %number of periods in mirror 2

% kappacm1 = 0.5; %coupling constant in cm-1 for mirror 1
kappacm1 = Kloop(kappaloop); %coupling constant in cm-1 for mirror 1
kappa1 = kappacm1.*100; %coupling constant in m-1 for mirror 1
% kappacm2 = kappacm1; %coupling constant in cm-1 for mirror 2
% kappa2 = kappacm2.*100; %coupling constant in m-1 for mirror 2

%Simulation Functional Parameters
%Coldren Chapter 3, page 116
%Loop where calculations are performed wavelength by wavelength
numpoints = 1000; %number of data points
lambda = linspace(Bragglambda - (SimWaveWindow./2),Bragglambda +
(SimWaveWindow./2),numpoints); %wavelength

%Window functions
zdist1 = linspace(biglambda,totallength1,m1);
% zdist2 = linspace(biglambda,totallength1,m2);
```

```
%Apodization functions from 1998_Ennser_Optimization of Apodized Linearly
Chirped Fiber Gratings...
%Blackman window function
BlackX = 2.*pi.*(zdist1 - (totallength1./2))./totallength1;
BlackmanWindow = kappacm1.*((1+1.19.*cos(BlackX) +
0.19.*cos(2.*BlackX))./2.38);

%Positive tanh window function
for z = 1:length(zdist1)

    if zdist1(z) <= totallength1/2
        PosTanhWindow(z) = kappacm1.*tanh(2.*4.*zdist1(z)./totallength1);

    else
        PosTanhWindow(z) = kappacm1.*tanh(2.*4.*(totallength1 -
zdist1(z))./totallength1);

    end

end

%Linear function
LinearWindow = kappacm1.*ones(1,length(zdist1)); %Apodization Function

%Choose window function here
WinFunc1 = BlackmanWindow;
% WinName = 'Linear';
WinName = 'Blackman';

%Make beginning K going into loop be equal to the K at the mirror entrance
kappa1 = WinFunc1(1).*100; %apodized coupling constant in m-1 for mirror 1

for k = 1:length(lambda)
    disp(['Wavelength iteration ', num2str(k), ' of ',
num2str(length(lambda))])
    for n = 1:length(kappacm1)

        effectivelength1(n) =
(1./(2.*kappa1(n))).*tanh(kappa1(n).*totallength1); %effective grating
length for mirror 1
%         effectivelength2(n) =
(1./(2.*kappa2(n))).*tanh(kappa2(n).*totallength2); %effective grating
length for mirror 2

        deltan1(n) = (kappa1(n).*Bragglambda)./2; %index difference for
mirror 1 Coldren Chapter 3 page 121
%         deltan2(n) = (kappa2(n).*Bragglambda)./2; %index difference for
mirror 2 Coldren Chapter 3 page 121

        %Propagation Constants and Such
        %Propagation Constant at the Bragg Wavelength
        beta(k) = (2*pi.*neff)./(lambda(k)); %propagation constant at all
wavelengths (assume fitted disperion)
```

```
        beta0 = (2*pi.*neff)./(Bragglambda); %propagation constant at
Bragg wavelength
        delta(k) = beta(k) - beta0; %detuning parameter

        %Index Values for Mirror 1
        n1k1(n,k) = neff - deltan1(n)/2; %assumed index of notch section
using index difference from fitted Kappa value including dispersion
        beta1k1(n,k) = ((2*pi.*n1k1(n,k))./(lambda(k))) - 1j.*alpha./2;
%assumed propagation constant of notch section with loss
        n2k1(n,k) = neff + deltan1(n)/2; %assumed index of wider section
using index difference from fitted Kappa value including dispersion
        beta2k1(n,k) = ((2*pi.*n2k1(n,k))./(lambda(k))) - 1j.*alpha./2;
%assumed propagation constant of wider section with loss

        rk1(n,k) = -(n1k1(n,k) - n2k1(n,k))./(n1k1(n,k) + n2k1(n,k));
%field reflection coefficient
        tk1(n,k) = sqrt(1-(rk1(n,k).^2)); %field transmission coefficient

        %Index Values for Cavity Reflection
        n1kcr = 1; %assumed index of air
        beta1kcr(k) = (2*pi.*n1kcr)./(lambda(k)); %assumed propagation
constant of air
        n2kcr(n,k) = nlaser; %assumed index of hybrid active section
        beta2kcr(n,k) = ((2*pi.*n2kcr(n,k))./(lambda(k))) - 1j.*alpha./2;
%assumed propagation constant of hybrid active section with loss

        rkcr(n,k) = -(n1kcr - n2kcr(n,k))./(n1kcr + n2kcr(n,k)); %field
reflection coefficient
        tkcr(n,k) = sqrt(1-(rkcr(n,k).^2)); %field transmission
coefficient
        mcr = 1;

%         %Index Values for Mirror 2
%         n1k2(n,k) = neff - deltan2(n)/2; %assumed index of notch section
using index difference from fitted Kappa value including dispersion
%         beta1k2(n,k) = ((2*pi.*n1k2(n,k))./(lambda(k))) - 1j.*alpha./2;
%assumed propagation constant of notch section with loss
%         n2k2(n,k) = neff + deltan2(n)/2; %assumed index of wider section
using index difference from fitted Kappa value including dispersion
%         beta2k2(n,k) = ((2*pi.*n2k2(n,k))./(lambda(k))) - 1j.*alpha./2;
%assumed propagation constant of wider section with loss
%
%         rk2(n,k) = -(n1k2(n,k) - n2k2(n,k))./(n1k2(n,k) + n2k2(n,k));
%field reflection coefficient
%         tk2(n,k) = sqrt(1-(rk2(n,k).^2)); %field transmission
coefficient
%
%         %Index Values for Input Facet
%         n1kif = 1; %assumed index of air
%         beta1kif(k) = (2*pi.*n1kif)./(lambda(k)); %assumed propagation
constant of air
%         n2kif(n,k) = neff + deltan1(n)/2; %assumed index of wider
section using index difference from fitted Kappa value including
dispersion
%         beta2kif(n,k) = ((2*pi.*n2kif(n,k))./(lambda(k))) -
1j.*alpha./2; %assumed propagation constant of wider section with loss
```

```
%
%         rkif(n,k) = -(n1kif - n2kif(n,k))./(n1kif + n2kif(n,k)); %field
reflection coefficient
%         tkif(n,k) = sqrt(1-(rkif(n,k).^2)); %field transmission
coefficient
%         mif = 1;
%
%         %Index Values for Output Facet
%         n1kof(n,k) = neff + deltan1(n)/2; %assumed index of wider
section using index difference from fitted Kappa value including
dispersion
%         beta1kof(n,k) = ((2*pi.*n1kof(n,k))./(lambda(k))) -
1j.*alpha./2; %assumed propagation constant of notch section with loss
%         n2kof = 1; %assumed index of air
%         beta2kof(k) = (2*pi.*n2kof)./(lambda(k)); %assumed propagation
constant of air
%
%         rkof(n,k) = -(n1kof(n,k) - n2kof)./(n1kof(n,k) + n2kof); %field
reflection coefficient
%         tkof(n,k) = sqrt(1-(rkof(n,k).^2)); %field transmission
coefficient
%         mof = 1;

%         %---% Begin recursive chirp setup + loop

        %Phase terms phiplus and phiminus for Grating 1 are:
        phiplusk1(n,k) = beta1k1(n,k).*L1 + beta2k1(n,k).*L2; %positive
phase term
        phiminusk1(n,k) = beta1k1(n,k).*L1 - beta2k1(n,k).*L2; %negative
phase term

        %T Matrix Segments for Grating 1
        T11k1(n,k) = (1./(tk1(n,k).^2)).*( exp(1j.*phiplusk1(n,k)) -
(rk1(n,k).^2).*exp(-1j.*phiminusk1(n,k)) );
        T21k1(n,k) = (rk1(n,k)./(tk1(n,k).^2)).*( exp(1j.*phiplusk1(n,k))
- exp(-1j.*phiminusk1(n,k)) );
        T12k1(n,k) = (rk1(n,k)./(tk1(n,k).^2)).*( exp(-1j.*phiplusk1(n,k))
- exp(1j.*phiminusk1(n,k)) );
        T22k1(n,k) = (1./(tk1(n,k).^2)).*( exp(-1j.*phiplusk1(n,k)) -
(rk1(n,k).^2).*exp(1j.*phiminusk1(n,k)) );

        %Entire Grating 1 T Matrix
        Tgk1 = [T11k1(n,k) T12k1(n,k); T21k1(n,k) T22k1(n,k)]^1;

        %Grating 1 T Matrix Individual Portions
        Tg11k1(n,k) = Tgk1(1,1);
        Tg21k1(n,k) = Tgk1(2,1);
        Tg12k1(n,k) = Tgk1(1,2);
        Tg22k1(n,k) = Tgk1(2,2);

        %Killer recursive loop to calculate apodized Grating 1
        for l = 2:length(zdist1)

            %Apozidation functionality begin
```

```
            kappa1 = WinFunc1(l).*100; %appodized coupling constant in m-1
for mirror 1

            deltan1(n) = (kappa1.*Bragglambda)./2; %index difference for
mirror 1 Coldren Chapter 3 page 121

            %Index Values for Mirror 1
            n1k1(n,k) = neff - deltan1(n)/2; %assumed index of notch
section using index difference from fitted Kappa value including
dispersion
            beta1k1(n,k) = ((2*pi.*n1k1(n,k))./(lambda(k))) -
1j.*alpha./2; %assumed propagation constant of notch section with loss
            n2k1(n,k) = neff + deltan1(n)/2; %assumed index of wider
section using index difference from fitted Kappa value including
dispersion
            beta2k1(n,k) = ((2*pi.*n2k1(n,k))./(lambda(k))) -
1j.*alpha./2; %assumed propagation constant of wider section with loss

            rk1(n,k) = -(n1k1(n,k) - n2k1(n,k))./(n1k1(n,k) + n2k1(n,k));
%field reflection coefficient
            tk1(n,k) = sqrt(1-(rk1(n,k).^2)); %field transmission
coefficient

            %Phase terms phiplus and phiminus for Grating 1 are:
            phiplusk1(n,k) = beta1k1(n,k).*L1 + beta2k1(n,k).*L2;
%positive phase term
            phiminusk1(n,k) = beta1k1(n,k).*L1 - beta2k1(n,k).*L2;
%negative phase term

            %T Matrix Segments for Grating 1
            T11k1(n,k) = (1./(tk1(n,k).^2)).*( exp(1j.*phiplusk1(n,k)) -
(rk1(n,k).^2).*exp(-1j.*phiminusk1(n,k)) );
            T21k1(n,k) = (rk1(n,k)./(tk1(n,k).^2)).*(
exp(1j.*phiplusk1(n,k)) - exp(-1j.*phiminusk1(n,k)) );
            T12k1(n,k) = (rk1(n,k)./(tk1(n,k).^2)).*( exp(-
1j.*phiplusk1(n,k)) - exp(1j.*phiminusk1(n,k)) );
            T22k1(n,k) = (1./(tk1(n,k).^2)).*( exp(-1j.*phiplusk1(n,k)) -
(rk1(n,k).^2).*exp(1j.*phiminusk1(n,k)) );

            %Entire Grating 1 T Matrix
            Tgk1 = Tgk1*[T11k1(n,k) T12k1(n,k); T21k1(n,k) T22k1(n,k)];

            %Grating 1 T Matrix Individual Portions
            Tg11k1(n,k) = Tgk1(1,1);
            Tg21k1(n,k) = Tgk1(2,1);
            Tg12k1(n,k) = Tgk1(1,2);
            Tg22k1(n,k) = Tgk1(2,2);

        end

%          %Phase terms phiplus and phiminus for Grating 2 are:
%          phiplusk2(n,k) = beta1k2(n,k).*L1 + beta2k2(n,k).*L2; %positive
phase term
%          phiminusk2(n,k) = beta1k2(n,k).*L1 - beta2k2(n,k).*L2; %negative
phase term
```

```
%
%           %T Matrix Segments for Grating 2
%           T11k2(n,k) = (1./(tk2(n,k).^2)).*( exp(1j.*phiplusk2(n,k)) -
(rk2(n,k).^2).*exp(-1j.*phiminusk2(n,k)) );
%           T21k2(n,k) = (rk2(n,k)./(tk2(n,k).^2)).*(
exp(1j.*phiplusk2(n,k)) - exp(-1j.*phiminusk2(n,k)) );
%           T12k2(n,k) = (rk2(n,k)./(tk2(n,k).^2)).*( exp(-
1j.*phiplusk2(n,k)) - exp(1j.*phiminusk2(n,k)) );
%           T22k2(n,k) = (1./(tk2(n,k).^2)).*( exp(-1j.*phiplusk2(n,k)) -
(rk2(n,k).^2).*exp(1j.*phiminusk2(n,k)) );
%
%           %Entire Grating 2 T Matrix
%           Tgk2 = [T11k2(n,k) T12k2(n,k); T21k2(n,k) T22k2(n,k)]^1;
%
%           %Grating 2 T Matrix Individual Portions
%           Tg11k2(n,k) = Tgk2(1,1);
%           Tg21k2(n,k) = Tgk2(2,1);
%           Tg12k2(n,k) = Tgk2(1,2);
%           Tg22k2(n,k) = Tgk2(2,2);
%
%           %T Matrix Segments for Phase Shift Section (Wider Section)
%           TPhase11(n,k) = exp(1j.*beta2k1(n,k).*(phaseshiftlength));
%           TPhase21(n,k) = 0;
%           TPhase12(n,k) = 0;
%           TPhase22(n,k) = exp(-1j.*beta2k1(n,k).*(phaseshiftlength));
%
%           %Entire Phase Shift Section (Wider Section) T Matrix
%           TPhase = [TPhase11(n,k) TPhase12(n,k); TPhase21(n,k)
TPhase22(n,k)];
%
%           %T Matrix Segments for Input Waveguide Section (Wider Section)
%           TInput11(n,k) = exp(1j.*beta2k1(n,k).*(inputlength));
%           TInput21(n,k) = 0;
%           TInput12(n,k) = 0;
%           TInput22(n,k) = exp(-1j.*beta2k1(n,k).*(inputlength));
%
%           %Entire Phase Shift Section (Wider Section) T Matrix
%           TInput = [TInput11(n,k) TInput12(n,k); TInput21(n,k)
TInput22(n,k)];
%
%           %T Matrix Segments for Output Waveguide Section (Wider Section)
%           TOutput11(n,k) = exp(1j.*beta2k1(n,k).*(outputlength));
%           TOutput21(n,k) = 0;
%           TOutput12(n,k) = 0;
%           TOutput22(n,k) = exp(-1j.*beta2k1(n,k).*(outputlength));
%
%           %Entire Phase Shift Section (Wider Section) T Matrix
%           TOutput = [TOutput11(n,k) TOutput12(n,k); TOutput21(n,k)
TOutput22(n,k)];
%
%           %T Matrix Segments for Input Facet (CHECK THIS IT'S PROBABLY
WRONG)
%
%           T11kif(n,k) = (1./(tkif(n,k).^2));
%           T21kif(n,k) = (rkif(n,k)./(tkif(n,k).^2));
%           T12kif(n,k) = (rkif(n,k)./(tkif(n,k).^2));
%           T22kif(n,k) = (1./(tkif(n,k).^2));
```

```
%
%          %Entire Input Facet T Matrix
%          Tgkif = [T11kif(n,k) T12kif(n,k); T21kif(n,k) T22kif(n,k)];
%
%          %Input Facet T Matrix Individual Portions
%          Tg11kif(n,k) = Tgkif(1,1);
%          Tg21kif(n,k) = Tgkif(2,1);
%          Tg12kif(n,k) = Tgkif(1,2);
%          Tg22kif(n,k) = Tgkif(2,2);
%
%          %T Matrix Segments for Output Facet (CHECK THIS IT'S PROBABLY
WRONG)
%          T11kof(n,k) = (1./(tkof(n,k).^2));
%          T21kof(n,k) = (rkof(n,k)./(tkof(n,k).^2));
%          T12kof(n,k) = (rkof(n,k)./(tkof(n,k).^2));
%          T22kof(n,k) = (1./(tkof(n,k).^2));
%
%          %Entire Output Facet T Matrix
%          Tgkof = [T11kof(n,k) T12kof(n,k); T21kof(n,k) T22kof(n,k)];
%
%          %Output Facet T Matrix Individual Portions
%          Tg11kif(n,k) = Tgkif(1,1);
%          Tg21kif(n,k) = Tgkif(2,1);
%          Tg12kif(n,k) = Tgkif(1,2);
%          Tg22kif(n,k) = Tgkif(2,2);

%          %T Matrix Segments for Cavity Reflection (CHECK THIS IT'S
PROBABLY WRONG)
%          T11kcr(n,k) = (1./(tkcr(n,k).^2));
%          T21kcr(n,k) = (rkcr(n,k)./(tkcr(n,k).^2));
%          T12kcr(n,k) = (rkcr(n,k)./(tkcr(n,k).^2));
%          T22kcr(n,k) = (1./(tkcr(n,k).^2));

        %T Matrix Segments for Cavity Reflection (THIS SHOULD BE CORRECT)
        T11kcr(n,k) = (1./(tkcr(n,k)));
        T21kcr(n,k) = (rkcr(n,k)./(tkcr(n,k)));
        T12kcr(n,k) = (rkcr(n,k)./(tkcr(n,k)));
        T22kcr(n,k) = (1./(tkcr(n,k)));

        %Entire Cavity Reflection T Matrix
        Tgkcr = [T11kcr(n,k) T12kcr(n,k); T21kcr(n,k) T22kcr(n,k)];

        %T Matrix Segments for Cavity Section (Hybrid Section)
        TPhase11(n,k) = exp(1j.*beta2kcr(n,k).*(laserlength));
        TPhase21(n,k) = 0;
        TPhase12(n,k) = 0;
        TPhase22(n,k) = exp(-1j.*beta2kcr(n,k).*(laserlength));

        %Entire Phase Shift Section (Wider Section) T Matrix
        TPhase = [TPhase11(n,k) TPhase12(n,k); TPhase21(n,k)
TPhase22(n,k)];

        %Entire DFB T Matrix (Grating-Phase Shift-Grating)
%          TDFB = Tgkif*TPhase*Tgk1*TPhase*Tgkof;
%          TDFB = Tgk1*TPhase*Tgk2;
```

```
%         TDFB = Tgkif*TInput*Tgk1*TPhase*Tgk2*TOutput*Tgkof;
%         TDFB = Tgk1*Tgk2;
        TDFB = Tgk1*TPhase*Tgkcr;
%         TDFB = Tgk1;

        %DFB T Matrix Individual Portions
        TDFB11(n,k) = TDFB(1,1);
        TDFB21(n,k) = TDFB(2,1);
        TDFB12(n,k) = TDFB(1,2);
        TDFB22(n,k) = TDFB(2,2);

        %Grating 1 S Matrix Individual Portions
        Sg11k1(n,k) = (1./(Tg11k1(n,k))).*Tg21k1(n,k);
        Sg21k1(n,k) = (1./(Tg11k1(n,k))).*1;
        Sg12k1(n,k) = (1./(Tg11k1(n,k))).*det(Tgk1);
        Sg22k1(n,k) = (1./(Tg11k1(n,k))).*(-1.*Tg12k1(n,k));

        %Cavity Reflection S Matrix Individual Portions
        Scr11k1(n,k) = (1./(T11kcr(n,k))).*T21kcr(n,k);
        Scr21k1(n,k) = (1./(T11kcr(n,k))).*1;
        Scr12k1(n,k) = (1./(T11kcr(n,k))).*det(Tgkcr);
        Scr22k1(n,k) = (1./(T11kcr(n,k))).*(-1.*T12kcr(n,k));

        %Cavity Phase Section S Matrix Individual Portions
        Shd11k1(n,k) = (1./(TPhase11(n,k))).*TPhase21(n,k);
        Shd21k1(n,k) = (1./(TPhase11(n,k))).*1;
        Shd12k1(n,k) = (1./(TPhase11(n,k))).*det(TPhase);
        Shd22k1(n,k) = (1./(TPhase11(n,k))).*(-1.*TPhase12(n,k));

%         %Grating 2 S Matrix Individual Portions
%         Sg11k2(n,k) = (1./(Tg11k2(n,k))).*Tg21k2(n,k);
%         Sg21k2(n,k) = (1./(Tg11k2(n,k))).*1;
%         Sg12k2(n,k) = (1./(Tg11k2(n,k))).*det(Tgk2);
%         Sg22k2(n,k) = (1./(Tg11k2(n,k))).*(-1.*Tg12k2(n,k));

        %Entire DFB S Matrix Individual Portions
        SDFB11(n,k) = (1./(TDFB11(n,k))).*TDFB21(n,k);
        SDFB21(n,k) = (1./(TDFB11(n,k))).*1;
        SDFB12(n,k) = (1./(TDFB11(n,k))).*1;
        SDFB22(n,k) = (1./(TDFB11(n,k))).*(-1.*TDFB12(n,k));

        %Grating 1 Reflection and Transmission Spectra
        GratingReflectk1Mag(n,k) = Sg11k1(n,k).*conj(Sg11k1(n,k));
        GratingTransk1Mag(n,k) = Sg21k1(n,k).*conj(Sg21k1(n,k));

%         %Grating 2 Reflection and Transmission Spectra
%         GratingReflectk2Mag(n,k) = Sg11k2(n,k).*conj(Sg11k2(n,k));
%         GratingTransk2Mag(n,k) = Sg21k2(n,k).*conj(Sg21k2(n,k));

        %DFB Reflection and Transmission Spectra
        DFBReflectMag(n,k) = SDFB11(n,k).*conj(SDFB11(n,k));
        DFBTransMag(n,k) = SDFB21(n,k).*conj(SDFB21(n,k));

    end
end
```

```
%Plotting
color = colormap(cool(length(kappacm1)));

set(0,'units','pixels'); %Sets the units of the root object (screen) to
pixels
Pix_SS = get(0,'screensize'); %Obtains this pixel information

for n = length(kappacm1)
    Fig1 = figure(1);
    subplot 211
    plot(lambda*(1e9),10*log10(GratingTransk1Mag(n,:)),'Color',color(n,:))
    xlabel('Wavelength (nm)')
    ylabel('Transmission (dB)')
    title('Grating Transmission')
    hold all

    subplot 212

plot(lambda*(1e9),10*log10(GratingReflectk1Mag(n,:)),'Color',color(n,:))
    xlabel('Wavelength (nm)')
    ylabel('Reflection (dB)')
    title('Grating Reflection')
    set(Fig1,'OuterPosition',[0 50 + Pix_SS(4)/2 Pix_SS(3)/2
Pix_SS(4)/2]);
    hold all

%     Fig2 = figure(2);
%     subplot 211
%
plot(lambda*(1e9),10*log10(GratingTransk2Mag(n,:)),'Color',color(n,:))
%     xlabel('Wavelength (nm)')
%     ylabel('Transmission (dB)')
%     title('Grating 2 Transmission')
%     hold all
%
%     subplot 212
%
plot(lambda*(1e9),10*log10(GratingReflectk2Mag(n,:)),'Color',color(n,:))
%     xlabel('Wavelength (nm)')
%     ylabel('Reflection (dB)')
%     title('Grating 2 Reflection')
%     set(Fig2,'OuterPosition',[Pix_SS(3)/2 50 + Pix_SS(4)/2 Pix_SS(3)/2
Pix_SS(4)/2]);
%     hold all
%
%     Fig3 = figure(3);
%     subplot 211
%     plot(lambda*(1e9),10*log10(DFBReflectMag(n,:)),'Color',color(n,:))
%     xlabel('Wavelength (nm)')
%     ylabel('Reflection (dB)')
%     title('DFB Reflection')
%     hold all
%
%     subplot 212
%     plot(lambda*(1e9),10*log10(DFBTransMag(n,:)),'Color',color(n,:))
```

```
%     xlabel('Wavelength (nm)')
%     ylabel('Transmission (dB)')
%     title('DFB Transmission')
%     set(Fig3,'OuterPosition',[0 50 Pix_SS(3)/2 Pix_SS(4)/2]);
%     hold all

    Fig5 = figure(5);

plot(lambda*(1e9),10*log10(DFBTransMag(n,:)),'Color',color(n,:),'Linewidth
',3)
    set(gca, 'FontSize', 16)
    xlabel('Wavelength (nm)', 'FontSize', 20)
    ylabel('Transmission (dB)', 'FontSize', 20)
    title('Cavity Transmission Spectrum', 'FontSize', 20)
    grid on
    hold all
    set(Fig5,'OuterPosition',[0 50 Pix_SS(3)/2 Pix_SS(4)-50]);
    legend(['\kappa = ', num2str(kappacm1(1)), ' (cm^-^1)'])

    Fig6 = figure(6);

plot(lambda*(1e9),10*log10(DFBReflectMag(n,:)),'Color',color(n,:),'Linewid
th',3)
    set(gca, 'FontSize', 16)
    xlabel('Wavelength (nm)', 'FontSize', 20)
    ylabel('Reflection (dB)', 'FontSize', 20)
    title('Cavity Reflection Spectrum', 'FontSize', 20)
    grid on
    hold all
    set(Fig6,'OuterPosition',[Pix_SS(3)/2 50 Pix_SS(3)/2 Pix_SS(4)-50]);
    legend(['\kappa = ', num2str(kappacm1(1)), ' (cm^-^1)'])

    Fig7 = figure(7);
    plot(zdist1.*1e3,WinFunc1,'Color',[0.7 0 0],'Linewidth',3)
    set(gca, 'FontSize', 16)
    xlabel('Grating Length (mm)', 'FontSize', 20)
    ylabel('Coupling Constant (\kappa cm^-^1)', 'FontSize', 20)
    title('Apodization Profile', 'FontSize', 20)
    grid on
    hold all
    set(Fig7,'OuterPosition',[Pix_SS(3)/4 50 Pix_SS(3)/2 Pix_SS(4)-50]);

end

% filename=input('Filename>>','s');
% filenames=dir([filename '*']);
% ok_write=isempty(filenames);
%
% while ok_write==0
%     ok_write=input('File already exists. 1 to overwrite>>');
% end

filename = [WinName ' Profile - L = ' num2str(totallength1*1e3) ' mm - K =
' num2str(kappacm1) ' cm-1 Laser Cavity Included'];
```

```
save([filename '.mat'])

clearvars -except Kloop
close all
clc

end

toc
```